DISSERTATION

ADVANCING IMPULSIVE RAMAN SPECTROSCOPY AND MICROSCOPY FOR BIOLOGICAL APPLICATIONS

Submitted by

David R. Smith

School of Biomedical Engineering

In partial fulfillment of the requirements

For the Degree of Doctor of Philosophy

Colorado State University

Fort Collins, Colorado

Summer 2024

Doctoral Committee:

Advisor: Randy Bartels
Co-Advisor: Jesse Wilson

Stuart Tobet
Dylan Jost

Copyright by David R Smith 2024

All Rights Reserved

ABSTRACT

ADVANCING IMPULSIVE RAMAN SPECTROSCOPY AND MICROSCOPY FOR BIOLOGICAL APPLICATIONS

Chemically sensitive, label-free spectroscopy and microscopy is a critical tool for the study of many complex and dynamic biological systems. The development of the impulsive stimulated Raman scattering (ISRS) techniques in this thesis represent important steps forward in addressing the ability to interrogate Raman vibrations in complex and scattering samples, particularly low frequency Raman modes.

ACKNOWLEDGEMENTS

Thank you to Randy Bartels for your endless support in the pursuit of this work.

DEDICATION

I would like to dedicate this thesis to Watson.

TABLE OF CONTENTS

LIST OF FIGURES

Chapter 1

Introduction

The discovery and development of light microscopy has been a critical component in advancing many fields of biomedical science. Because light microscopy is noninvasive it can be used to observe live cells with high spatial resolution, enabling research into processes that dictate the behavior of cells, tissues, and organisms. Allows tracking of response to drugs, progression of disease, and a multitude of other forms of perturbations to the biological system.

Objects are visible in standard light microscopy through the combination of light absorption and scattering that occurs when passing light through the sample of interest. Certain parts of cells and tissue will absorb more (or less) light and appear darker (or lighter) under microscopic observation. While standard light microscopy was and is today still a valuable tool, it has a large limitation in that it is impossible to see and track specific cells or intracellular targets such as a specific protein. This ability is crucial for more complex studies investigating the molecular machinery and interactions within cells and organisms. As microscopy and biomedicine advanced through the 20th century, more complex imaging concepts were introduced to investigate the inner workings of biological systems. While standard light microscopy proved groundbreaking for biology and medicine, a large advancement was made by employing molecular tags to allow precise and accurate observation of specific parts or proteins within cells and tissue. The most common molecular tags are fluorescent proteins which can be bound to specific cell sites or proteins.

Fluorescent microscopy is an extremely valuable and widespread technique because of molecular specificity and specific targeting to study the behavior of biomolecules of interest in space and time in live cells and organisms. However, fluorescent microscopy also has certain limitations that motivate further development of alternative ways to achieve target and chemical specificity when studying biological systems with microscopy. Many fluorescent proteins are quite large relative to the molecular targets with which they are being used to target. Biological systems are filled with complex molecular interactions and attaching large exogenous fluorescent proteins to intercelluar

targets can affect the natural biological workings of the system being interrogated. This issue is particularly difficult to manage when studying dynamic systems such as cell metabolism where the normal operation of the cell is desired. In addition to potentially interfering with the regular workings of a cellular system, fluorescent tagging has limitations in which targets are possible to bind to. Other drawbacks of fluorescent tagging include limited diffusion in tissues, probe toxicity, and cross reactivity in binding. Effective fluorescent tags can require significant research and chemistry development for antibody binding and tailoring fluorescent proteins and binding mechanisms. Fluorescent tags can also suffer from bleaching when being used in dynamic studies where repeated measurements over time degrade the brightness of the fluorescent tag, making long term tracking difficult. These limitations motivated additional research into methods of achieving high resolution microscopy of specific targets by leveraging label-free techniques that leave the biological system unperturbed and don't rely on specific binding mechanisms. The label-free methods of tracking targets in cells often utilize nonlinear physical interactions between incident light and the cellular targets in question.

Although microscopy with exogenous fluorophorescent tags is an extremely powerful technique, there is significant need for complementary techniques that can provide chemically-specific, time-resolved information about cells or biological systems with more target flexibility and less disruption to the natural order of the biological system. A well known option for label-free imaging is utilizing vibrational spectroscopy where a photon-matter interaction between an incoming photon and the sample of interest reveals information about the molecular structure present in the photon-matter interaction. Vibrational spectroscopy permits label-free, chemically-specific noninvasive interrogation of biological samples and tissue.

Raman vibrational spectroscopy has been established as a valuable tool for biology, medicine, and materials science. Raman spectroscopy allows for chemically specific, label-free, hyperspectral imaging of samples. Conventional Raman microscopy based on spontaneous Raman scattering has been widely used for cellular, tissue, *in vivo*, and plant imaging [2, 3]. In contrast to direct infrared (IR) excitation of the vibrational modes, spontaneous Raman scattering can be achieved

with visible laser wavelengths, significantly increasing the imaging resolution due to being able to use shorter frequency light. However, spontaneous Raman faces severe limitations. Light interacts weakly with Raman vibrations, which is represented by the small Raman cross section per molecule – on the order of $\sigma_R \approx 10^{-30}\,\mathrm{cm}^2$. The weak cross section translates into low scattering rates which necessitates long exposure times that restrict the bio-dynamics that can be studied with spontaneous Raman scattering as well as becoming a practical limitation for experimental work. For example, illumination of a molecule with a 1 Watt light beam focused to a diameter of $150\,\mu$m leads to less than one photon scattered by the spontaneous Raman process every hour. This means that a large flux of photons, i.e., large incident laser power, is required to achieve enough Raman scattering events to detect the Stokes/anti-Stokes shifted photons and collect them to create an image, but this must be balanced with the photodamage limitations of biological samples. While the Raman scattering rates will vary based on the specific beam powers, wavelengths, molecular species, and vibrational frequencies, the numbers are always of a similar order of magnitude. Thus, despite the power of spontaneous Raman scattering, the technique is severely limited for biological applications. Visible pump light will also excite endogenous fluorophores, creating a fluorescent background that can be difficult to filter out from the desired Stokes/anti-Stokes shifted light, leading to a Raman spectrum that is nearly invisible on top of a large fluorescent background.

The usefulness of chemically-sensitive, label-free imaging with spontaneous Raman motivated the pursuit of coherent Raman scattering techniques that could overcome the primary drawback of spontaneous Raman scattering–weak signals that limit imaging speeds and applications. Coherent Raman techniques such as Stimulated Raman Scattering (SRS) and coherent anti-stokes Raman Scattering (CARS) are nonlinear processes where a specific vibrational mode can be coherently driven, vastly increasing the signal levels of the Raman scattered light. Resonant excitation of Raman vibrational modes using coherent techniques can boost the Raman signal by a factor of up to 10^6. Increased signal levels allow for much faster detection rates and enable high-speed (video-rate) imaging of biological systems with optical power levels that do not damage the sample [4].

Coherent Raman scattering enables label-free imaging and spectroscopy of dynamic biological systems.

While spontaneous Raman scattering is a linear optical interaction with one input photon and one scattered photon, coherent Raman techniques such as SRS and CARS involve a third order nonlinear process where the sample interaction involves multiple photons to resonantly excite specific Raman vibrational modes. SRS and CARS require more complex experimental setups from the laser sources to signal detection schemes. CRS techniques require lasers in order to drive the nonlinear interaction and multiple beams with tunable frequencies (pump and Stokes) in order to resonantly drive particular Raman vibrational modes. CARS is a four-wave mixing process where a coherent signal is generated at the anti-Stokes wavelength, making detection and optical filtering of the signal relatively straightforward. The SRS signal is observed as either a stimulated Raman loss or gain (SRL/SRG) using the pump or Stokes beam, respectively. The stimulated Raman loss/gain is a small signal on top of a large background from the pump/Stokes beams and is best detected using modulation transfer and lock-in detection. While CRS techniques dramatically increase the detected signal, the overall sensitivity and limit of detection restricts what kind of samples can be interrogated. The detection sensitivity (SRS/CARS: $\sim \mathrm{mM}$) is not low enough to track inter/intracellular activity and chemical communication because the molecular concentration is significantly lower than the limit of detection. CRS techniques excel at targeting molecular vibrations in the biological "fingerprint" region of Raman vibrations $(200\,\mathrm{cm}^{-1} - 1800\,\mathrm{cm}^{-1})$, or higher vibrational modes associated with C-H stretches in lipids $(2800\,\mathrm{cm}^{-1} - 3200\,\mathrm{cm}^{-1})$. CRS excites molecular vibrations using a pump (ω_p) and Stokes (ω_s) beam where the frequency difference between the two beams matches the energy of an excitable vibrational mode. Higher frequency vibrations require a larger difference in frequency between the two input beams. Practical experimental considerations such as quality of optical filtering limits how low of a Raman vibration $(< 200\,\mathrm{cm}^{-1})$ can be coherently driven and detected with the pump/Stokes beams. Low frequency Raman vibrations are difficult to access with SRS and CARS, yet this spectral region can provide valuable information on larger molecular movements and deformations. These modes

are generally associated with large reduced mass and correspond to vibrational motion that occurs over an extended region. Such relevant motions include virus capsid vibrations, [5] deformations of proteins, [6] and mechanical properties of solids, particularly for soft [7] and two-dimensional materials [8, 9].

This work is focused on developing high-sensitivity label-free spectroscopy and imaging techniques using impulsive stimulated Raman scattering (ISRS) to study biological systems. ISRS is a pump-probe experiment in which the pump pulse simultaneously excites all Raman-active modes with vibrational periods longer than the temporal duration of the pump pulse. A challenge is that this method requires precise control over pulse compression to maintain short pulses. While this style of coherent excitation has limitations in the high-frequency vibrational region ($1800\,\mathrm{cm}^{-1}$ requires an $18\,\mathrm{fs}$ optical pulse), it excels at exciting molecular vibrations in the hard-to-measure low frequency region ($< 200\,\mathrm{cm}^{-1}$). In this work we will show high-sensitivity Raman spectroscopy across the fingerprint region using impulsive Raman scattering as well as work to focus on detection of the low-frequency region using phase-sensitive detection.

This work will first address the most common form of ISRS detection where a vibrational coherence-modulated energy exchange between the sample and a probe pulse is detected with a simple optical filter and photodiode using lock-in detection. This form of detection has limitations in applications to biological samples that can be highly scattering (tissue). To alleviate this problem, we introduce a modification to the typical polarization-based pump rejection scheme by clipping the overlapping pump and probe spectra in order to allow dichroic rejection of the pump beam after the sample. This dramatically increases the robustness of spectral filter based ISRS and makes it a viable technique for spectroscopy and imaging in scattering samples. The interferometric impulsive Raman (phase-sensitive Raman) scheme utilizes a pair of phase-stable probe pulses to preferentially excite low frequency Raman modes, amplifying one of ISRS excitation's primary benefits. The phase-stable relationship between the probe and reference pulses also makes this technique robust against scattering samples while excelling at detecting very low frequency Raman vibrational modes. In order to push the sensitivity limits of impulsive Raman scattering

we developed Doppler Raman spectroscopy where a vibrational coherence-modulated frequency shift of the probe pulse is converted into time-delay that can be very accurately measured with RF electronics. Doppler Raman is demonstrated across the fingerprint region with biological samples and a limit of detection is established (sub mM) that pushes impulsive Raman sensitivity closer to being able to track intracellular dynamics where molecular concentrations are in the nM to uM range. The impact of this work on the landscape of coherent Raman techniques and biology will be discussed. Coherent Raman techniques are experimentally complex, future work will focus on efforts to simplify these experiments and detection schemes in order to make them more robust and to begin applying these techniques to biological systems.

As noted above, ISRS is a pump/probe time-resolved technique where a broadband ultrafast pump pulse excites a vibrational coherence in the sample and a time-delayed probe pulse is incident on the excited sample in order to detect the molecular vibrations. Unlike SRS or CARS, where the pump and Stokes fields are separate laser beams with different frequencies, ISRS employs a broadband femtosecond pulse that contains the pump and Stokes frequencies within a single optical pulse. Because the pump and probe beams overlap spectrally and are collinear, they are arranged to be orthogonally polarized and the pump beam is rejected after the sample using a polarizer. It is critical to completely eliminate the pump beam after the sample before detection to prevent pump contamination and large background signals using lock-in detection. Pump rejection using polarization works very well with simple samples such as some crystals, transparent liquid samples (solvents, amino acids), and thin samples. When attempting to perform spectroscopy or to image more complex samples like biological cells/tissue, crystals that exhibit birefringence, or heterogenous liquids, the polarization-based pump rejection fails. The scattering and birefringent samples depolarize the pump beam and upon exiting the sample, and the pump beam is no longer cleanly rejected by a polarizer. The residual pump is collected by the photodiode and because the pump is carrying the lock-in modulation, but not the Raman spectral information, it creates significant background signals that can completely obscure the Raman spectral information on the probe beam. To address this problem, we developed Split-Spectrum Impulsive Raman where the

same laser system is used, but by utilizing complementary ultrasteep edgepass spectral filters on the pump beam and after the sample, the pump can be spectrally rejected using a dichroic filter, independent of the polarization state. This modification dramatically increases the robustness of impulsive Raman imaging in scattering and complex samples.

Interferometric Raman, or phase-sensitive Impulsive Stimulated Raman Scattering (ϕ-ISRS), is a technique that allows for more sensitive measurement of low-frequency vibrational modes. Because ϕ-ISRS is an interferometric technique, it is directly sensitive to the time-dependent change in the linear optical susceptibility due to the excited vibrational coherence. Other phase-senstivie ISRS techniques have been developed, but they have been unable to probe complex or scattering samples. ϕ-ISRS uses a common-path phase-stable pair of probe pulses to interrogate the excited vibrational coherence. The probe pulse pair is generated using a birefringent crystal and because of the common-path configuration, the ϕ-ISRS measurement is robust to scattering. ϕ-ISRS spectroscopy is demonstrated through a large number of scattering layers and stage-scanning imaging of complex samples is shown.

CRS techniques significantly amplify the Raman scattering signal, allowing for rapid imaging, but the limit of detection for Raman-active molecules is relatively high. There is a need for high-sensitivity coherent Raman techniques that can be used to do label-free imaging and spectroscopy of dynamic biological systems where the concentrations of particular molecules are relatively low. Doppler Raman is a high-sensitivity coherent Raman technique that uses ISRS to excite a vibrational coherence in the sample, then the coherence-modulated probe pulse is subjected to large amounts of dispersion in order to convert a spectral frequency shift caused by the time-varying index of refraction of the excited sample to a timing delay measurement. By converting the optical frequency shift into a timing delay, the measurement noise floor is not limited by the amplitude noise of the laser, expressed as the relative intensity noise (RIN), but is instead limited by the phase noise of the mode-locked laser, which is much lower than the RIN. RF metrology techniques are utilized to measure small timing variations that are directly proportional to the concentration of Raman-active molecules in the focal volume.

Chemically sensitive, label-free spectroscopy and microscopy is a critical tool for the study of many complex and dynamic biological systems. The development of the ISRS techniques in this thesis represent important steps forward in addressing the ability to interrogate Raman vibrations in complex and scattering samples, particularly low frequency Raman modes. In addition to expanding the robustness of ISRS in scattering samples, work was done to improve the overall sensitivity of ISRS and demonstrate an improved limit of detection for ISRS, so that lower concentrations of molecular species can be detected. While Doppler Raman is a high-sensitivity technique, it is also experimentally complex. Future work will involve integrating the scattering-resistant techniques into high-speed imaging systems and complementing the Raman scattering techniques with other measurements. It is important to continue simplifying the complex ISRS experiments as much as possible to increase their utility and ease of use.

Chapter 2

Background

2.1 Microscopic to Macroscopic Nonlinear Response

A coherent Raman interaction is a four-wave mixing process between three incident fields and the coherently Raman scattering (CRS) signal that is detected. Because CRS is a four-wave mixing process, in order to model the interaction we begin by considering the third-order nonlinear polarization density $P^{(3)}$. We want to examine the macroscropic polarization density, so we first start with modeling the interaction between a single molecule and an intense, non-resonant field and consider the induced electric dipole moment in that molecule:

$$\mu = \mu_0 + \alpha E + \frac{1}{2}\beta E^2 + \frac{1}{6}\gamma E^3$$

Where μ_0 is the permanent dipole moment, α is the polarizability, β is the second hyperpolarizability, and γ is the second hyperpolarizability, and higher order terms in the dipole moment have been suppressed. The field E that drives the induced dipole is a real electric field that we will assume is a short laser pulse. The third order component, $\gamma^{(3)}$, the second hyperpolarizability, is the single molecule analog to the third order macroscopic polarization density, $P^{(3)}$. In order to translate the microscopic model given above into a microscope lab frame, we must take into account the number density of molecules, N, and the local field correction, f for each field. We must also project the polarizabilities from the local tensor frame ($IJKL$ indices) to the lab coordinates ($ijkl$ indices). To evaluate the third-order response, we connect the microscopic dipole moment to the macroscopic polarization density using a rotation matrix $\mathbf{R}$ and direction cosines, r_{ab}. Because CRS is a four-wave mixing process, we focus on the third order nonlinear susceptibility, which in the lab frame is [10]

$$\chi^{(3)}_{ijkl} = \frac{N}{\epsilon_0}\gamma_{IJKL} f_i f_j f_k f_l \int r_{iI}\, r_{jJ}\, r_{kK}\, r_{lL}\, G(\Omega)\, d\Omega := \frac{N}{\epsilon_0}\langle\gamma\rangle_{ijkl}.$$

The optical frequency arguments in the local field correction factors, the polarizability terms, and the nonlinear susceptibility are being suppressed for simplicity of notation. In lab coordinates, we write the third order macroscopic polarization density as

$$\chi^{(3)} = \frac{N}{\epsilon_0}\langle\gamma^{(3)}\rangle.$$

2.2 Simple Harmonic Oscillator

The induced molecular vibrations resulting from the incident electric field can cause fluctuations in the polarizability of the molecule. The molecular vibrations can be modeled by decomposing the molecular motions into an approximately normal set of displacements. Under the conditions of a weak excitation by the incident electric field, the motion of the atoms of the molecule can be modeled as a simple harmonic oscillator.

$$mg - kx_0 = 0$$

$$\frac{d^2x}{dt^2} + \omega_0^2 x = 0$$

where $\omega_0 = \sqrt{k/m}$ is the system resonant frequency. Consider the mass experiences a damping friction force $F = -2\gamma m(dx/dt)$ where γ is the damping coeffienct. The differential equation describing the mass movment is then

$$\frac{d^2x}{dt^2} + 2\gamma\frac{dx}{dt} + \omega_0^2 x = 0$$

$$F = E_0 \cos^2(\omega t)$$

The mass movement equation then becomes

$$\frac{d^2x}{dt^2} + 2\gamma\frac{dx}{dt} + \omega_0^2 x = \frac{F(t)}{m}$$

The atomic displacement can be modeled with a damped simple harmonic oscillator (SHO), which obeys the differential equation

$$m\frac{\mathrm{d}^2x(t)}{\mathrm{d}t^2} + 2\,m\,\gamma\,\frac{\mathrm{d}x(t)}{\mathrm{d}t} + m\,\omega_r^2\,x(t) = F(t)$$

where m is the reduced mass of the vibrational mode, Γ_v is the damping constant, $\omega_r = \sqrt{k/m}$ is the resonant frequency, $F = -kx$ is the linear restoring force, and k is the spring constant. The normal modes of the molecule are generally written in the mass-weighted coordinates

$$Q(t) = \sqrt{m}\,x(t).$$

The differential equation for the SHO now reads

$$\sqrt{m}\,\frac{\mathrm{d}^2Q(t)}{\mathrm{d}t^2} + 2\,\Gamma_v\sqrt{m}\,\frac{\mathrm{d}Q(t)}{\mathrm{d}t} + \omega_r^2\sqrt{m}\,Q(t) = F(t)$$

which simplifies to

$$\frac{\mathrm{d}^2Q(t)}{\mathrm{d}t^2} + 2\Gamma_v\frac{\mathrm{d}Q(t)}{\mathrm{d}t} + \omega_r^2\,Q(t) = \frac{1}{\sqrt{m}}\,F(t).$$

The driving term, $F(t)$, can be determined by considering the electric dipole induced on a single molecule by an applied electric field

$$\mu(t) = \vec{\alpha}\cdot\mathbf{E}\vec{(}t)$$

with the incident real field

$$\vec{\mathbf{E}}(t) = \vec{\mathbf{E_0}}\cos(\omega t)$$

the potential energy of the electric dipole is

$$U(t) = -\mu(t) \cdot \vec{\mathbf{E}}(t).$$

the force of the dipole is computed as

$$\vec{\mathbf{F}}(t) = -\nabla U(t) = \nabla \left(\mu(t) \cdot \vec{\mathbf{E}}(t) \right)$$

and for the case of the induced dipole of a single molecule, we then have

$$\vec{\mathbf{F}}(t) = \nabla \left(\vec{\mathbf{E}}(t) \cdot \vec{\alpha} \cdot \vec{\mathbf{E}}(t) \right).$$

We will assume that the electric field is uniform in space over relevant length scales. We can then write

$$\vec{\mathbf{F}}(t) = \vec{\mathbf{E_0}} \cdot \nabla \vec{\alpha} \cdot \vec{\mathbf{E_0}} \cos^2(\omega t)$$

which can be rewritten as

$$\vec{\mathbf{F}}(t) = \vec{\mathbf{E_0}} \cdot \nabla \vec{\alpha} \cdot \vec{\mathbf{E_0}} \left(\frac{1}{2} + \frac{1}{2} \cos(2\omega t) \right)$$

along a given displacement direction (normal coordinates), we write

$$\vec{\mathbf{F}} = \vec{\mathbf{E_0}} \cdot \frac{\delta \vec{\alpha}}{\delta x} \cdot \vec{\mathbf{E_0}} \left(\frac{1}{2} + \frac{1}{2} \cos(2\omega t) \right)$$

Because the frequency of the incident electric field is much higher than the frequency of the Raman vibrational modes ($\omega_0 >> \Omega_v$) and due to the large nuclear mass, the nuclear motion does not directly respond to the field. The time averaged force is then

$$\langle \vec{\mathbf{F}} \rangle_t = \vec{\mathbf{E_0}} \cdot \frac{\delta \vec{\alpha}}{\delta x} \cdot \vec{\mathbf{E_0}} \left\langle \frac{1}{2} + \frac{1}{2} \cos(2\omega t) \right\rangle_t = \frac{1}{2} \vec{\mathbf{E_0}} \cdot \frac{\delta \vec{\alpha}}{\delta x} \cdot \vec{\mathbf{E_0}}.$$

Rewriting the result in normal coordinates,

$$\langle \vec{\mathbf{F}} \rangle_t = \frac{\sqrt{m}}{\sqrt{m}} \frac{1}{2} \vec{\mathbf{E_0}} \cdot \frac{\delta \vec{\alpha}}{\delta x} \cdot \vec{\mathbf{E_0}} = \sqrt{m} \frac{1}{2} \vec{\mathbf{E_0}} \cdot \frac{\delta \vec{\alpha}}{\delta Q} \cdot \vec{\mathbf{E_0}}$$

which can be rewritten as

$$\frac{1}{\sqrt{m}} \langle \vec{\mathbf{F}} \rangle_t = \frac{1}{2} \vec{\mathbf{E_0}} \cdot \frac{\delta \vec{\alpha}}{\delta Q} \cdot \vec{\mathbf{E_0}}.$$

Now that we have the SHO differential equation and the driving force for Raman excitation expressed in normal mode coordinates, we can examine the SHO differential equation for driven normal mode vibrations.

The incident electric field in the driving term is assumed to be a real field, which we can write as:

$$\vec{\mathbf{E}}(t) = \vec{\mathbf{E_0}} \cos(\omega t + \phi) = \frac{1}{2} \vec{\mathbf{E_0}} e^{i\phi} e^{i\omega t} + \text{c.c.} \equiv \frac{1}{2} A e^{i\omega t} + \text{c.c.}$$

where the complex field amplitude is defined as

$$\vec{\mathbf{A}} = \vec{\mathbf{E_0}} e^{i\phi}$$

for a pulse, the envelope is time-varying, and can be written as

$$\vec{\mathbf{A}}(t) = \vec{\mathbf{E_0}}(t) e^{i\phi(t)}.$$

Using the notation where the k^{th} field has a peak amplitude of A_k and a complex field envelope of $u(t)$,

$$\vec{\mathbf{A}}(t) = \vec{\mathbf{A}}_k u(t)$$

and the intensity of the field is given by

$$I(t) = \frac{1}{2}\mathrm{nc}\epsilon_0|\vec{\mathbf{A}}_k|^2$$

where the peak intensity is

$$|\vec{\mathbf{A}}_k|^2 = \frac{2I_k}{\mathrm{nc}\epsilon_0}.$$

Ignoring polarization, scalar fields can be used. The interaction of the incident fields (pump and Stokes) with a Raman active molecule results in the fields exerting a force along the vibrational coordinate direction Q_j. We consider two input fields

$$E_k(t) = \frac{1}{2}A_k u(t)e^{-i\omega_k t} + \frac{1}{2}\mathrm{c.c.}$$

Recall that the frequencies ω_k are much higher than the vibrational frequency Ω_v so the nuclear modes will not be driven efficiently by the incident fields. For sufficiently strong fields, nonlinear motion of the nuclear coordinates can be driven at the difference frequencies between the two incident fields, $\Omega = \omega_2 - \omega_1$ for $k \in \{1, 2\}$. The electric field product is then

$$E_1(t)\,E_2(t) = \frac{1}{4}\left(A_1 u(t)e^{-i\omega_1 t} + \mathrm{c.c.}\right)\left(A_2 u(t)e^{-i\omega_2 t} + \mathrm{c.c.}\right)$$

where it is assumed that the fields have normalized amplitudes that are identical and may be complex, where $|u(t=0)| = 1$.

Expanding we have,

$$E_1(t)\,E_2(t) = \frac{1}{4}\Big\{A_1 A_2\,u^2(t)\,e^{-i(\omega_1+\omega_2)t}\Big\} + \frac{1}{4}\Big\{A_1^* A_2\,|u(t)|^2\,e^{-i(\omega_1+\omega_2)t}\Big\} + \mathrm{c.c.}$$

The combined optical field exerts a force on the vibrational oscillator from the frequency difference fields:

$$F(t) = \frac{1}{2}\left(\frac{\delta\alpha}{\delta Q}\right)_0 |u(t)|^2\left\{A_1^* A_2 e^{-i\Delta\Omega t} + \mathrm{c.c.}\right\}.$$

If we consider the time-average of the force driven by the total field, where the field reads

$$\vec{\mathbf{E}}(t) = \vec{\mathbf{E}}_1|u(t)|\cos\left(\omega_1 t + \phi(t) + \varphi_1\right) + \vec{\mathbf{E}}_2|u(t)|\cos\left(\omega_2 t + \phi(t) + \varphi_2\right).$$

and assuming scalar fields, we can write

$$\vec{\mathbf{F}}(t) = \frac{1}{2}\nabla\alpha\left[E_1|u(t)|\cos\left(\omega_1 t + \phi(t)\right) + E_2|u(t)|\cos\left(\omega_2 t + \phi(t)\right)\right]^2$$

Expanding the term for the force,

$$\begin{aligned}\vec{\mathbf{F}}(t) = \frac{1}{4}\nabla\alpha\,|u(t)|^2\,\big[E_1^2 + E_2^2 + E_1^2\cos\left(2\,\omega_1 t + 2\,\phi_1 + 2\phi(t)\right) + \\ 2E_1E_2\cos\left(2(\omega_1 - \omega_2)\,t + \phi_1 - \phi_2\right) + \\ 2E_1E_2\cos\left(2(\omega_1 + \omega_2)\,t + \phi_1 + \phi_2 + 2\phi(t)\right) + \\ E_2^2\cos\left(2\omega_2 t + 2\phi_2 + 2\phi(t)\right)\big]\end{aligned}$$

Taking a time average of the driving force, the terms with oscillations at the high optical frequencies can be dropped. We now have the difference frequency term,

$$\langle\vec{\mathbf{F}}\rangle_t = \frac{1}{4}\nabla\alpha\,|u(t)|^2\,\left[E_1^2 + E_2^2 + 2E_1E_2\cos\left(\,2\,(\omega_1 - \omega_2)\,t + \phi_1 - \phi_2\right)\right]$$

defining the frequency difference $\Delta\Omega = \omega_1 - \omega_2$ and the phase difference $\Delta\phi = \phi_1 - \phi_2$ we can write

$$\langle\vec{\mathbf{F}}\rangle_t = \frac{1}{4}\nabla\alpha\,|u(t)|^2\,\left[\,|A_1|^2 + |A_2|^2 + 2|A_1||A_2|\cos\left(\Delta\Omega\,t + \Delta\phi\right)\,\right]$$

and we see three terms, two that are driven by the field intensity envelopes, $\langle\vec{\mathbf{F}}\rangle_t \propto |A_1|^2|u(t)|^2$ and $\langle\vec{\mathbf{F}}\rangle_t \propto |A_2|^2|u(t)|^2$ which we can also write as $\langle\vec{\mathbf{F}}\rangle_t \propto I_1(t)$ and $\langle\vec{\mathbf{F}}\rangle_t \propto I_2(t)$.

The impulsive Raman scattering regime is described by these two driving terms that are proportional to the field intensity envelope and will drive molecular vibrations (and/or rotations) that

have temporal vibrational periods that are longer than the pulse duration. The other term in the driving force expression describes normal stimulated Raman scattering. By convention, we will call the higher frequency field the pump (ω_1) and the lower frequency field the Stokes (ω_2). The Raman vibrations are strongly driven when the difference frequency $\Delta\Omega$ matches a vibrational frequency $\Omega_{v,j}$ of the molecule. The temporal envelope of the interfering pulses will excite a band of vibrational frequencies centered on $\Delta\Omega$ over a spectral range inversely proportional to the pulse duration, $\delta\Omega \approx 1/\tau_p$. That is, again the vibrational frequencies with periods longer than the pulse duration will be excited by the interfearing pulse envelope.

Now that we have an expression for the driving force with the real electric fields, we want to determine the driving terms for the forced SHO. To first summarize, we will write out the equation we wish to solve using the real electric field expressions and pulse intensity definitions. The pulse intensities are written as

$$\frac{1}{2}|A_1|^2 = \frac{I_1}{\mathrm{n}_1 c\, \epsilon_0}$$

where n_1 is the local index of refraction, c is the speed of light, and ε_0 is vacuum electric permitivity constant. The pulse intensity is similar for the second field (Stokes field). The mixing term for the pulses can be written as

$$|A_1|\,|A_2| = \frac{2\sqrt{I_1 I_2}}{\sqrt{\mathrm{n}_1 \mathrm{n}_2}\, c\, \epsilon_0}\,|u(t)|^2\,\cos\left(\Delta\Omega\, t + \Delta\phi\right).$$

the time-averaged (cycle-averaged) driving force with our expressions for the fields is then

$$\frac{1}{\sqrt{m}}\langle\vec{\mathbf{F}}\rangle_t = \frac{1}{2}\left(\frac{\delta\alpha}{\delta Q}\right)_0 |u(t)|^2\left[\frac{1}{2}|A_1|^2 + \frac{1}{2}|A_2|^2 + |A_1||A_2|\cos\left(\Delta\Omega t + \Delta\phi\right)\right].$$

The differential equation governing the molecules normal mode displacement can then be written with the expression for the time-averaged force,

$$\frac{\mathrm{d}^2Q(t)}{\mathrm{d}t^2} + 2\Gamma_v \frac{\mathrm{d}Q(t)}{\mathrm{d}t} + \Omega_v^2\, Q(t) = \frac{1}{2}\left(\frac{\delta\alpha}{\delta Q}\right)_0 |u(t)|^2 \left[\frac{1}{2}|A_1|^2 + \frac{1}{2}|A_2|^2 + |A_1||A_2|\cos\left(\Delta\Omega\, t + \Delta\phi\right)\right].$$

Written in terms of intensities the differential equation becomes,

$$\frac{\mathrm{d}^2Q(t)}{\mathrm{d}t^2} + 2\Gamma_v \frac{\mathrm{d}Q(t)}{\mathrm{d}t} + \Omega_v^2\, Q(t) = \frac{1}{c\,\epsilon_0}\left(\frac{\delta\alpha}{\delta Q}\right)_0 |u(t)|^2 \left[\frac{I_1}{\mathrm{n}_1} + \frac{I_2}{\mathrm{n}_1} + 2\sqrt{\frac{I_1 I_2}{\mathrm{n}_1\mathrm{n}_2}}\cos\left(\Delta\Omega\, t + \Delta\phi\right)\right].$$

We now wish to find solutions for the driven SHO differential equation for the two cases of interest. The two cases we will consider are for impulsive stimulated Raman excitation: $\Delta\Omega = 0$ and stimulated Raman excitation: $\Delta\Omega \neq 0$.

2.3 Green's Function: Impulse Response

First the impulsive Raman case ($\Delta\Omega = 0$) where the differential equation can be written as

$$\frac{\mathrm{d}^2Q(t)}{\mathrm{d}t^2} + 2\Gamma_v \frac{\mathrm{d}Q(t)}{\mathrm{d}t} + \Omega_v^2\, Q(t) = \Gamma_1\, \mathrm{d}(t)$$

where we have defined

$$A_1 = \left(\frac{\Phi_1}{2\,\mathrm{n}_1\, c\,\epsilon_0}\right)\left(\frac{\delta\alpha}{\delta Q}\right)_0$$

and we have used the pulse fluence

$$\Phi_1 = \int_{-\infty}^{\infty} I_1(t)^2\,\mathrm{d}t = I_1 \int_{-\infty}^{\infty} |u(t)|^2\,\mathrm{d}t = I_1 U_0$$

where we have written the integral over the normalized pulse intensity profile as

$$U(\Omega) = \int_{-\infty}^{\infty} |u(t)|^2 e^{-i\Omega t}\,\mathrm{d}t \rightarrow U(0) = \int_{-\infty}^{\infty} |u(t)|^2\,\mathrm{d}t \equiv U_0$$

and the finally we define the term

$$\mathrm{d}(t) = \frac{1}{U_0}|u(t)|^2.$$

The case of stimulated Raman excitation ($\Delta\Omega \neq 0$) has a driving term of:

$$\frac{\mathrm{d}^2 Q(t)}{\mathrm{d}t^2} + 2\Gamma_v \frac{\mathrm{d}Q(t)}{\mathrm{d}t} + \Omega_v^2\, Q(t) = \Gamma_2\,\mathrm{d}(t)\cos\left(\Delta\Omega\, t + \Delta\phi\right) \equiv \Gamma_2\,\mathrm{d}_2(t)$$

where we have defined

$$A_2 = \left(\frac{U_0}{c\,\epsilon_0}\sqrt{\frac{I_1 I_2}{\mathrm{n}_1\mathrm{n}_2}}\right)\left(\frac{\delta\alpha}{\delta Q}\right)_0$$

and where

$$\mathrm{d}_2(t) = \mathrm{d}(t)\cos\left(\Delta\Omega\, t + \Delta\phi\right).$$

We will seek solutions to the differential equations in the frequency domain, so we may write

$$Q(t) = \frac{1}{2\pi}\int \hat{Q}(\Omega)\, e^{i\,\Omega\, t}\,\mathrm{d}\Omega$$

$$\mathrm{d}(t) = \frac{1}{2\pi}\int D(\Omega)\, e^{i\,\Omega\, t}\,\mathrm{d}\Omega$$

where we have

$$D(\Omega) \equiv \frac{1}{D_n}\int |u(t)|^2\, e^{-i\,\Omega\, t}\,\mathrm{d}t$$

where $D(\Omega)$ describes the relative power spectral density of the excitation strength of the vibrational mode. Note that $D(0) = 1$, which implies that

$$D_n \equiv \int |u(t)|^2 \, \mathrm{d}t.$$

Substituting the frquency domain expressions into the SHO equation for the normal vibrational coordinate displacement, we obtain

$$\left\{\Omega_v^2 - \Omega^2 + i\,2\,\Gamma_v\,\Omega\right\}\hat{Q}(\Omega) = \Gamma\,D(\Omega)$$

and rearranging, we have

$$\hat{Q}(\Omega) = \frac{\Gamma\,D(\Omega)}{\Omega_v^2 - \Omega^2 + i\,2\,\Gamma_v\,\Omega}.$$

General solutions to the SHO differential equation can be constructed using the impulse response where $\mathrm{d}(t) = \delta(t)$. We can write the differential equation as

$$\frac{\mathrm{d}^2 G(t)}{\mathrm{d}t^2} + 2\Gamma_v \frac{\mathrm{d}G(t)}{\mathrm{d}t} + \Omega_v^2\,G(t) = \delta(t).$$

In the frequency domain, we then have

$$\hat{G}(\Omega) = \frac{1}{\Omega_v^2 - \Omega^2 + i\,2\,\Gamma_v\Omega} = -\,\frac{1}{\Omega^2 - \Omega_v^2 - i\,2\,\Gamma_v\Omega}$$

and this function has the poles

$$\Omega_\pm = i\,\Gamma_v \pm \sqrt{\Omega_v^2 - \Gamma_v^2}$$

so we can write

$$\hat{G}(\Omega) = -\frac{1}{(\Omega - \Omega_+)(\Omega - \Omega_-)}.$$

The impulse response in the time domain can be found with the inverse Fourier transform

$$G(t) = \mathcal{F}^{-1}\{\hat{G}(\Omega)\} = -\frac{1}{2\,\pi}\int_{-\infty}^{\infty} \frac{e^{i\,\Omega t}}{(\Omega - \Omega_+) - (\Omega - \Omega_-)}\, d\Omega.$$

This integral can be solved by contour integration, yielding the result

$$G(t) = \frac{1}{\widetilde{\Omega}_v}\, e^{-\Gamma_v t}\, \frac{1}{2\,i}\left(e^{i\,\widetilde{\Omega}_v t} - e^{-i\,\widetilde{\Omega}_v t}\right), \text{for } t > 0$$

where we have defined $\widetilde{\Omega}_v = \sqrt{\Omega_v^2 - \Gamma_v^2}$. This can be simplified to

$$G(t) = \frac{e^{-\Gamma_v t}}{\widetilde{\Omega}_v} \sin\left(\widetilde{\Omega}_v t\right), \text{for } t > 0.$$

This solution takes the form of a damped sinusoid. We have now a general form for the solution using the impulse response and we can look to examine the case of impulsive Raman excitation. To construct the solution for the ISRS excitation cases we may use the driving term

$$Q(t) = A\int_{-\infty}^{t} \mathrm{d}(t')G(t-t')\,\mathrm{d}t'.$$

The bounds of the integral enforce the causality of the Green's function. Recall that for the impulsive stimulated Raman excitation, $\Delta\Omega = 0$, and the differential equation reads

$$\frac{\mathrm{d}^2Q(t)}{\mathrm{d}t^2} + 2\Gamma_v\frac{\mathrm{d}Q(t)}{\mathrm{d}t} + \Omega_v^2\, Q(t) = A_1\,\mathrm{d}(t)$$

with the solution given by

$$Q(t) = A_1\int_{-\infty}^{t} \mathrm{d}(t')\, G(t-t')\,\mathrm{d}t'.$$

It will be useful to write out the normalized Green's function

$$G_n(t) = \widetilde{\Omega}_v G(t) = e^{-\Gamma_v t}\sin\left(\widetilde{\Omega}_v t\right),\ \text{for t} > 0$$

defining $\Delta = \frac{\widetilde{\Omega}_v}{\Gamma_v}$ and $\theta = \widetilde{\Omega}_v t$, we can then write

$$G_n(\theta) = e^{-\frac{t}{\Delta}\sin(\theta)}.$$

We can write the normalized Gaussian pulse as

$$|u(t)|^2 = e^{-\left(\frac{t}{\tau_p}\right)^2} \rightarrow e^{-\left(\frac{\theta}{\widetilde{\Omega}_v \tau_p}\right)^2} \rightarrow e^{-\left(\frac{\theta}{T_p}\right)^2}$$

where we have defined $T_p = \widetilde{\Omega}_v \tau_p$. With this normalized Gaussian pulse definition, we find that $U_0 = \sqrt{\pi}\,\tau_p$. The normalized Green's function for the ISRS case is

$$Q_n(\theta) = \int_{-\infty}^{0} \mathrm{d}(\theta')\, G(\theta - \theta')\, \mathrm{d}\theta'$$

This work in this thesis focuses on impulsive Raman excitation, so we will further examine this case of spectral scattering with a single impulse provided by a short pump pulse and we are interested in probing the sample/medium at times after the arrival of the pump pulse. We will assume a Gaussian pulse of the form

$$I_t(t) = I_t |u(t)|^2$$

where we have defined

$$|u(t)|^2 = e^{-(t/\tau_p)^2}$$

where τ_p is the pulse duration. We may write the Gaussian pulse fluence as

$$\Phi_1 = \int_{-\infty}^{\infty} I_1(t)\, \mathrm{d}t = I_1 \int_{-\infty}^{\infty} |u(t)|^2\, \mathrm{d}t = I_1\, U_0 = I_1 \sqrt{\pi}\, \tau_p$$

recalling that $U_0 = \sqrt{\pi}\,\tau_p$, so that we can write

$$\mathrm{d}(t) = \frac{1}{\sqrt{\pi}\,\tau_p}\, e^{-\left(\frac{t}{\tau_p}\right)^2}$$

and we have

$$\Gamma_1 = \left(\frac{\sqrt{\pi}\,\tau_p I_1}{n_1 c\,\epsilon_0}\right)\left(\frac{\delta\alpha}{\delta Q}\right)_0.$$

For the case of ISRS excitation, we consider the integral in the solution found for the SHO differential equation. The integral bounds ensure we can examine the behavior of the medium after the pump pulse has left. Recall our solution will take the form of

$$Q(t) = \Gamma_1 \int_{-\infty}^{\infty} \mathrm{d}(t')G(t-t')\,\mathrm{d}t'$$

where we have found the Green's function

$$G(t) = \Theta(t)\,\frac{e^{-\Gamma_v t}}{\widetilde{\Omega}_v}\sin\left(\widetilde{\Omega}_v t\right), \text{for } t > 0$$

where $\Theta(t)$ is the Heavyside step function to enforce causality.

In the frequency domain we have,

$$\widehat{Q}(\Omega) = A_1 D(\Omega)\widehat{G}(\Omega)$$

and recall that in the frequency domain, the Green's function is

$$\widehat{G}(\Omega) = \frac{1}{\Omega_v^2 - \Omega^2 + i\,2\,\Gamma_v\Omega}.$$

The frequency domain driving excitation density is

$$D(\Omega) = e^{-\frac{1}{4}(\Omega\tau_p)^2}.$$

Now the frequency domain impulsive Raman excitation is

$$\widehat{Q}(\Omega) = \frac{A_1}{\widetilde{\Omega}_v U_0}\,\frac{e^{-\frac{1}{4}(\Omega\,\tau_p)^2}}{\Omega_v^2 - \Omega^2 + i\,2\,\Gamma_v\Omega}$$

and performing an inverse Fourier transform yields the final time-domain result

$$Q(t) = \frac{1}{2\pi}\,\frac{A_1}{\widetilde{\Omega}_v U_0}\int_{-\infty}^{\infty}\frac{e^{-\frac{1}{4}(\Omega\,\tau_p)^2}}{\Omega_v^2-\Omega^2+i\,2\,\Gamma_v\Omega}\,e^{i\,\Omega\,t}\,\mathrm{d}\Omega.$$

Again using contour integration to solve the integral yields the expression

$$G(t) = \frac{1}{\widetilde{\Omega}_v}\,e^{-\frac{1}{4}\left[(\widetilde{\Omega}_v\tau_p)^2-(\Gamma_v\tau_p)^2\right]}\,e^{-\gamma t}\,\sin\left(\widetilde{\Omega}_v\,t-2\Gamma_v\,\widetilde{\Omega}_v\,\tau_p^2\right),\text{for}\,t>0$$

In the case of the usual ISRS approximation, the damping is assumed to be negligible, resulting in,

$$G(t) \approx \frac{1}{\widetilde{\Omega}_v}e^{-\frac{1}{4}\left(\widetilde{\Omega}_v\,\tau_p\right)^2}\,\sin\left(\widetilde{\Omega}_v\,t\right),\text{for}\,t>0$$

This can be put in the familiar form

$$Q(t) = Q_0\,e^{-\gamma\,t}\sin\left(\widetilde{\Omega}_v+\phi_0\right),\text{for}\,t>0$$

where then

$$Q_0 = \frac{1}{\widetilde{\Omega}_v}\,e^{-\frac{1}{4}(\Omega_v\,\tau_p\,)^2}\left(\frac{\sqrt{\pi}\tau_p I_1}{\mathrm{n}_1 c\,\epsilon_0}\right)\left(\frac{\delta\alpha}{\delta Q}\right)_0$$

$$\phi_0 = 2\Gamma_v\widetilde{\Omega}_v\tau_p^2$$

$$\widetilde{\Omega}_v = \sqrt{\Omega_v^2-\Gamma_v^2}.$$

In order to examine the effects of the short pump pulse on the medium, we will consider perturbations to the linear optical susceptibility.

2.4 Perturbation to the Linear Optical Susceptibility

The linear polarization density for a material can be written as

$$P^{(1)}(t) = \epsilon_0 \, \chi^{(1)}(t) \, E(t) = N \, \alpha(t) \, E(t)$$

where we consider the time-dependent polarizability from a single molecule coherently vibrating with a single vibrational mode, which we write as

$$\alpha(t) = \alpha_0 + \left(\frac{\delta \alpha}{\delta Q} \right)_0 Q(t).$$

and we will write the linear susceptibility as

$$\chi^{(1)}(t) = \frac{N}{\epsilon_0} \, \alpha(t) \equiv \chi_0^{(1)} + \delta \, \chi^{(1)}(t).$$

We can write

$$\delta \, \chi^{(1)}(t) = \frac{N}{\epsilon_0} \left(\frac{\delta \alpha}{\delta Q} \right)_0 Q(t)$$

and using the results from above for $Q(t)$, and the maximum displacement we can now write

$$\delta \chi^{(1)}(t) = \frac{N}{\epsilon_0} \left(\frac{\delta \alpha}{\delta Q} \right)_0 Q_0 \, e^{-\Gamma_v \, t} \, \sin\left(\widetilde{\Omega}_v \, t + \phi_0 \right) \equiv \delta \, \chi_0 \, e^{-\Gamma_v t} \sin\left(\widetilde{\Omega}_v t + \phi_0 \right)$$

where we have defined the maximum perterbation to the linear susceptiblity as

$$\delta \chi_0 = \frac{\sqrt{\pi} \, \tau_p I_1 N}{n_1 c \, \Omega_v \, \epsilon_0^2} \left(\frac{\delta \alpha}{\delta Q} \right)_0^2 e^{-\frac{1}{4}(\Omega_v \tau_p)^2}.$$

2.5 Field Propagation Equation

Propagation of light modulated by a nonlinear polarization density is generally approached using nonlinear coupled wave equations. Assuming the incident pump and stokes fields (pulses)

are not depleted, we can limit our interest to the propagation equation for the signal of interest. The general equation for the nonlinear signal propagation is

$$\frac{\mathrm{d}A_n}{\mathrm{d}z} = -i\,\frac{\omega_n D\,\chi^{(3)}}{2\,\mathrm{n_n}\,c} A_a\,A_b\,A_c\,e^{i\Delta k\,z}$$

Our signal of interest for impulsive Raman excitation is the probe field after interacting with the excited vibrational coherence in the medium due to the pump pulse. The propagation equation for the probe field is then

$$\frac{\mathrm{d}A_{pr}}{\mathrm{d}z} = -i\,\frac{\omega_{pr}}{2\,\mathrm{n_{pr}}\,c}\,\delta\chi^{(1)}A_{pr} - i\,\frac{\omega_{pr}}{2\,\mathrm{n_{pr}}\,c}\,\frac{3}{4}\chi^{(3)}_{NR}\,|A_{pr}|^2\,A_{pr}$$

where

$$\delta\chi^{(1)}(t) = \delta\chi_0\,e^{-\,\gamma t}\,\sin\left(\widetilde{\Omega}_v\,t + \phi_0\right).$$

Note that the first term on the right hand side of the propagation equation describes the spectral scattering induced by the Raman vibrational coherence. The second term on the right hand side describes the purely electronic response of the material, resulting in cross-phase modulation (XPM) when the pump and probe pulses are overlapped. We now define

$$\delta\chi_0 = \frac{\sqrt{\pi}\tau_p I_1 N}{n_1\,c\,\Omega_v\epsilon_0^2}\left(\frac{\delta\alpha}{\delta Q}\right)_0^2 e^{-\frac{1}{4}(\Omega_v\tau_p)^2} = -\frac{12\sqrt{\pi}\,\tau_{p1}}{n_1\,c\,\epsilon_0}\Gamma_v e^{-\frac{1}{4}(\Omega_v\tau_{p1})^2}\mathrm{Im}\left[\chi^{(3)}_{VR}(\Omega_v)\right] I_1$$

Note that the XPM term from the non-resonant $\chi^{(3)}$ is the nonlinear refractive index seen in the second term on the right hand side of the propagation equation,

$$\delta\chi^{(3)}_{NR} \approx \frac{3}{4}\chi^{(3)}_{NR}\,|A_{pr}|^2\,.$$

To examine the propagation of the vibrational coherence-modulated probe field, we will assume the field is confined to a focal pill box, a cylinder of length l_{foc} and with a cross-sectional area A_{foc}

and a volume V_{foc}. For simplicity, we also assume that the pulse intensity is uniform in the focal pill box and is zero outside of the focal volume. The focal spot area is

$$A_{foc} = \pi \, \mathrm{w_0}^2$$

where $\mathrm{w_0}$ is is the $1/e$ field radius. The focal interaction length is

$$l_{foc} = \frac{2 \, \pi \, \mathrm{w_0^2}}{\lambda}$$

and the focal volume is

$$V_{foc} = l_{foc} A_{foc} \approx \frac{2 \, \pi \, \mathrm{w_0}^2}{\lambda} \, \pi \, \mathrm{w_0}^2 = \pi \frac{\omega}{c} \, \mathrm{n} \, \mathrm{w_0}^4.$$

We will assume the incident field intensity is I_j and we have a pulsed laser source with a pulse intensity $[W/m^2]$ of

$$I(t) = I_j \left| u(t) \right|^2.$$

The fluence $[J/m^2]$ of the beam is then

$$\Phi = \int I(t) \, \mathrm{d}t = I_j \int \left| u(t) \right|^2 \, \mathrm{d}t = \sqrt{\pi} \, \tau_p \, I_j$$

Assuming a Gaussian pulse of the form used above,

$$\left| u(t) \right|^2 = e^{-\left(\frac{t}{\tau_p} \right)^2}$$

we can evaluate the above definition of the beam fluence using the Gaussian pulse in order to write the total pulse energy $[J]$:

$$\varepsilon_j = A_{foc} \Phi = \sqrt{\pi} \, \tau_p \, A_{foc} I_j = \pi^{\frac{3}{2}} \mathrm{w_0^2} \, \tau_p \, A_{foc} \, I_j.$$

We can find the average power of a train of pulses with a repetition rate of f_R ,

$$p_j = f_R\,\varepsilon_j = A_{foc}\Phi = \sqrt{\pi}\,\tau_p\,f_R\,A_{foc}\,I_j = \pi^{\frac{3}{2}}\,{\mathrm{w_0}}^2\,\tau_p\,f_R\,A_{foc}\,I_j$$

2.6 Impulsive Raman Probe Field Propagation

Recall that we have written out the propagation equation for the probe field after interacting with the medium undergoes impulsive Raman excitation

$$\frac{\mathrm{d}A_{pr}}{\mathrm{d}z} = -i\,\frac{\omega_{pr}}{2\,\mathrm{n_{pr}}\,c}\left(\delta\chi^{(1)} + \frac{3}{4}\chi^{(3)}_{NR}\,|A_{pr}|^2\right)A_{pr}$$

with

$$\delta\chi^{(1)}(t) = \delta\chi_0\,e^{-\,\Gamma_v\,t}\,\sin\left(\widetilde{\Omega}_v\,t + \phi_0\right) \equiv \delta\chi_0\,\mathrm{f}(t\,;\,\tau).$$

$$\delta\chi_0 \approx \frac{\sqrt{\pi}\,\tau_{p1}\,I_1\,N}{\mathrm{n_1}\,c\,\Omega_v\,\epsilon_0^2}\left(\frac{\delta\alpha}{\delta Q}\right)_0^2 e^{-\frac{1}{4}(\Omega_v\,\tau_{p1})^2} = -\,\frac{12\sqrt{\pi}\,\tau_{p1}}{\mathrm{n_1}\,c\,\epsilon_0}\,\Gamma_v\,e^{-\frac{1}{4}(\Omega_v\,\tau_{p1})^2}\,\mathrm{Im}\left[\chi^{(3)}_{VR}\left(\Omega_v\right)\right]I_1$$

and

$$\mathrm{f}(t\,;\tau) \equiv e^{-\Gamma_v\,t}\sin\left(\widetilde{\Omega}_v\,t + \phi_0\right).$$

We can also write the change in the linear susceptibility in terms of the average power of the pump pulse. The power of the pump field is

$$p_1 = \sqrt{\pi}\,\tau_{p1}\,f_R\,A_{foc}\,I_1$$

so we can write

$$I_1 = \frac{p_1}{\sqrt{\pi}\,\tau_{p1}\,f_R\,A_{foc}}$$

putting this into the above equation for the susceptibility, we have

$$\delta\chi_0 \approx -\frac{12\sqrt{\pi}\,\tau_{p1}}{\mathrm{n}_1\,c\,\epsilon_0}\Gamma_v\,e^{-\frac{1}{4}(\Omega_v\tau_{p1})^2}\,\mathrm{Im}\left[\chi^{(3)}_{VR}(\Omega_v)\right]I_1$$

which simplifies to

$$\delta\chi_0 \approx -\frac{1}{f_R}\frac{12}{\mathrm{n}_1\,A_{foc}\,c\,\epsilon_0}\Gamma_v\,e^{-\frac{1}{4}(\Omega_v\tau_{p1})^2}\,\mathrm{Im}\left[\chi^{(3)}_{VR}(\Omega_v)\right]p_1$$

which then gives the set of expressions

$$\delta\chi^{(1)}(t) = \delta\chi_0\,e^{-\,\Gamma_v t}\,\sin\left(\widetilde{\Omega}_v\,t+\phi_0\right) \equiv \delta\chi_0\,\mathrm{f}(t\,;\tau)$$

$$\delta\chi_0 \approx -\frac{1}{f_R}\frac{12}{n_1\,A_{foc}\,c\,\epsilon_0}\Gamma_v\,e^{-\frac{1}{4}(\Omega_v\tau_{p1})^2}\,\mathrm{Im}\left[\chi^{(3)}_{VR}(\Omega_v)\right]p_1$$

$$f(t\,;\tau) \equiv e^{-\Gamma_v\,t}\sin\left(\widetilde{\Omega}_v\,t+\phi_0\right)$$

Propagation of this field gives

$$A_{pr}\left(l_{foc}\right) = A_{pr}(0)\,e^{-i\,\frac{\omega_{pr}}{c}\left(\frac{\delta\chi^{(1)}}{2\,n_{pr}}+\frac{3}{8\,n_{pr}}\chi^{(3)}_{NR}\,|A_{pr}|^2\right)l_{foc}}$$

The nonlinear optical susceptibilities are purely real in this case. When detecting impulsive Raman excitation used in the experiments in this thesis, lock-in detection is employed. Lock-in detection utilizes amplitude modulation on the pump pulse intensity and is sensitive only to signal that carries the applied modulation frequency. Because of this, the only above terms that are detected are those with the pump power intensity, I_1, which is the $\delta\chi^{(1)}$ term. The impulsive Raman excitation creates a perturbation in the linear susceptibility of the medium/sample, resulting

in a small frequency shift that is accumulated by the probe pulse. Detecting this small frequency shift gives the Raman signal from the sample.

2.7 Raman-Induced Phase Shift

In this work, we utilize a time-delayed probe pulse that is the same temporal duration as the pump pulse used to excite a vibrational coherence through impulsive stimulated Raman excitation (ISRE). The probe pulse arrives at a time delay of τ relative to the pump pulse. The probe pulse experiences a time-varying linear susceptibility (a time varying refractive index) that produces a local phase shift

$$\phi(t) = \delta\phi_0\, e^{-\Gamma_v t} \sin\left(\widetilde{\Omega}_v\, t + \phi_0\right), \text{for } t > 0$$

The relevant effects occur locally in time around τ. To examine the effects, we perform a Taylor expansion about $t - \tau$

$$\begin{aligned}\phi(t-\tau) \approx{}& \delta\phi_o\, e^{-\Gamma_v \tau} \sin\left(\widetilde{\Omega}_v\, \tau + \phi_0\right) \\ &- \Gamma_v\, \delta\phi_0\, e^{-\Gamma_v \tau}\, \sin\left(\widetilde{\Omega}_v\, \tau + \phi_0\right)(t-\tau) \\ &+ \widetilde{\Omega}_v\, \delta\phi_0\, e^{-\Gamma_v \tau}\, \cos\left(\widetilde{\Omega}_v\, \tau + \phi_0\right)(t-\tau).\end{aligned}$$

Because $\gamma << \widetilde{\Omega}_v$, we may neglect the middle term,

$$\phi(t-\tau) \approx\ \delta\phi_o\, e^{-\Gamma_v \tau} \sin\left(\widetilde{\Omega}_v\, \tau + \phi_0\right) + \widetilde{\Omega}_v\, \delta\phi_0\, e^{-\Gamma_v \tau}\, \cos\left(\widetilde{\Omega}_v\, \tau + \phi_0\right)(t-\tau)$$

where the maximum phase shift is

$$\delta\phi_0 = \frac{\omega_{pr}}{c} \frac{l_{foc}}{2\,\mathrm{n_{pr}}}\, \delta\chi^{(1)} = \frac{\pi}{\mathrm{n_{pr}}} \frac{l_{foc}}{\lambda_{pr}}\, \delta\chi^{(1)}$$

Using the expressions from above, the maximum phase shift can be written a number of ways:

$$\delta\phi_0 = \frac{\pi^{\frac{3}{2}}\tau_{p_1}}{\mathrm{n_1\,n_{pr}}\,c\,\Omega_v\,\epsilon_0^2}\,e^{-\frac{1}{4}(\Omega_v\,\tau_{p_1})^2}\left(\frac{l_{foc}}{\lambda_{pr}}\right)N\left(\frac{\delta\alpha}{\delta Q}\right)_0^2 I_1$$

$$\delta\phi_0 = -\frac{12\,\pi^{\frac{3}{2}}\,\Gamma_v\,\tau_{p_1}}{\mathrm{n_1\,n_{pr}}\,c\,\epsilon_0}\,e^{-\frac{1}{4}(\Omega_v\,\tau_{p_1})^2}\left(\frac{l_{foc}}{\lambda_{pr}}\right)\mathrm{Im}\left[\chi_{VR}^{(3)}\left(\Omega_v\right)\right]I_1$$

and a maximum frequency shift of

$$\delta\omega_0 = \widetilde{\Omega}_v\,\delta\phi_0$$

$$\delta\omega_0 = \frac{\pi^{\frac{3}{2}}\tau_{p_1}\widetilde{\Omega}_v}{\mathrm{n_1\,n_{pr}}\,c\,\Omega_v\,\epsilon_0^2}\,e^{-\frac{1}{4}(\Omega_v\,\tau_{p_1})^2}\left(\frac{l_{foc}}{\lambda_{pr}}\right)N\left(\frac{\delta\alpha}{\delta Q}\right)_0^2 I_1$$

$$\delta\omega_0 = -\frac{12\,\pi^{\frac{3}{2}}\,\Gamma_v\,\tau_{p_1}\widetilde{\Omega}_v}{\mathrm{n_1\,n_{pr}}\,c\,\epsilon_0}\,e^{-\frac{1}{4}(\Omega_v\,\tau_{p_1})^2}\left(\frac{l_{foc}}{\lambda_{pr}}\right)\mathrm{Im}\left[\chi_{VR}^{(3)}\left(\Omega_v\right)\right]I_1$$

The aim of RF Doppler Raman detection is to detect as small of a frequency shift, $\delta\omega_0$, as possible. For convenience, we define the term $\beta_{DR} = \Gamma_v\,\widetilde{\Omega}_v\,e^{-\frac{1}{4}\left(\Omega_v\tau_{p_1}\right)^2}$ such that the maximum frequency shift can be written as

$$\delta\omega_0 = \beta_{DR}\,\frac{\pi^{\frac{3}{2}}\tau_{p_1}}{\mathrm{n_1\,n_{pr}}\,c\,\Gamma_v\,\Omega_v\,\epsilon_0^2}\left(\frac{l_{foc}}{\lambda_{pr}}\right)N\left(\frac{\delta\alpha}{\delta Q}\right)_0^2 I_1$$

$$\delta\omega_0 = -\beta_{DR}\,\frac{12\,\pi^{\frac{3}{2}}\,\tau_{p_1}}{\mathrm{n_1\,n_{pr}}\,c\,\epsilon_0}\left(\frac{l_{foc}}{\lambda_{pr}}\right)\mathrm{Im}\left[\chi_{VR}^{(3)}\left(\Omega_v\right)\right]I_1$$

and the maximum frequency shift can also be written (as will be shown later)

$$\delta\omega_0 = -\beta_{DR}\,\frac{2}{f_R}\,\frac{6\,\pi}{\mathrm{n_1\,n_{pr}}\,A_{foc}\,c\,\epsilon_0}\left(\frac{l_{foc}}{\lambda_{pr}}\right)\mathrm{Im}\left[\chi_{VR}^{(3)}\left(\Omega_v\right)\right]p_1.$$

2.8 Measuring Frequency Shift with Spectral Filter

The frequency shift imparted on the probe pulse is identical for each pulse in the pulse train given a fixed pump pulse energy, pulse shape (temporal profile), and relative pump pulse delay. The pulses in the pulse train are separated in time by approximately $10\,\mathrm{ns}$ while the excited vibrational coherences relax on the order of picoseconds. We will model the frequency shift experienced by the probe spectrum as a change in the centroid of a Gaussian spectrum.

One method for detecting the frequency shift is to employ a spectral filter before the detection photodiode. The power detected by the photodiode is some fraction of the total probe power incident on the spectral filter after interacting with the sample. To determine the amount of transmitted power through the spectral filter, first consider the total signal power. Recall that we have defined the pulse intensity profile

$$I(t) = I_0\,|u(t)|^2$$

where the field envelope magnitude reads

$$|u(t)| = e^{-\frac{1}{2}\left(\frac{t}{\tau_p}\right)^2}$$

Assuming that the probe pulse is transform-limited, the spectrum is then

$$U(\Omega) = \sqrt{2\,\pi}\,\tau_p\,e^{-\frac{1}{2}(\Omega\,\tau_p)^2}$$

with a power spectrum given by

$$S(\Omega) = A_{beam}\,I_0\,|U(\Omega)|^2 = 2\,\pi\,\tau_p^2\,A_{beam}\,I_0\,e^{-(\Omega\tau_p)^2} \equiv S_0\,e^{-(\Omega\,\tau_p)^2}$$

where we have defined $S_0 = 2\,\pi\,\tau_p^2 A_{beam}\,I_0$. The total energy is then

$$\varepsilon = \int S(\Omega)\,\mathrm{d}\Omega = S_0 \int e^{-(\Omega\,\tau_p)^2}\mathrm{d}\Omega = \frac{\sqrt{\pi}}{\tau_p}\,S_0.$$

The average power of the probe field is then

$$p_{avg} = f_R\,\varepsilon = \sqrt{\pi}\frac{f_R}{\tau_p}S_0.$$

We wish to examine the shift of the centroid of the power spectrum, such that

$$S(\Omega) \rightarrow S(\Omega - \delta\omega).$$

It will be useful to find the maximum slope of the Gaussian spectrum,

$$\frac{\mathrm{d}\,S(\Omega)}{\mathrm{d}\,\Omega} = -2\,\tau_p^2\;\Omega\;e^{-(\tau_p\Omega)^2}$$

with the maximum located at

$$\left|\frac{\mathrm{d}\,S(\Omega)}{\mathrm{d}\,\Omega}\right|_{\max} = \pm\frac{1}{\sqrt{2}\,\tau_p}.$$

The region of the spectrum with the maximum slope will provide the most sensitivity to the induced optical frequency shift. Consider a spectral edge filter with a transmission of the form

$$g(\Omega) = \Theta(\Omega - \Omega_0)$$

with the probe energy transmitted through the filter given by

$$\varepsilon_e(\delta\omega, \Omega_0) = \int S(\Omega - \delta\omega)\,g(\Omega)\,\mathrm{d}\Omega$$

which can be explicitly written as

$$\varepsilon_e(\delta\omega, \Omega_0) = S_0\int_{\Omega_0}^{\infty} e^{-[(\Omega-\delta\omega)\tau_p]^2}\,\mathrm{d}\Omega.$$

Evaluating this integral, we obtain

$$\varepsilon_e(\delta\omega, \Omega_0) = \frac{\sqrt{\pi}\, S_0}{2\,\tau_p}\,(1 + \mathrm{erf}[\tau_p(\delta\omega - \Omega_0)]).$$

The transmitted energy for a zero frequency shift reads

$$\varepsilon_e(0, \Omega_0) = \frac{\sqrt{\pi} S_0}{2\,\tau_p}\,(1 - \mathrm{erf}[\tau_p \Omega_0])$$

so that the normalized transmission reads

$$\frac{\varepsilon_e(\delta\omega, \Omega_0)}{\varepsilon_e(0, \Omega_0)} = \frac{1 + \mathrm{erf}\,[\tau_p(\delta\omega - \Omega_0)]}{\mathrm{erfc}\,[\tau_p\,\Omega_0]}.$$

The maximum value of the normalized transmission through the filter is then

$$\left.\frac{\varepsilon_e(\delta\omega, \Omega_0)}{\varepsilon_e(0, -\frac{1}{\sqrt{2}\,\tau_p})}\right|_{\max} = \frac{1 + \mathrm{erf}\left[\frac{1}{\sqrt{2}} + \delta\omega\,\tau_p)\right]}{1 + \mathrm{erf}\left[\frac{1}{\sqrt{2}}\right]}$$

where we have positioned the spectral filter at the maximum slope of the Gaussian spectrum.

Because $\delta\omega$ is small, we can look at a series expansion and neglect the higher order terms. We can write

$$\varepsilon_e(\delta\omega, \Omega_0) \approx \varepsilon_e(0, \Omega_0)\left(1 + \frac{2\,e^{-\tau_p^2\Omega_0^2}\,\tau_p\,\delta\omega}{\sqrt{\pi}\,\mathrm{erfc}[\tau_p\,\Omega_0]}\right)$$

and we find for the optimal slope,

$$\varepsilon_e\left(\delta\omega, -\frac{1}{\sqrt{2}\tau_p}\right) \approx \varepsilon_e\left(0, -\frac{1}{\sqrt{2}\tau_p}\right)\left(1 + \frac{2\,\tau_p\delta\omega}{\sqrt{e\pi}\,\left(1 + \mathrm{erf}\left[\frac{1}{\sqrt{2}}\right]\right)} + 0[\delta\omega]^2\right).$$

The experimental signal of interest comes from the difference

$$\Delta\varepsilon_e(\delta\omega, \Omega_0) = \varepsilon_e(\delta\omega, \Omega_0) - \varepsilon_e(0, \Omega_0) = \varepsilon_e(0, \Omega_0)\frac{2\,\tau_p\,\delta\omega\,e^{-(\tau_p\,\Omega_0)^2}}{\sqrt{\pi}\,\mathrm{erfc}[\tau_p\,\Omega_0]}.$$

With this, we can now write an expression for the case of an edge filter which reads

$$\Delta\varepsilon_e = \frac{2\,\tau_{\rm pr}\,e^{-(\tau_p\,\Omega_0)^2}}{\sqrt{\pi}\,{\rm erfc}[\tau_{\rm pr}\,\Omega_0]}\varepsilon_{e_0}\,\delta\omega$$

$$\Delta\varepsilon_e \equiv {\rm C}_e\,\varepsilon_{e_0}\,\delta\omega$$

where we have grouped the constants

$${\rm C}_e = \frac{2\,\tau_{\rm pr}\,e^{-(\tau_p\,\Omega_0)^2}}{\sqrt{\pi}\,{\rm erfc}[\tau_{\rm pr}\,\Omega_0]}$$

and the unshifted edge filter transmitted energy then reads

$$\varepsilon_{e_0} = \frac{\sqrt{\pi}\,S_0}{2\tau_{\rm pr}}\,(1-{\rm erf}[\tau_{\rm pr}\Omega_0])\,.$$

Using the average probe power

$$p_{\rm pr} = f_R\,\varepsilon_{\rm pr} = \sqrt{\pi}\frac{f_R}{\tau_{\rm pr}}\,S_{0_{\rm pr}} \rightarrow S_{0_{\rm pr}} = \frac{\tau_{\rm pr}\,p_{\rm pr}}{\sqrt{\pi}\,f_R}$$

we can write

$$\varepsilon_{e_0} = \frac{\sqrt{\pi}}{2\,\tau_{\rm pr}}\,\frac{\tau_{\rm pr}\,p_{\rm pr}}{\sqrt{\pi}\,f_R}(1-{\rm erf}[\tau_{\rm pr}\,\Omega_0]) = \frac{p_{\rm pr}}{2\,f_R}(1-{\rm erf}[\tau_{\rm pr}\,\Omega_0])$$

which gives the expression for the change in transmitted energy through the filter

$$\varepsilon_{e_0} = \frac{\sqrt{\pi}}{2\,\tau_{\rm pr}}\frac{\tau_{\rm pr}\,p_{\rm pr}}{\sqrt{\pi}\,f_R}(1-{\rm erf}[\tau_{\rm pr}\Omega_0]) = \frac{p_{\rm pr}}{2\,f_R}(1-{\rm erf}[\tau_{\rm pr}\Omega_0])$$

from which we can write the expression for the transmitted energy difference caused by the frequency shift through the spectral filter

$$\Delta\varepsilon_e = \frac{{\rm C}_e}{2\,f_R}(1-{\rm erf}[\tau_{\rm pr}\,\Omega_0])\,\delta\omega_0\,{\rm f}(t;\tau)\,p_{\rm pr} \equiv \frac{{\rm C}_e}{2\,f_R}(1-{\rm erf}[\tau_{\rm pr}\,\Omega_0])\,\delta\omega_0\,{\rm f}(t;\tau)\,p_{\rm pr}.$$

Now we may write the transmitted pulse energy as

$$\Delta\varepsilon_e = \beta_e \, \delta\omega_0 \, \mathrm{f}(t;\tau) \, p_{\mathrm{pr}}$$

where we may write

$$\beta_e = \frac{\mathrm{C}_e}{2\, f_R}(1 - \mathrm{erf}[\tau_{\mathrm{pr}}\, \Omega_0]) = \frac{2\, \tau_{\mathrm{pr}}\, e^{-(\tau_{\mathrm{pr}}\, \Omega_0)^2}}{\sqrt{\pi}\, \mathrm{erfc}[\tau_{\mathrm{pr}}\, \Omega_0]} \, \frac{1}{2\, f_R}(1 - \mathrm{erf}[\tau_{\mathrm{pr}}\, \Omega_0])$$

which simplifies to read

$$\beta_e = \frac{\tau_{\mathrm{pr}}\, e^{-(\tau_{\mathrm{pr}}\, \Omega_0)^2}}{\sqrt{\pi}\, f_R} \left(\frac{1}{\mathrm{erfc}[\tau_{\mathrm{pr}}\, \Omega_0]} - 1 \right).$$

The average power of the transmitted signal then reads

$$p_{\mathrm{R}_e} = f_R \, \Delta\varepsilon_e = f_R \, \beta_e \, \delta\omega_0 \, \mathrm{f}(t;\tau) \, p_{\mathrm{pr}}$$

with the final average power of the ISRE signal given by

$$p_{\mathrm{R}_{\mathrm{avg}}} = \widetilde{\Omega}_v \, f_R \, \beta_e \, \delta\phi_0 \, \mathrm{f}(t;\tau) \, p_{\mathrm{pr}}$$

where the peak phase shift $\delta\phi_0$ is given by

$$\delta\phi_0 = -\frac{6\, \pi\, \Gamma_v}{\mathrm{n}_1\, \mathrm{n}_{\mathrm{pr}}\, f_R\, A_{\mathrm{foc}}\, c\, \epsilon_0} \, e^{-\frac{1}{4}\left(\Omega_v\, \tau_{p_1}\right)^2} \left(\frac{l_{\mathrm{foc}}}{\lambda_{\mathrm{pr}}} \right) \mathrm{Im}\left[\chi^{(3)}_{VR}\left(\Omega_v\right) \right] \, p_1$$

We can write the expression for the ISRE signal collected through the edge spectral filter using the peak phase shift expression

$$p_{\mathrm{R}_e} = \widetilde{\Omega}_v \, f_R \, \beta_e \, \delta\phi_0 \, \mathrm{f}(t;\tau) \, p_{\mathrm{pr}}$$

$$p_{\mathrm{R}_e} = -\widetilde{\Omega}_v \, f_R \, \beta_e \frac{6\,\pi\,\Gamma_v}{\mathrm{n}_1\,\mathrm{n}_{\mathrm{pr}}\,f_R\,A_{\mathrm{foc}}\,c\,\epsilon_0} e^{-\frac{1}{4}\left(\Omega_v\,\tau_{p_1}\right)^2} \left(\frac{l_{\mathrm{foc}}}{\lambda_{\mathrm{pr}}}\right) \mathrm{f}(t;\tau)\,\mathrm{Im}\left[\chi^{(3)}_{VR}(\Omega_v)\right]\, p_1\, p_{\mathrm{pr}}.$$

To relate this to the energy transmitted through the spectral filter for the non-frequency shifted probe pulse, we define the constant

$$p_{ISRE} = -\mathrm{B}_{\mathrm{ISRE}}\,\mathrm{Im}\left[\chi^{(3)}_{VR}(\Omega_v)\right]\, p_1\, p_{\mathrm{pr}}$$

where we have used the scaling coefficient

$$\mathrm{B}_{ISRE} = \beta_e\,\beta_{\mathrm{DR}} \frac{6\,\pi}{\mathrm{n}_1\,\mathrm{n}_{\mathrm{pr}} A_{\mathrm{foc}}\,c\,\epsilon_0} \left(\frac{l_{\mathrm{foc}}}{\lambda_{\mathrm{pr}}}\right) \mathrm{f}(t;\tau)$$

where we have defined

$$\beta_{\mathrm{DR}} = \Gamma_v\,\widetilde{\Omega}_v\,e^{-\frac{1}{4}\left(\Omega_v\,\tau_{p_1}\right)^2}$$

and

$$\beta_e = \frac{\tau_{\mathrm{pr}}\,e^{-(\tau_{\mathrm{pr}}\Omega_0)^2}}{\sqrt{\pi}\,f_R}\left(\frac{1}{\mathrm{erfc}[\tau_{\mathrm{pr}}\,\Omega_0]} - 1\right).$$

As we have shown, using a spectral edge filter is a reliable way to detect the optical frequency shift experienced by the probe spectrum after interacting with the pump-mediated vibrational coherence in the sample. In an effort to expand the utility of the spectral filter detection scheme for biological imaging, we explored ways to make this form of detection more robust to complex samples that can be scattering and depolarizing. In the next chapter the split spectrum detection technique is introduced.

Chapter 3

Split Spectrum Impulsive Raman

Label free optical imaging has been widely developed as a route of observing the concentration and monitoring the dynamics of chemical species without requiring the use of exogenous labels that are susceptible to introducing perturbations to behaviors that one wishes to observe [11]. Label free optical imaging methods exploit differences in electronic or vibrational spectroscopy between molecules to form images that can be used to separate particular chemical species [3, 12] [1].

Raman vibrational spectroscopy is of particular interest because the spectrally narrow Raman features enable reliable hyperspectral decomposition of molecular species. Spontaneous Raman scattering is a simple strategy for label free molecular spectroscopy yet is limited due to the fact that weak Raman cross sections make Raman scattering a rare event. Coherent Raman scattering (CRS) is driven by intense laser fields that increase the rate of Raman scattering by orders of magnitude, enabling rapid imaging with relatively low laser powers [13–15]. The majority of CRS methods use two laser fields (pump and Stokes) that are detuned to efficiently drive stimulated Raman process at a particular vibrational frequency. Such a system generally requires complex, tunable short pulse laser systems. Interest in low frequency Raman spectroscopy and microscopy has grown in recent years due to the untapped potential for probing local material properties and structural properties of large macromolecules [10].

CRS imaging can be considerably simplified by deriving the pump and Stokes fields directly from a single laser pulse by using impulsive stimulated Raman scattering (ISRS) [16]. ISRS is normally implemented in a pump-probe arrangement, where the laser pulse energy is split into a pump pulse followed by a time-delayed probe pulse. The pump pulse prepares a vibrational coherence that leads to a time-varying perturbation to the linear refractive index (RI) [17, 18]. The time-dependent linear RI variation imparts a temporal phase modulation on a probe pulse that

[1] This chapter has been adapted with permission from "Nearly degenerate two-color impulsive coherent Raman hyperspectral imaging," Opt. Lett. 47, 5841-5844 (2022), Optical Society of America.

arrives at the sample at a delay τ after the pump pulse excitation [10]. ISRS signals can then be acquired from myriad strategies, based on diffraction from a transient grating [16], interferometry [19, 20], Kerr lensing and steering [21, 22], an induced transient probe pulse delay [23], or spectral scattering that produces either a change in the probe spectral center of mass or scatters probe energy to new spectral regions [24]. Interest in ISRS methods has recently been revived due to the ability to readily probe low frequency vibrational modes that can be technically challenging to obtain using spontaneous Raman scattering or other CRS methods. Generally CRS allows for recording of one vibrational frequency at a time by tuning the frequency difference between the pump and Stokes fields, which can be speed up with multiplexed methods. Conversely, ISRS spectra can be acquired by recording a time-resolved ISRS signal imparted to the probe pulse as a function of relative probe pulse arrival time τ. The Raman spectrum is obtained from the time-resolved ISRS signal through power spectral density estimators (such as a Fourier transform [20], multitaper estimation [23], or model fitting [19]. The spectrum is obtained from the time-domain signal and thus is an approximately continuous Raman spectrum that spans from a low vibrational frequency $\nu_{min} = 1/\Delta\tau$ bound and spectral resolution set by the duration of the scan $\Delta\tau$ and a maximum vibrational frequency set by the pump and probe pulse durations as described below.

A key requirement of pump-probe ISRS is the ability to block the pump pulse from reaching the probe photodetector. While pump rejection generally is not problematic in non-scattering specimens such as high-quality crystals and transparent fluids, a vast majority of specimens of interest are either depolarizing, scattering, or both. As many strategies rely on isolating the probe pulse spatially through non-collinear propagation [25, 26] or on polarization [19, 27], the widespread application of ISRS to high-resolution imaging has been hindered.

A common strategy for ISRS is to use dichroic optics to separate the pump and probe pulse. [20] The pump and probe pulses can be obtained through frequency doubling of a single pulse or by generation of a separate color pulse with an optical parametric oscillator. Because ISRS methods require the delivery of temporally compressed pulses, the use of multiple color laser pulses brings added system complexity and cost [28].

In this Letter, we introduce a simplified experimental approach for ISRS that enables robust separation of pump and probe pulses derived from a single laser pulse. Our method, illustrated in Fig. 3.1, is inspired by single-pulse coherent anti-Stokes Raman scattering (CARS) methods that use a low pass filtering of the pulse and complementary dichroic filter to collect light scattered to anti-Stokes frequencies [29]. We retain the pump-probe architecture so that we benefit from the use of lock-in amplifier (LIA) detection of the probe signal to suppress noise. Continued development of ultrasteep spectral filters has enabled the use of complimentary long pass and short pass filters to filter and separate the pump and probe fields. To spectrally reject the pump from the collinearly propagating probe pulse, we insert an ultrasteep longpass (USLP) optical filter (Semrock USLP785) into the pump arm before the pump and probe pulses are combined with orthogonal polarization (Fig. 3.1 a)). The full bandwidth of probe pulse is combined with the spectrally clipped pump and is focused onto the sample (Fig. 3.1 b)). After the sample, the pulses are re-collimated and a complimentary ultrasteep short pass (USSP) optical filter (Semrock USSP785), is used to reject the spectrally clipped pump pulse and transmit the high-frequency portion of the probe pulse (Fig. 3.1 c)). The second ultrasteep filter (USSP) also enables amplitude detection of the frequency shift of the probe pulse to record the ISRS spectrum [22, 24, 30].

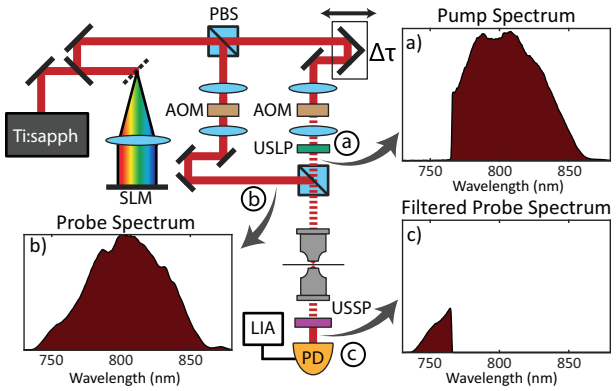

Figure 3.1: Experimental Setup. The pump spectrum is filtered with ultrasteep longpass (USLP) filter (a) while maintaining the full probe spectrum (b). A complimentary ultrasteep short pass (USSP) filter post-sample spectrally rejects pump light while simultaneously providing a spectral edge for the probe to convert frequency modulation to amplitude modulation (c). The grating, lens and spatial light modulator (SLM) are used as a programmable pulse shaper to ensure the delivery of transform-limited pulses at the focus.

The CRS signal arises due to interference between spectral scattering of the probe pulse with the input probe pulse spectrum [10]. The spectral scattering is driven by a time-varying refractive index (RI) produced by the pump pulse that can be expressed as [10]
$\delta n(t) = \delta n_0 \exp(-\Gamma_v t) \sin(\Omega_v t)\, \Theta(t)$. The RI shift decays exponentially with a rate of Γ_v set by the vibrational mode with frequency Ω_v and with a peak amplitude that is readily computed from experimental parameters and the Raman interaction under study. The Heaviside step function, $\Theta(t)$ enforces causality. For a temporally short probe pulse, such that the exponential decay may be neglected for a weak scattering limit encountered in CRS experiments and when temporal walk off can be neglected (i.e. group velocity differences between the pump and probe are negligible), the probe pulse accumulates a sinusoidal temporal phase shift of the form $\phi(t) = \delta\phi_0 \sin(\Omega_v[t+\tau])$, where τ is the pump-probe delay. The sinusoidal phase modulation scatters energy from the input probe pulse spectrum $\hat{E}_{\mathrm{pr}}(\Omega)$ to spectral sidebands, producing a modulated probe spectrum of $\hat{E}_{\mathrm{m}}(\Omega) \approx a_\tau \hat{E}_{\mathrm{pr}}(\Omega - \Omega_v) + \hat{E}_{\mathrm{pr}}(\Omega) - a_\tau \hat{E}_{\mathrm{pr}}(\Omega + \Omega_v)$. The scattered amplitude $a_\tau \approx \delta\phi_0 \exp(i\,\phi_\tau)/2$ depends on pump-probe delay τ, where the accumulated phase is $\phi_\tau = \Omega_v \tau$. [10]

The ultrasteep filters are always set to be complementary. Thus, the choice of the cutoff optical frequency for pump and probe spectral clipping impacts the spectral measurement. When the pump pulse is clipped (by the USLP), as seen in Fig. 3.1 a), the bandwidth and pulse energy are both decreased. The decreased bandwidth stretches the pump pulse in time and reduces the Raman frequency extraction bandwidth. In addition, the decreased pump pulse energy and increased pulse duration also reduce the strength of the Raman excitation, so minimal spectral clipping of the pump pulse is favorable. On the other hand, the ISRS signal is obtained from the transmission of the probe pulse through the second, complementary USSP spectral filter. Because this clipping occurs after the probe pulse has interacted with the sample, there is no concern about the temporal duration of the probe pulse, as the probe pulse contains the full bandwidth within the sample. However, a higher clipping frequency means a reduced probe pulse energy, which reduces the SNR of the measurement.

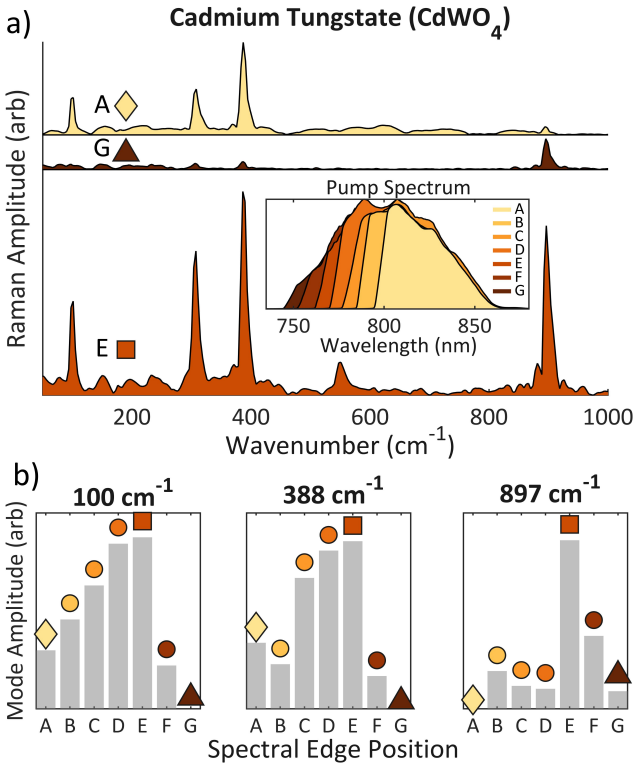

Figure 3.2: (a) Vibrational spectrum response of Cadmium Tungstate ($CdWO_4$) as the complementary spectral edge frequency edge Ω_c is varied. The Raman spectra for three different Ω_c setrings are shown the inset. (b) The mode amplitude for three vibrational frequencies as Ω_c is varied; each probe spectrum is shown in the inset of (a).

We can understand the impact of the tradeoffs in the choice of the complementary filter cutoff frequency with a theoretical model. For purposes of the model, we assume Gaussian pump and probe pulses with the same pulse duration τ_p, written as $E(t) = \exp[-(t/\tau_p)^2]$. The signal is derived from a small change in the average probe pulse power transmitted through the USSP probe filter. The signal power is given by $p_{\rm sig} = \bar{p}_{\rm pr}\,\Delta\eta$, where $\bar{p}_{\rm pr}$ is the average probe pulse power and the differential transmission efficiency $\Delta\eta$ for a high (frequency) pass filter with a cutoff frequency Ω_c. For a weak phase modulation, $(\delta\phi_0 \ll 1)$, the differential filter transmission is given by $\Delta\eta = P_c\,\delta\phi_0$, and thus depends both on the filter clipping function, P_c, and the strength of the coherent Raman vibrations, characterized by $\delta\phi_0$. With the Gaussian probe pulse model we obtain the clipping function $P_c = \exp[-(\tau_p\,\Omega_v/2)^2]\,(\mathrm{erf}\{\tau_p\,(\Omega_c - \Omega_v/2)\} - \mathrm{erf}\{\tau_p\,(\Omega_c + \Omega_v/2)\})/2$. This function displays a nearly linear increase in amplitude with increasing vibrational frequency, Ω_v, and a steep dropoff near $\Omega_v\,\tau_p > 1$, where impulsive vibrational excitation no longer occurs. A

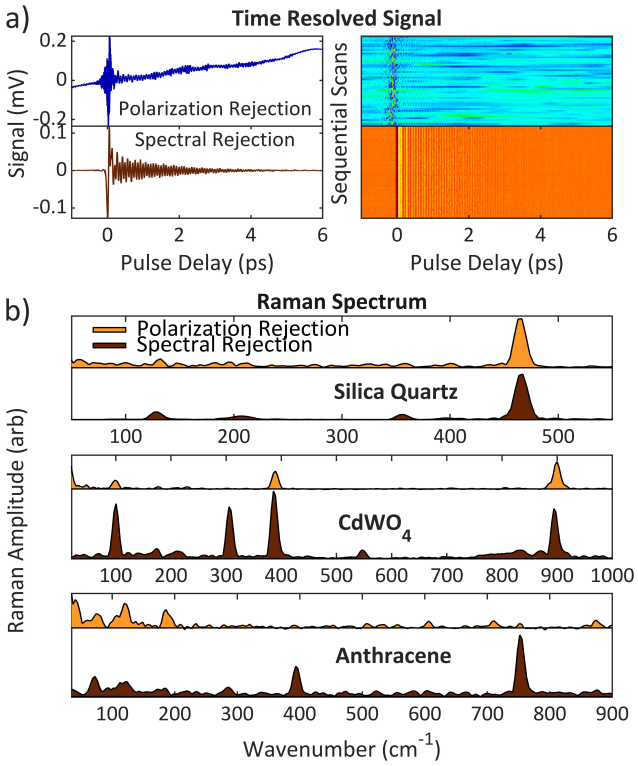

Figure 3.3: Comparison of polarization versus spectral pump rejection for ISRS. a) The time-resolved signal shows a more stable signal using spectral rejection. b) Spectral rejection increases signal-to noise ratio (SNR) and increased sensitivity to Raman vibrational modes.

lower cutoff optical frequency will increase the average transmitted probe power and thus improve the SNR. By contrast, the excitation strength improves with a higher cutoff optical frequency. The peak phase modulation $\delta\phi_0 \propto \bar{p}_{\rm pu}\,\tilde{D}(\Omega_v) = \exp\left[-(\tau_p\,\Omega_v/2)^2\right]$, and thus scales linearly with the average pump pulse power, $\bar{p}_{\rm pu}$, so the signal strength can be traded between the pump and probe pulses. However, the impulsive excitation power spectral density for a compressed Gaussian pulse with a transform limited pulse duration is τ_p is $\tilde{D}(\Omega_v)$. The more the pump pulse spectrum is clipped, the longer the pump pulse duration, which attenuates excitation of the very highest vibrational frequencies. Yet, clipping leaves the excitation strength of lower vibrational frequencies nearly unattenuated. The reduced excitation efficiency at the highest frequencies is a suitable tradeoff for enabling extremely robust Raman imaging.

The expected signal trends are evident in Fig. 3.2 which shows the behavior of the coherent Raman spectroscopy as the clipping frequency is varied. As seen in Fig. 3.2, the signal increases

approximately linearly with vibrational frequency for low-to-mid frequency Raman vibrations (< 500 cm^{-1}) where pump excitation is not limited by bandwidth or pulse duration. Fig. 3.2 b) shows how the signal of specific Raman modes increase and with an increase in filter cutoff frequency (corresponding to more pump bandwidth and a shorter pump pulse) up to a point where the cutoff frequency is high enough that low post-sample filtered probe power becomes the limiting factor for SNR. The clipping of the pump pulse spectrum largely impacts higher vibrational frequencies (see Fig. 3.2 b). The lowest frequency mode (100 cm^{-1}) shows a steep increase in signal level as the probe power is increased when the cutoff frequency is shifted to longer wavelengths. The optimal point occurs for filter edge E, then the signal decreases due to a decrease in the signal power. The 388 cm^{-1} mode shows similar behavior. However, the highest frequency mode at 897 cm^{-1} is extremely sensitive to the clipping frequency. Remarkably, the increase in the signal as the cutoff frequency is lowered (higher wavelength), with a peak at spectral edge E, the high frequency vibrational excitation exhibits a strong nonlinear dependence on excitation strength through $\tilde{D}(\Omega_v)$ as τ_p increases with more severe clipping.

The signal is derived from the differential change in the transmitted probe power through the complementary USSP spectral filter. In the shot noise limit, the noise in the measurement is dominated by the average transmitted probe power through the filter, $\bar{p}_{\mathrm{bkg}} = \bar{p}_{\mathrm{pr}}\,\mathrm{erfc}(\tau_p\,\Omega_c)/2$, so that the transmitted power decreases with increasing probe filter cutoff frequency. Shot-noise limited detection can be accessed with a suitable detector leading to $\mathrm{SNR} = \kappa\sqrt{\Delta t}$. Here, Δt is the detector integration time. The SNR coefficient, $\kappa = P_c\,\delta\phi_0\,\Upsilon_{\mathrm{pr}}$, scales with the strength of the Raman phase modulation $\delta\phi_0$ and with $\Upsilon_{\mathrm{pr}} = \sqrt{\mathcal{R}\,\bar{p}_{\mathrm{pr}}/e}$, where $\mathcal{R}$ is the detector responsivity, e is the elementary charge, and P_c is the spectral transmission coefficient. Evaluation of the SNR parameter indicates that generally SNR improves with a lower Ω_c. While relative intensity noise is problematic for some lasers, such as fibers, RIN can be largely mitigated with balanced detection or lock-in detection.

Rejecting the pump light after the sample using dichroic filtering substantially improves the stability and signal quality of impulsive Raman measurements in samples that have birefringence,

scattering, or defects that contribute to a depolarization of the pump light. Previous detection techniques have used high extinction ratio polarizers to reject pump light, but this technique breaks down when the pump light is no longer uniformly polarized. Fig. 3.3 a) shows the time-resolved signal obtained from a thick piece of silica quartz. Because quartz is birefringent, the pump light is not completely rejected using polarization rejection, leading to pump leak-through that is detected by the LIA and causing instability in the signal and large signal artifacts. Using the dichroic rejection technique developed in this work, it is clear that the signal is significantly more stable with better SNR. The striking improvement in stability can be seen on the right in Fig. 3.3 a). For samples that cause changes to the pump polarization, dichroic pump rejection is far superior to polarization rejection, as demonstrated in the Raman spectra shown in Fig. 3.3 b).

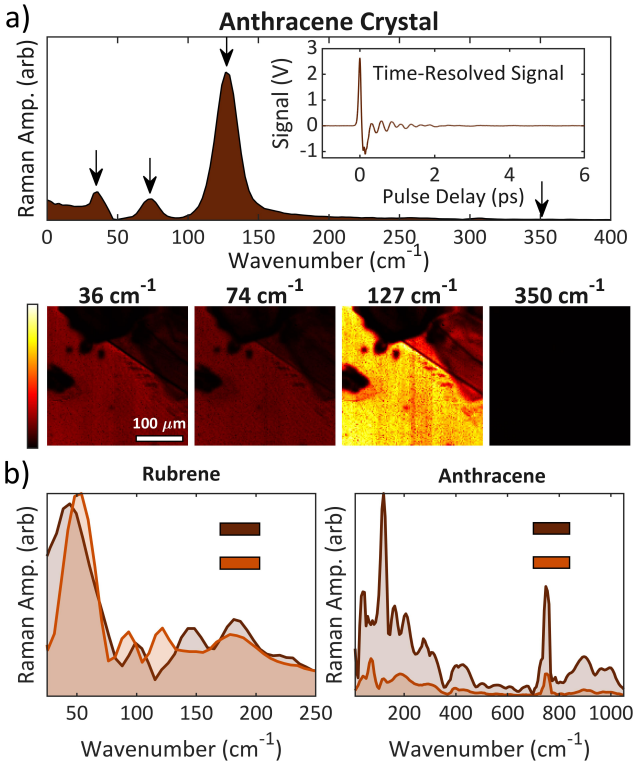

Figure 3.4: Hyperspectral image. a) Example of time-resolved signal and vibrational spectra recorded at each pixel of hyperspectral image. Image contrast generated by isolating specific vibrational modes. b) Spectral rejection enables the use of circular polarization for the pump and probe pulses.

Finally, we note that the use of spectral filter based, instead of polarization based, pump rejection enables detection of polarization-dependant behavior of the Raman spectra as shown in Fig. 3.4 where we see a hyperspectral image of an anthracene crystal in Fig. 3.4 a) and the differences between orthogonal linearly and circularly polarized pump and probe pulses in Fig. 3.4 b).

To conclude, we have demonstrated a new approach for ISRS imaging that greatly simplifies the experimental apparatus. When imaging with ISRS in complex specimens, scattering and depolarization make imaging extremely challenging due to disruption of the beams through scattering and depolarization, which prevents isolation of the probe pulse. By clipping off some of the high-frequency side of the pump spectrum with an edge spectral filter in a standard pump-probe interferometer, we can easily select the high frequency side of the probe pulse spectrum with a complementary spectral edge filter introduced after the sample interaction. We have alleviated concerns that the SNR is strongly reduced in the configuration by developing a theoretical model of the signal transmitted through the probe selection spectral filter. We find that while the very highest vibrational frequencies are mildly attenuated in the signal and SNR, the vast majority of the low frequency vibrational spectrum can be interrogated with nearly the same fidelity as in a conventional ISRS pump probe scenario. However, here we have the advantage that we can maintain high quality imaging even in complex specimens [29] ISRS imaging can be easily adapted to existing SRS by introducing a pump-probe delay scan between the pump and Stokes beams. Such a strategy will probe low frequency modes with vibrational periods longer than the pulse durations. We also anticipate that this new advance will help expand the use of low frequency coherent Raman microscopy and phase-contrast transient absorption [31].

Chapter 4

Phase-Sensitive ISRS

4.1 Introduction

Chemical imaging is a powerful imaging modality in the biological sciences. While fluorescent imaging with exogenous fluorescent probes or transgenically expressed fluorescent proteins forms the workhorse for chemical imaging in biological specimens [32], limitations of fluorescent imaging technologies have driven the development of label-free imaging modalities. [33–39] Of the many label-free imaging modalities, microscopy based on Raman scattering remains particularly appealing due to the narrow Raman vibrational spectroscopic lines that permit reliable identification of molecular species [2].

The vibrational frequency of materials and molecules offers a powerful means to both identify them and probe their dynamics and interactions. [36] Spectral features of the vibrational spectrum can be optically interrogated through either direct dipole-allowed transitions with infrared spectroscopy or through inelastic Raman scattering. Raman scattering is often preferred because infrared spectroscopy suffers from interference from water absorption, broad spectral features, and low spatial resolution resulting from the use of long optical wavelengths. [39] That said, while Raman microscopy with spontaneous scattering is common for many applications, the weak Raman scattering cross-section and incoherent nature of spontaneous Raman scattering severely limit the rate of scattered signal detection—leading to long integration times and poor sensitivity to low concentrations of Raman-active molecules. Raman signals can be enhanced by stimulating the Raman transitions, either by introducing near-field enhancements or by directly stimulating the transitions with a Stokes laser field. Coherent Raman scattering (CRS) [33] overcomes the weak Raman signals by invoking stimulated Raman scattering to drive a much larger response, enabling video-rate

[2]This chapter has been adapted with permission from https://doi.org/10.1021/cbmi.4c00020. Copyright 2024 American Chemical Society.

CRS microscopy. Moreover, an improved detection sensitivity for low concentration and weak Raman scattering modes is obtained with techniques that leverage homodyne interference, producing a linear dependence of the CRS signal on concentration [10, 15, 33].

Raman vibrational frequencies carry extremely valuable information for the study of molecules and material systems. Vibrational frequencies, Ω_v, scale as a harmonic oscillator, $\Omega_v^2 = k/m$. Thus, strong binding, associated with a large value of the effective force constant k, and low (reduced) mass, m, of the vibrational mode correspond to high vibrational frequencies. The highest frequency modes are approximately localized and correspond to hydrogen bonds due to the low hydrogen mass and are used in investigations of water and lipids. The mid-band frequencies, $\Omega_v \sim 400 - 1200$ cm^{-1}, are extremely powerful for the identification of particular molecules [33] and even for bacterial classification. [40] Recent attention has focused on the largely neglected low-frequency vibrational modes. [10] These modes are generally associated with large reduced mass and correspond to vibrational motion that occurs over an extended region. Such relevant motions include virus capsid vibrations, [5] deformations of proteins, [6] and mechanical properties of solids, particularly for soft [7] and two-dimensional materials. [8, 9]

However, implementation of Raman scattering at low vibrational frequencies remains a persistent challenge [10] because inelastic scattering at small offsets is difficult to measure, requiring low noise, narrow linewidth lasers, multiple stages of monochromators, and extremely steep spectral edge filters. The result is that imaging is extremely challenging. In this Letter, we introduce a simple and robust technique that is suitable for imaging in complex specimens. Our approach makes use of impulsive stimulated Raman scattering (ISRS) to probe low-frequency vibrational modes with time-domain spectroscopy. [10] In ISRS, a short pump pulse is used to drive the excitation of vibrational coherences for vibrational frequencies lower than $\sim 1/\tau_p$, where τ_p is the pump pulse duration. [16] Because the Raman interaction involves a change in molecular polarizability with vibrational displacement, excitation of vibrational coherences produces an effective time-varying perturbation to the linear optical susceptibility denoted by $\delta\chi_{\text{eff}}(t)$. [10] The Raman spectrum is obtained by recording signals with a probe pulse that follows behind the pump pulse by a delay

of τ. The recorded signals are derived from the temporal phase, $\phi_v(t)$, accumulated by the probe pulse as it propagates through the excited vibrational coherence. This recovered spectrum is continuous and spans a range with a maximum frequency on the order of $1/\tau_p$ down to a minimum frequency $1/\Delta\tau$ bounded by the range of pump-probe delay $\Delta\tau$.

The readout method of the Raman spectrum in ISRS impacts the sensitivity of spectral detection. [10] The most common technique is to make use of a spectral shift for detection, where spectral scattering from the time-dependent phase modulation applied to the probe pulse by the transient effective linear optical susceptibility leads to changes in power transmitted through a spectral filter. [24, 41–43] Improved detection sensitivity can be achieved by turning the probe pulse spectral shift into a change in arrival time at a detector by applying additional spectral dispersion. [23] Methods that detect the signal based on a spectral shift reduce the amplitude of the low-frequency vibrational modes and impart a spectral filter on the relative amplitudes of the Raman spectrum. To emphasize the low-frequency vibrational modes and eliminate the spectral distortions imparted by frequency shift detection, $\delta\chi_{\text{eff}}(\tau)$ should be probed directly. [10]

Low frequency vibrations can be readily detected with ISRS methods where the signal detection is directly proportional to the time-varying change in the optical susceptibility induced by the forced Raman response. Several methods have been explored for the direct measurement of $\delta\chi_{\text{eff}}(t)$ to obtain an undistorted Raman spectrum, which we call phase-sensitive ISRS (ϕ-ISRS). ϕ-ISRS spectroscopy was originally implemented in a transient grating geometry, [16] which allows for background-free measurements but relies on direct measurement of the diffracted beam power, leading to limited detection sensitivity. In the transient grating experiment, the amplitude of the diffracted probe field is proportional to $\delta\chi_{\text{eff}}(\tau)$, i.e., the susceptibility perturbation at the pump-probe delay τ. However, because the total scattered power is recorded, the Raman spectrum is distorted. The direct amplitude of $\delta\chi_{\text{eff}}(\tau)$ can be obtained with Kerr lensing [21] and interferometric measurements. [18–20, 44, 45] A comparison of the Raman spectral amplitudes has been demonstrated in a Sagnac interferometer configuration and verified the access to low-frequency vibrational spectral information when $\delta\chi_{\text{eff}}(t)$ is directly obtained, with a an enhancement in the

signal strength for low-frequency measurements compared to a frequency shift [44]; this result has recently been validated in further experiments. [45] The Sagnac interferometer configuration is intrinsically stable, but has limited application for spectroscopic or imaging measurements. A stable common path interferometer configuration is possible with a collinear time-delayed probe and reference pulse configuration, [46, 47] which has been demonstrated with spectral interferometry [18–20] and Fourier transform interferometry. [48]

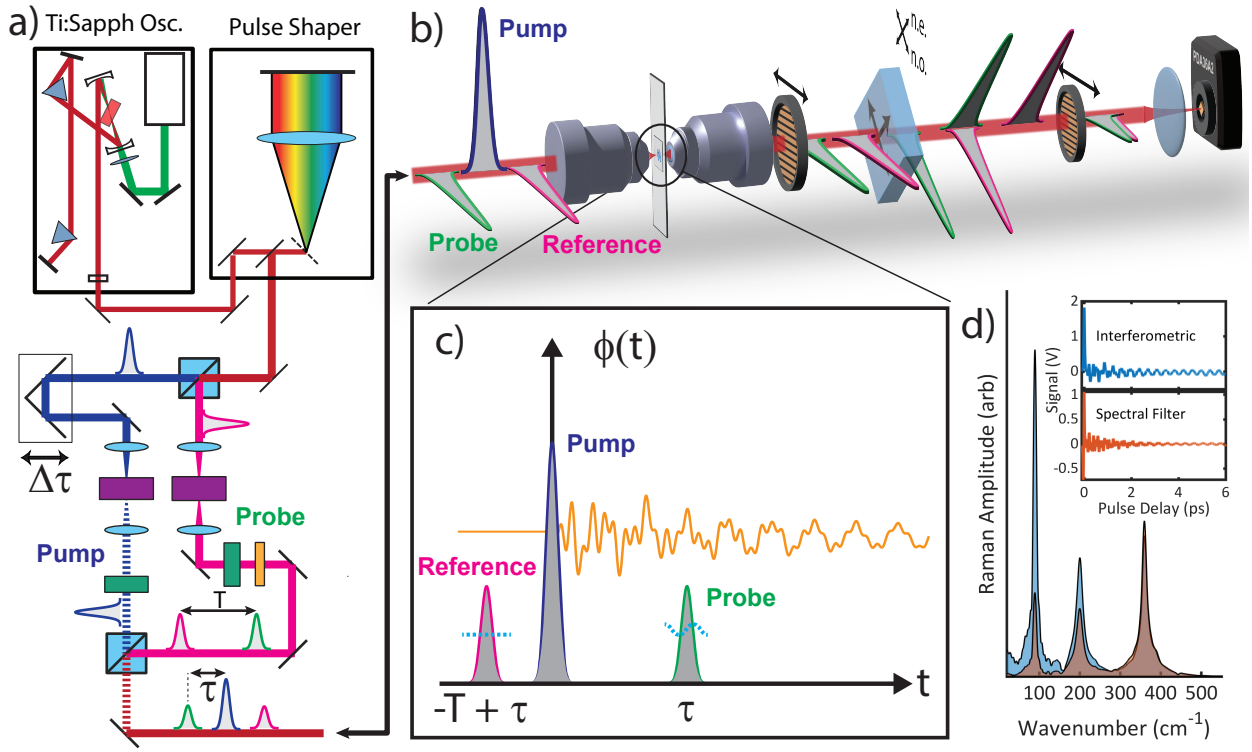

Figure 4.1: Common path interferometric ϕ-ISRS concept figure. a) Experimental setup for ϕ-ISRS. The acousto-optic modulators, calcite crystals, and linear polarizer are represented by the purple, green, and orange elements, respectively. b) Conceptual figure that shows the interaction of the pump, probe, and reference pulses with the sample, as well as the isolation of the probe-reference pair and re-timing to produce pulse interference. The interference produces signal current changes in a photodiode that are proportional to the Raman-induced transient phase, $\phi(\tau)$, at the arrival time, τ, of the probe pulse. c) The relative arrival time of the pump, probe, and reference pulses. d) Example Raman spectra measured in BGO for ϕ-ISRS and spectral shift detection [1]. The improved low-frequency Raman detection with ϕ-ISRS is evident.

4.2 Concept

Unfortunately, the existing ϕ-ISRS methods are restricted to non-depolarizing and non-scattering samples such as liquid-phase spectroscopy or transparent crystals. In this Letter, we introduce a simple collinear interferometric approach to ϕ-ISRS that is extremely stable and thus performs robustly in the presence of strong scattering and depolarization effects, such as in cell culture and tissues.

A conceptual schematic of the experimental system is shown in Fig. 4.1. A modelocked ultrafast laser produces pulses that are passed through a spatial light modulator pulse shaper for second and third order dispersion control. The laser beam power is split into pump and probe pulses in an orthogonally polarized Mach-Zenhder interferometer. The pump pulse intensity is modulated by an acousto-optic modulator to allow for lock-in amplifier detection of the Raman signal. A computer-controlled resonant delay scanner in the pump arm enables rapid scanning of the relative pump-probe delay τ. The probe pulse arm is modified from a standard pump-probe experimental arrangement [24, 25, 43] in order to generate a probe-reference pulse pair with a birefringent optical crystal. [47]

Birefringent crystals are used both as a pulse pair generator [24, 47, 49] and a pulse retimer to create a common path collinearly propagating probe-reference pulse pair with an extremely stable relative phase and a temporal separation of T, as shown in Fig. 4.1b. The probe-reference pair is generated by sending a linearly polarized probe pulse through a birefringent crystal plate rotated so that the eigen-polarization axes are at 45 degrees with respect to the input linear polarization of the probe pulse. Depending on the cut of the crystal and the orientation of the optic axis, the relative delay time, T, can be adjusted by rotating the birefringent crystal or by adjusting the crystal thickness. The pulses are separated by a few picoseconds and share a common propagation path.

To combine the probe-reference pulse pair with the pump pulse, the probe-reference pair is projected onto the same linear polarization axis in the polarizing beam splitter where the pulse pair is combined with the orthogonally polarized pump pulse. The pulses are focused into the sample with a high numerical aperture aspheric lens and recollimated with an identical aspheric

lens after passing through the specimen. The pump pulse is removed from the collimated beams with a polarizer to isolate the probe-reference pulse pair.

The coherent ISRS signal is contained in a phase perturbation, $\phi_v(t)$, induced by the pump pulse. The reference pulse precedes the pump pulse, accumulating a phase as it propagates through the optical system. This phase accumulated by the reference pulse comes from the sample at equilibrium because the vibrational coherences decay to equilibrium (over several picoseconds), long before the next pulse in the oscillator pulse train arrives ($\sim$ 10 ns). By contrast, the probe pulse arrives at a delay, τ, after the pump pulse and accumulates a phase identical to the reference pulse in addition to a phase perturbation induced by Raman excitation by the pump pulse. By placing the pump pulse in between the reference and probe pulses, the relative phase between the probe and reference pulses is the accumulated vibrational phase perturbation acquired by the probe pulse. After interacting with the sample, the probe-reference pair is isolated from the pump pulse—for example with a polarizer—then the probe-reference pulse pair is re-timed. In this way, the relative phase is converted to an amplitude modulation through interference between the probe and reference pulse so that the Raman signal is detected with a simple photodiode.

This pulse pair is re-timed using a second birefringent crystal that is oriented at –45 degrees to undo the probe-reference delay so that the probe and reference pulses overlap in time, i.e., setting $T = 0$. Because the probe-reference pulse pair propagates along the same direction and are only separated by a few picoseconds, $T \sim 6$ ps, the relative phase between these two pulses is exceptionally stable—allowing very stable phase measurements of the transient phase introduced by the pump pulse. The probe and reference pulses are in the same spatial mode and polarization state; only half of the power of the probe and reference pulses is overlapped in time and will interfere (see Fig. 4.1 b)). In addition, the two pulses travel through exactly the same optical path, and thus share the same spatial mode, making interference between the beams robust to perturbations acquired with propagation through optical scattering environments. To demonstrate the robustness of our approach, we introduce controlled scattering to a sample by adding layers

of parafilm on the sample between the objective and the sample of interest. For a more detailed description of the experimental setup, please refer to the supplementary information.

The interferometric signal for ISRS spectroscopy emerges from the fact that the pump pulse excites a non-equilibrium time-varying change in effective linear optical susceptibility, $\delta\chi_{\text{eff}}(t)$, imparting a transient phase modulation on a time-delayed probe pulse. The reference pulse can be arranged to arrive before the pump pulse so that the only phase that it accumulates is from the optical system and the specimen at thermal equilibrium. The pump pulse-induced phase perturbation, $\phi_v(t) = k_{\text{pr}}\,\ell\,\delta\chi_{\text{eff}}(t)/2n_0$, is then the only phase shift acquired between the probe and reference pulses. Here, ℓ is the focal interaction length, n_0 is the sample refractive index at thermal equilibrium, and $k_{\text{pr}} = 2\,\pi/\lambda$ is the free-space wavenumber for a pulse with center wavelength λ. The fact that the probe and reference pulses are common path means that all accumulated scattering, aberrations, and depolarizations are identical for both beams. This produces an extremely stable signal that prevents many forms of technical noise.

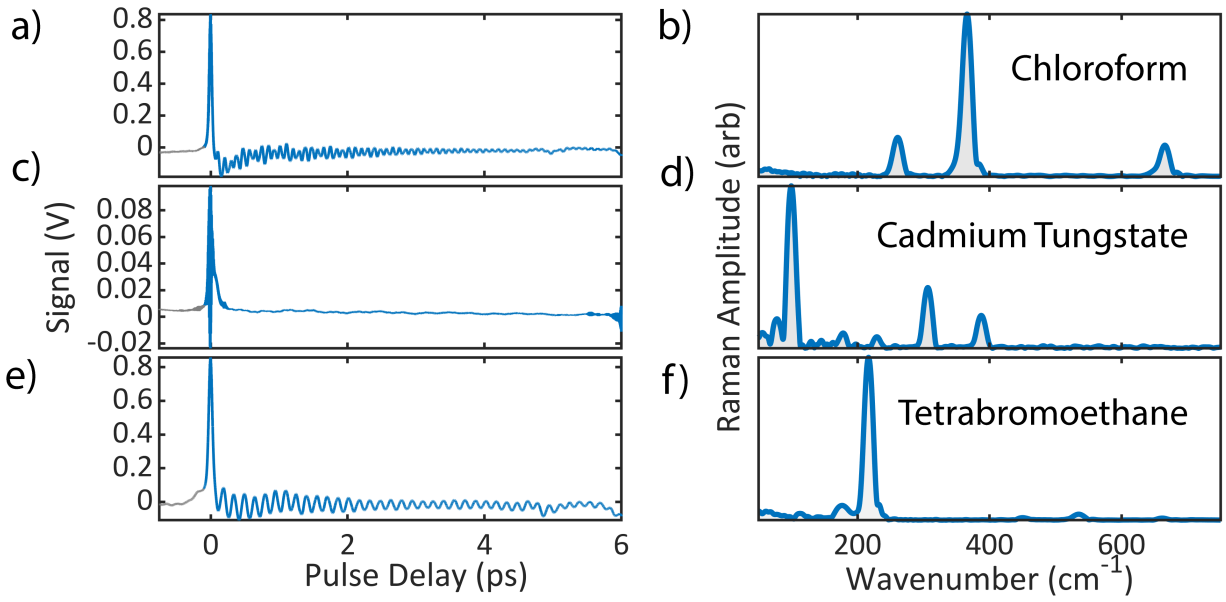

Figure 4.2: ϕ-ISRS data from multiple samples with low frequency Raman vibrations. a) The time-resolved ϕ-ISRS signal for Chloroform. b) The recovered Raman spectrum of Chloroform. c) and d) show the time-resolved signal and Raman spectrum for Cadmium Tungstate. e) and f) show the time-resolved signal and Raman spectrum for tetrabromoethane. Liquid and depolarizing crystal samples illustrate the effectiveness of ϕ-ISRS for robust low-frequency Raman spectroscopy.

The phase modulation due to the excited vibrational coherence can be expressed as a linear superposition of the phase modulation from each excited vibrational mode as $\delta\phi^v(\tau) = \sum_v \delta\phi_0^v \; h_v(\tau)$, and depends on the arrival time τ of the probe pulse after the excitation induced by the pump and is summed over the contribution of each vibrational mode, denoted with a superscript v. Each vibrational mode is excited through an impulsive forced Raman response that is driven by the pump pulse, leading to a damped causal oscillation [10, 15], $h_v(t) = \Theta(t)\,\exp(-\Gamma_v\; t/2)\,\sin(\Omega_v t)$. Here $\Theta(t)$ is the Heavyside step function that ensures causality and Γ_v is the damping rate of the mode at the vibrational frequency Ω_v. The induced vibrational phase perturbation $\delta\phi_0^v = g_f\,\mathrm{Im}[\chi^{(3)}_{\mathrm{V}R}(\Omega_v)]\,\Gamma_v\,\tilde{D}(\Omega_v)\,\bar{p}_{\mathrm{pu}}$ scales linearly with the average power of the pump pulse, $\bar{p}_{\mathrm{pu}}$, and the molecular concentration, N, which becomes clear when we note that $\mathrm{Im}[\chi^{(3)}_{\mathrm{V}R}(\Omega_v)] = N\,(\partial\alpha/\partial Q)_0^2/6\epsilon_0\,\Gamma_v\,\Omega_v$. The amplitude of the Raman-induced phase modulation is also proportional to the power spectral density (PSD) of the pulse intensity profile at the vibrational frequency Ω_v [1,50], $\tilde{D}(\Omega) = \mathcal{F}\{I(t)\}/I_0\,\tau_0$. Here I_0 is the peak pulse intensity and $\tau_0 = \int I(t)/I_0\,dt$ is a measure of the pulse duration. In the limit of an impulsive pump pulse, $I(t) = I_0\,\delta(t)$, then the excitation PSD, $\tilde{D}(\Omega) \to 1$, so that the forced Raman response is the impulse for vibrational excitation. Here, we assume that the temporal duration, τ_p, and the temporal intensity, $I(t)$, of the pump, probe, and reference pulses are all identical. The coherent Raman excitation that drives the vibrational phase perturbation also depends on the focusing conditions, which are encapsulated in the focusing parameter $g_f = 12\,\pi\,\ell/(n^2\,\epsilon_0\,c\,\nu_R\,\mathcal{A}_f\,\lambda)$, where $\mathcal{A}_f$ is the focal beam cross sectional area, ν_R is the laser repetition rate frequency, and λ is probe pulse center wavelength.

4.3 Results

In our experiment, the probe-reference pulse pair, with a total average power of $\bar{p}_{\mathrm{pr}}$, is isolated from the pump pulse using polarizer to block the pump pulse. Then, half of the probe and reference pulse average power is adjusted to interfere in a compact, collinear interferometer using an angle-tuned birefringent crystal. The relative phase of probe and reference pulses are adjusted to be

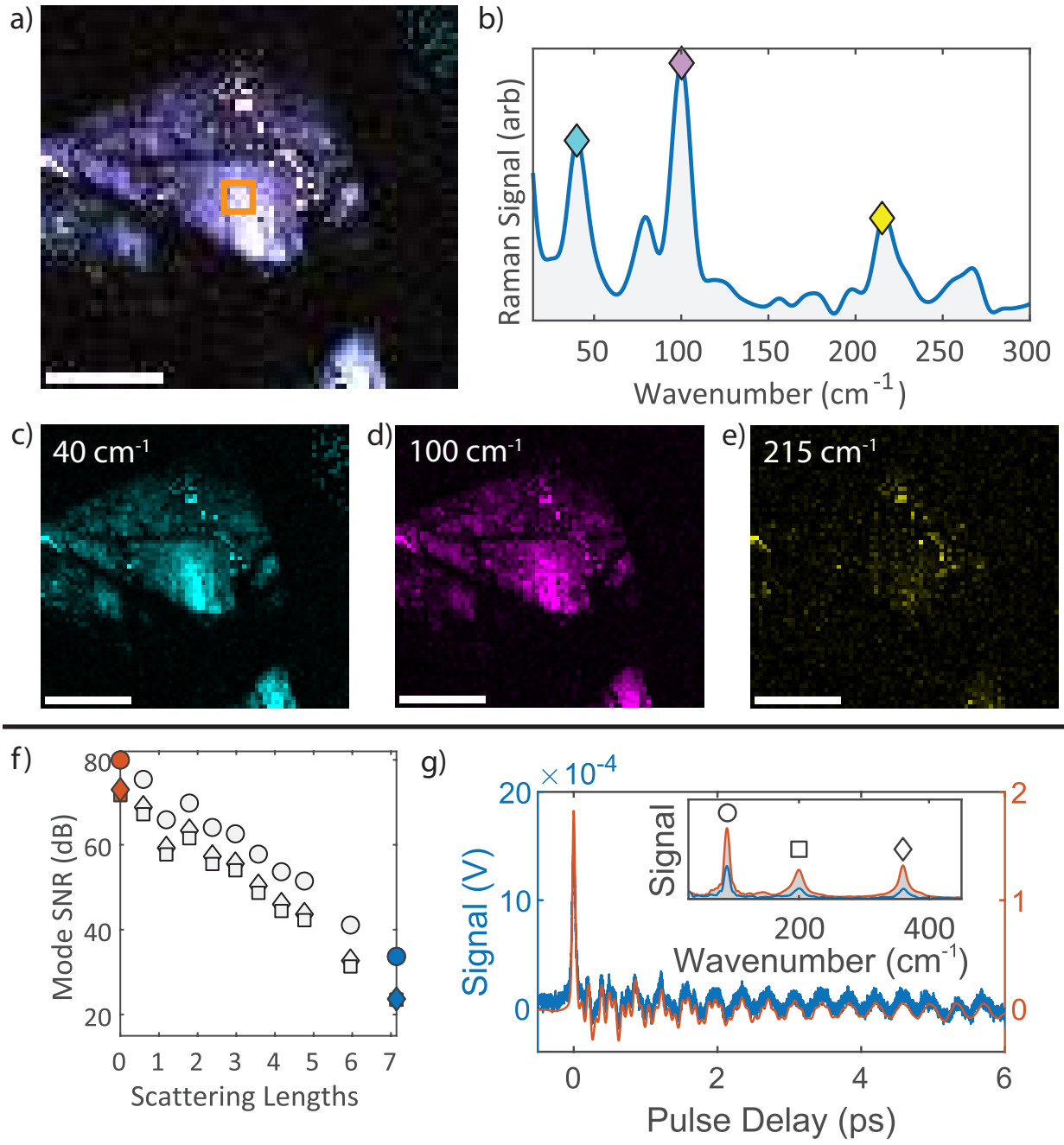

Figure 4.3: a) A composite image of the three low-frequency Raman-active optical phonon modes in an anthracene crystal. b) The Raman spectrum of the crystal at a single pixel centered in the orange square shown in a). c–e) Individual images of the three Raman modes indicated in b). f) The signal-to-noise ratio (SNR) of the three Raman vibrational modes of a BGO crystal with scattering layers added between the sample and the excitation objective. A high SNR is indicated for > 7 scattering lengths. g) A comparison of the Raman spectrum of BGO for zero and 12 scattering layers shows high quality spectra extracted even under conditions of strong optical scattering. Image acquisition parameters and SNR calculation details can be found in the Supporting Information. All scale bars are 50μm

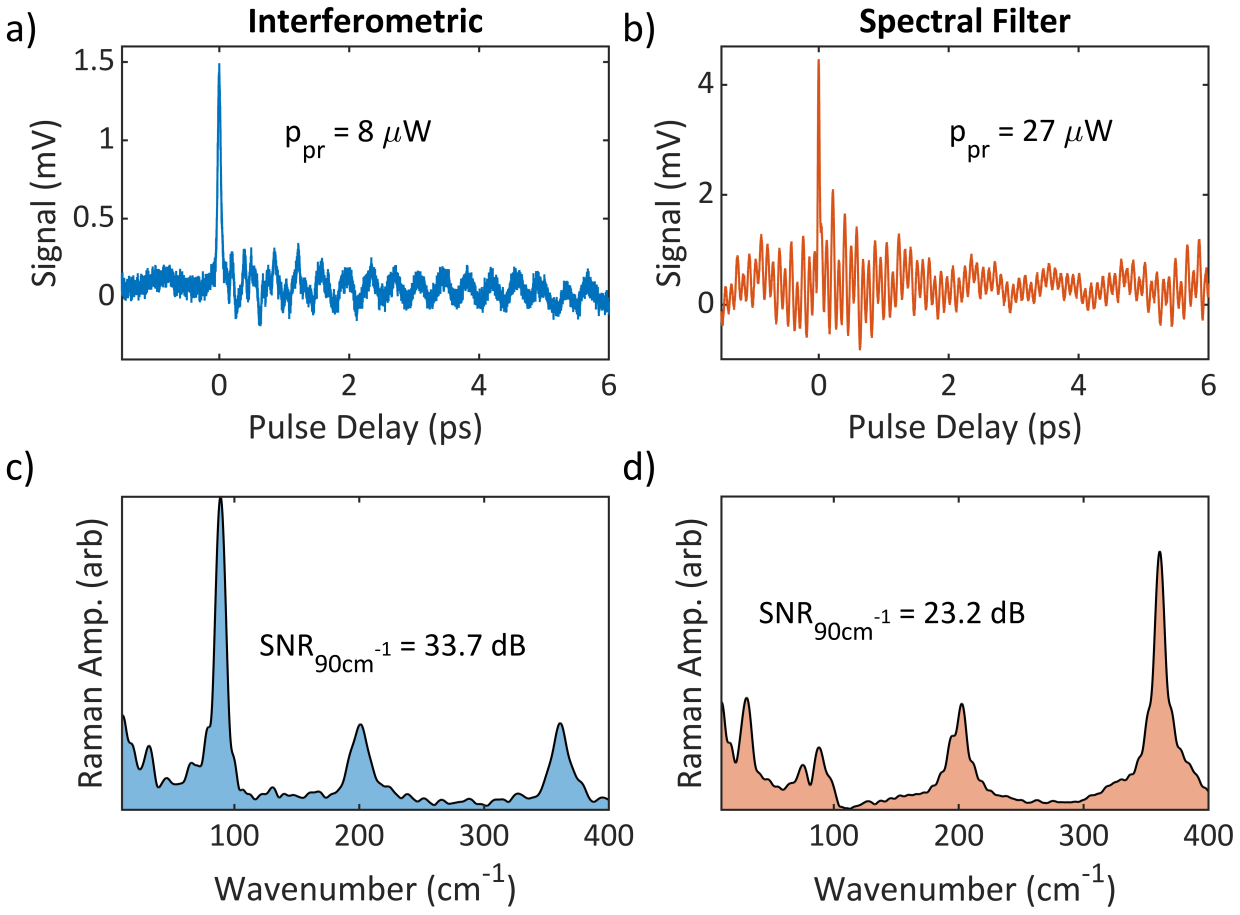

Figure 4.4: Comparison between ϕ-ISRS and spectral filter detection ISRS through 12 scattering layers. a) The time-resolved signal for ϕ-ISRS with the probe power incident on the photodiode indicated. b) The time-resolved signal for spectral filter detection ISRS with the probe power incident on the photodiode indicated. The time-resolved signal shows evidence of scattering and depolarization of the pump beam causing signal contamination around $\tau = 0$. The Raman spectra are shown in c) and d) with the SNR of the 90cm^{-1} mode. Details of the SNR calculation can be found the in the Supporting Information. The ϕ-ISRS shows a significantly higher SNR with a lower incident probe power. The pump contamination present in b) and d) contributes to distortion in the low frequency spectrum in addition to the lower SNR.

in quadrature so that the total power of the interfering pulses is $\bar{p}_{\rm int} = \bar{p}_{\rm pr}\left\{1+\sin[\delta\phi^v(\tau)]\right\}/2$, leading to a signal power incident on the detector of $\bar{p}_{\rm sig}(\tau) = \delta\phi^v(\tau)\ \bar{p}_{\rm pr}/2$, with a background power equal to the total average probe pulse train power $\bar{p}_{\rm bkg} = \bar{p}_{\rm pr}$. In the shot noise limit, the signal-to-noise ratio (SNR) for a detection integration time of Δt reads ${\rm SNR} = (\delta\phi^v/2)\ \Upsilon\ \sqrt{\Delta t}$, where $\Upsilon = \sqrt{\mathcal{R}\,\bar{p}_{\rm pr}/e}$, $\mathcal{R}$ is the detector responsivity, and e is the elementary charge. Provided that the total probe power exceeds approximately 2 mW, the shot noise limit is valid for lock-in detection that is able to largely avoid the laser intensity fluctuation noise. Because both the signal power and SNR depend linearly on $\delta\phi^v$, this collinear interferometric method is sensitive to low Raman vibrational frequencies, and is limited where the impulsive Raman excitation strength, $\tilde{D}(\Omega_v)$, becomes too low, which occurs when the vibrational period is on the order or larger than the pump pulse duration.

The ϕ-ISRS spectrum of the low-frequency optical phonon Raman spectrum in BGO is shown in Fig. 4.3d in comparison to a spectral shift measurement. The increased amplitude at low vibrational frequencies is apparent in the interferometric measurement. Because the pump-probe delay τ can be controlled independently of the separation between the probe and reference pulses, which is a fixed delay T, there are three zones for the ϕ-ISRS experimental system, each of which is illustrated in Fig. S2. We define the time-frame so that $t = 0$ occurs at the center of the pump pulse The first pulse to arrive is denoted the reference pulse that is incident at at a time $t = \tau - T$ and the probe pulse arrives at a time τ. Zone I occurs when $\tau < 0$, so that both the probe and reference pulses arrive before the pump pulse. In this region, there is no pump-induced transient phase acquired between the probe and reference pulses, so we have a null signal. Zone II is where we pull the Raman spectra; this temporal signal provides a pure Raman spectrum because only the probe pulse accumulated the Raman-induced phase shift. In Zone III, the spectrum is distorted because the interference signal is determined by the phase shift acquired by the probe and reference pulses, i.e., $\phi(\tau) - \phi(T-\tau)$.

Inteferometric ϕ-ISRS spectra from several samples displaying low-frequency Raman modes are shown in Fig. 4.2. While the chloroform and tetrabromoethane are liquid samples and do not

suffer depolarization, the cadmium tungstate is a birefringent crystal and induces a depolarization between the pump pulse and the probe-reference pulse pair. The time-domain traces are shown on the left column, whereas the Raman spectra shown in the right column is computed from the power spectral density of the time-domain trace after isolation of the signal that contains only the Raman transients away from the cross phase modulation feature near time zero. [18] The observed Raman spectral modes match known Raman spectral lines of these three samples.

Hyperspectral Raman images of anthracene crystals for three low-frequency Raman-active optical phonon modes are shown in Fig. 4.3. The Raman spectrum of the optical phonon modes is shown in Fig. 4.3b. Images for the three phonon modes marked in the spectrum are shown in Fig. 4.3c-e, whereas a composite image is displayed in Fig. 4.3a. The complex morphology of the crystals produces scattering that distorts the beams and degrades the Raman signal. However, we see that high-quality images are obtained with the common-path interferometric readout because the probe and reference pulses maintain identical spatial and polarization modes.

To quantitatively evaluate the effect of optical scattering on ϕ-ISRS with common-path interferometric detection, we captured Raman spectra as we added layers of optical scattering material. For each measurement, the Raman signal and the noise were estimated using the power spectral density (PSD) of the time-resolved signal. The "signal" (S) for a known Raman mode is calculated from the root mean square (RMS) of the spectral mode whose width is determined by where the value drops to 95% of the mode peak. The "noise" (N) is calculated from the RMS of the PSD of a frequency region well-removed from the Raman spectrum at wavenumbers above those excited by the pump pulse. From these values, we compute $\mathrm{SNR} = 10\log_{10}(\mathrm{S/N})$. To introduce optical scattering, layers of parafilm were added on the front of the BGO sample, thus introducing scattering before Raman excitation by the pump pulse and spectral scattering of the probe pulse. Results are shown in Fig. 4.3f, displaying the SNR as a function of the number of scattering layers added between the sample and the excitation objective. The data show two regions of SNR decay as a function of the number of scattering lengths, indicated by dashed lines in the figure. The Raman spectra for the highest and lowest SNR data are shown in Fig. 4.3g.

4.4 Discussion

Imaging of low-frequency vibrational modes with coherent Raman remains a challenging prospect. Here we introduce a new imaging strategy for a wide bandwidth of Raman vibrational frequencies, spanning from very low frequencies (< 300 cm^{-1}) to frequencies well within the fingerprint region > 1000 cm^{-1}. Our new strategy relies on a pump-probe geometry using ϕ-ISRS excitation of a vibrational coherence by a short pump pulse that is electronically non-resonant with the specimen. Such short pulse excitation is capable of exciting vibrational frequencies with periods that are longer than the pump pulse duration. [1] As a result, short laser pulses with carefully maintained dispersion compensation are critical for ISRS excitation. After excitation of the vibrational coherence, the readout of the signal with a probe pulse plays a crucial role in the vibrational frequencies that are observed. The conventional strategy is to use a spectral edge filter to convert the spectral scattering driven by the transient phase modulation acquired by the probe pulse when propagating through the vibrational coherence into a change in probe pulse power transmitted through the spectral filter. [24, 29] Unfortunately, this simple strategy renders ISRS largely insensitive to low-frequency vibrations. [10] By reading out the phase directly through interferometry, we directly detect the time domain-forced Raman response, providing sensitive detection of the low-frequency Raman vibrational modes.

Aside from the high sensitivity to low-frequency vibrational modes (e.g., terahertz Raman), we have demonstrated that our common-mode strategy for the detection of the transient Raman phase modulation produces high SNR data even in the face of optical scattering. This resilience of our signal detection to optical scattering follows from two properties that we acquire by generating the probe-reference pair in a suitably oriented birefringent crystal. The first property is that the probe and reference pulses are common path. Because of this common path propagation, any scattering that is encountered is common to both the probe and reference pulse beams. As a result, the beams are guaranteed to still interfere. Indeed, even depolarization is not a problem, as the spatial modes of the probe and reference beams are identical—ensuring stable interference even after becoming severely distorted, as they are distorted identically.

Of course, common path perturbations are only relevant if the relative phase, scattering, and depolarization are stable for the duration of the integration time over which the interference is acquired. The relative stability of the probe and reference pulses is guaranteed by the fact that there is very little perturbation of the refractive index of the specimen that can occur on the timescale of a few picoseconds other than the non-equilibrium vibrational coherence dynamics that are excited with the pump pulse.

The combination of the temporal and common-mode interferometric stability ensures extremely stable and high-sensitivity detection of the vibration-induced phase shift. The robustness of our approach is demonstrated by introducing controlled scattering to a sample by adding layers of parafilm on the sample between the objective and the sample of interest. The scattering introduced by the parafilm layers was characterized by measuring power transmission through a blank sample as more layers of parafilm were added. The power transmitted through the scattering layers decreases exponentially with the number of scattering layers. The scattering length, defined as when the optical power decreases by $1/e$, was found to be $\ell_s = 1.68$ parafilm layers. The scattering length was determined in a separate experiment where parafilm layers were sequentially added to a glass slide and the transmitted power through the collection objective was directly measured with a power meter. Figure 4.3f shows the SNR for the three main vibrational modes of BGO as a function of scattering length of parafilm added to the sample. Panel (g) of Figure 4.3 shows the time-resolved signal and the Raman spectrum (inset) of BGO with no scattering layers (orange) and the signal with the maximum number of scattering layers used (blue), which is 12 layers of parafilm, or 7.14 scattering lengths. This result shows the robustness of the interferometric Raman technique, with the SNR of the BGO modes remaining high after over 7 scattering lengths. The incident optical powers incident on the sample were $p_{pu} = 37.8$ mW and $p_{pr} = 38.95$ mW for the pump and probe, respectively. After passing through the sample, objectives, retiming crystal and analyzing polarizer, the probe power incident on the detection photodiode was $p_{pr} = 8.6$ mW with no scattering present. The probe power incident on the detection photodiode was measured to be $p_{pr} = 8$ μW with 12 parafilm layers (7.14 scattering lengths).

Because we have constructed this system based on orthogonally polarized pump and probe-reference pulses, we are limited to vibrational modes with a more symmetric character, and we may have reduced sensitivity to asymmetric modes. The spectral resolution of this strategy is limited to $\sim 1/T$ for methods that rely on power spectral estimation, e.g. the FFT or multitaper computation. However, the use of model-based estimation, e.g. LP-SVD, can circumvent this spectral resolution limitation. The lower bound of the vibrational frequency is limited by the scan range of the probe-reference pair. For Zome II, the lower bound is $\tilde{\nu} = (c\,T)^{-1} \sim 7$ cm^{-1}, but this can be extended arbitrarily with synthetic aperture scanning [19], where the probe and reference pulse pair both follow the pump pulse, at the cost of the loss of frequencies with vibrational periods that are an integer multiple of T. Application of LD-SVD methods are expected to further improve this lower bound.

4.5 Conclusions

We have developed a new and versatile method for low-frequency coherent Raman imaging. Balanced detection could eliminate the need for the acousto-optic modulator for beam intensity modulation, which will drastically reduce the spectral dispersion burden of the system. Such an approach would allow for easier use of high numerical aperture objective lenses that also carry a high dispersion. Right now, the relatively low numerical aperture and off-axis aberrations of the aspheres have limited our ability to image in complex samples, and the long working distance makes thin samples such as two-dimensional materials challenging to image. Future advances will explore additional strategies to simplify the imaging approach.

Supporting Information: details on the dispersion compensation required for driving ϕ-ISRS, additional experimental concept and setup diagrams to provide further understanding of ϕ-ISRS, details of the rapid delay line used for pump-probe scanning during image acquisition.

4.6 ϕ-ISRS Experimental System

The experimental layout for the system is provided in Fig. 4.5. The key to a robust ϕ-ISRS imaging is the production of common-path probe and reference pulses. [17, 46, 47] This pulse pair is generated in the experimental system that builds on a pump-probe experimental system using a Mach-Zehnder interferometer. [43] In addition, because we are using an ISRS interaction with broad-bandwidth ultrafast pulses, careful dispersion management is required. Pulses are generated in a Ti:sapphire laser (KM Labs Halcyon, $\sim$ 600 mW average power, $\sim$ 18 fs pulses, 94 MHz repetition rate). The output laser beam is collimated and then directed into a pulse shaper constructed from a folded Martinez stretcher with a flat mirror and a transmission spatial light modulator (SLM) placed at the focal plane of the lens (the Martinez Fourier plane). [51, 52] Details of the pulse compression protocol can be found in the supplemental information in our recent split-spectrum ISRS paper. [43]

After passing through the pulse shaper, the beam is split into pump and probe (reference) pulses with a low-dispersion polarizing beam splitter (ATFilms, PBS1005-GVD). The relative power in the two arms is controlled by a half-wave plate placed before the beam splitter. An acousto-optic modulator (AOM) crystal resides in each arm of the pump-probe interferometer. In the pump arm, the pump pulse is passed through an AOM that imparts a sinusoidal intensity modulation onto the pump pulse train for lock-in detection. The pump pulses are modulated at several MHZ to allow for detection of the signal through lock-in detection at an offset frequency where intensity noise fluctuations from the laser are low. The AOM in probe arm is left passive and is required to balance the spectral dispersion in the two interferometer arms. The pump and probe pulses are recombined with a second low-dispersion polarizing beam splitter. A reflective optical delay line in the pump pulse arm is used to control the relative arrival time, τ, of the pump and probe pulses. The pump-probe delay is rapidly scanned with a resonant scanner delay line (Peregrine, Mesa Photonics) that is capable of performing 20 ps delay scans at 60 Hz. The full delay is scanned with a triangle pattern that produces full ϕ-ISRS signal traces at a rate of 120 Hz. A full Raman spectrum is obtained in $\sim$8.3 ms. The Raman spectrum is obtained from the temporal

trace by either estimating the spectrum of the temporal trace with a fast Fourier transform through linear prediction singular value decomposition. [19, 49, 53] Defining a signal to noise ratio (SNR) metric that accurately captures the details of the data in the frequency domain is difficult. Because our interest is ultimately in the ability to resolve Raman vibrational modes, the SNR metric uses the root mean square value of the power spectral density for each BGO vibrational mode as the "signal". For the noise metric, a high frequency region $> 600\,\mathrm{cm}^{-1}$, that is known to be devoid of any spectral information, was selected and the root mean square (RMS) noise is computed for a suitable spectral interval to estimate the noise level. The SNR values quoted in the paper are from the ratio of the RMS value of a given Raman vibrational mode to the RMS value of the well-separate high-frequency spectral region.

To enable ϕ-ISRS detection, the probe pulses are temporally split into a pair of orthogonally-polarized probe and reference pulses. The probe and reference pulses are created by sending the linearly polarized probe pulse into the birefringent crystal (10mm thick calcite, Newlight Photonics) with the crystal rotated so that the axis of the linear polarization of the probe pulse is at 45 degrees with respect to the eigen-polarization axes of the ordinary and extraordinary polarization directions. [17, 19, 20, 24, 46–48, 52] The group velocity of the pulses that are projected onto the ordinary and extraordinary polarization directions differ, leading time delay accumulated through propagation through the uniaxial birefringent crystal. The rotation angle of the optical axis of the crystal can be adjusted to fine-tune the relative delay and the relative phase between the probe and reference pulses. Then the probe-reference pair is combined with the pump pulse in the polarizing beam splitter, the pulses are projected on the same linear polarization with equal amplitude. The pump pulse is orthogonally polarized to the probe-reference pair. An identical birefringent crystal is placed in pump arm to mach the dispersion between the arms.

The combined and orthogonally polarized pump and probe-reference pulses are focused into the with a low-dispersion aspheric lens (40x/0.6 NA, Newport). Typical pump/probe powers at the focus are $p_{pu} = 38\,\mathrm{mW}$, $p_{pr} = 19.5\,\mathrm{mW}$, and $p_{ref} = 19.5\,\mathrm{mW}$. After passing through the sample, the beams are collimated with a matching asphere. Once the probe-reference pulse

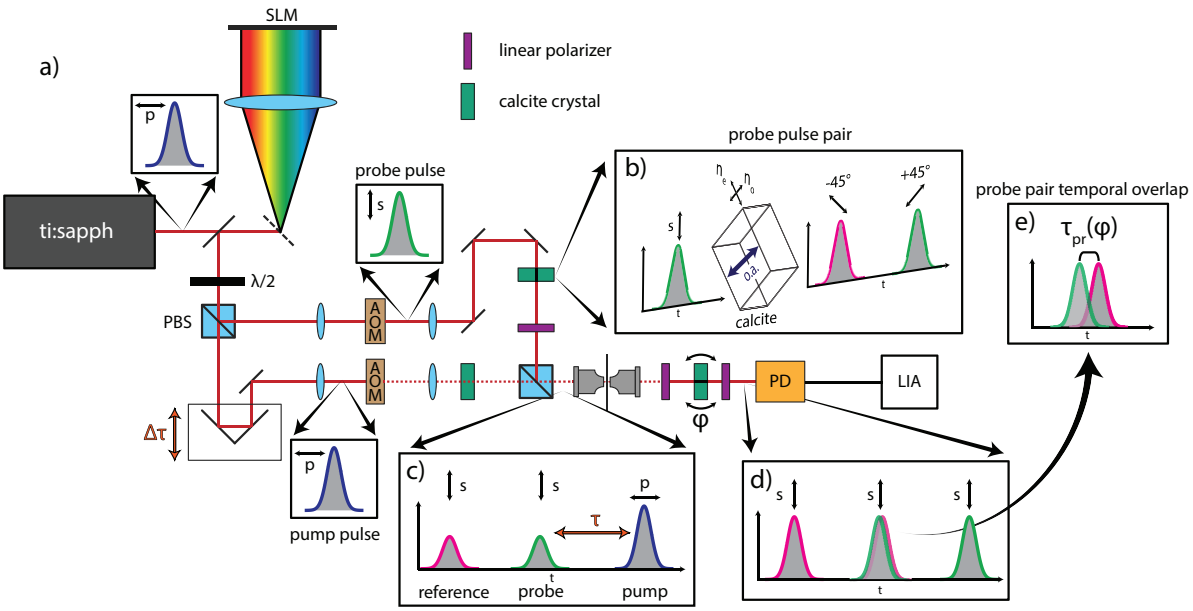

Figure 4.5: Experimental layout. a) Pump-probe experimental layout with an ultrafast pulse laser, and ultrafast pulse shaper, and a orthogonal, linearly polarized Mach-Zehnder interferometer. b) Illustration of the oriented uniaxial crystal that is used to produce a very stable probe-reference pulse pair from a single probe pulse. The pulse pair never propagates in free space ans are only delayed by a few picoseconds. Thus, the relative phase stability is extremely robust. c) When the pump pulse and probe-reference pulse pair are recombined on the output polarizing beam splitter, the probe-reference pulses are projected onto the same linear polarization direction that is perpendicular the the linearly polarized pump pulse direction. d) After the probe and reference pulses are re-timed, we have a set of three pulses, where the middle pulse comes from the interference of the probe and reference pulses and the two satellite pulses are the residual pulses projected onto the analyzer polarization direction. e) A zoomed-in view of the probe pair overlap where the temporal spacing has been exaggerated. The relative delay τ_{pr} is adjusted by manually tuning the azimuthal angle of the calcite crystal used for recombining the probe pulses.

pair is isolated with a polarizer, the time-delay is collapsed with a birefringent crystal oriented in the opposite direction of the original probe-reference pulse pair generator. The relative delay between the pulses is set to zero by adjusting the crystal angle to tune the relative delay to zero. The crystal angle is fine-tuned to adjust the relative phase so to $\pi/2$ or $-\pi/2$ to provide optimal sensitivity to the small phase shift accumulated by the probe pulse. After passing through an analyzing polarizer, the pulses interfere and convert the phase shift accumulated by the probe pulse to an amplitude modulation of the pulse interference. Note that because the probe and reference pulses were polarized along the same direction, each pulse is projected onto the ordinary and extraordinary polarization directions, so that half of the field amplitude for each pulse is further delayed in time. This is illustrated in Fig. 4.5d). The ϕ-ISRS signal is detected by an amplified photodiode (Thorlabs, PDA36A2) that is directed into a lock-in amplifier (Zurich Instruments, HF2LI).

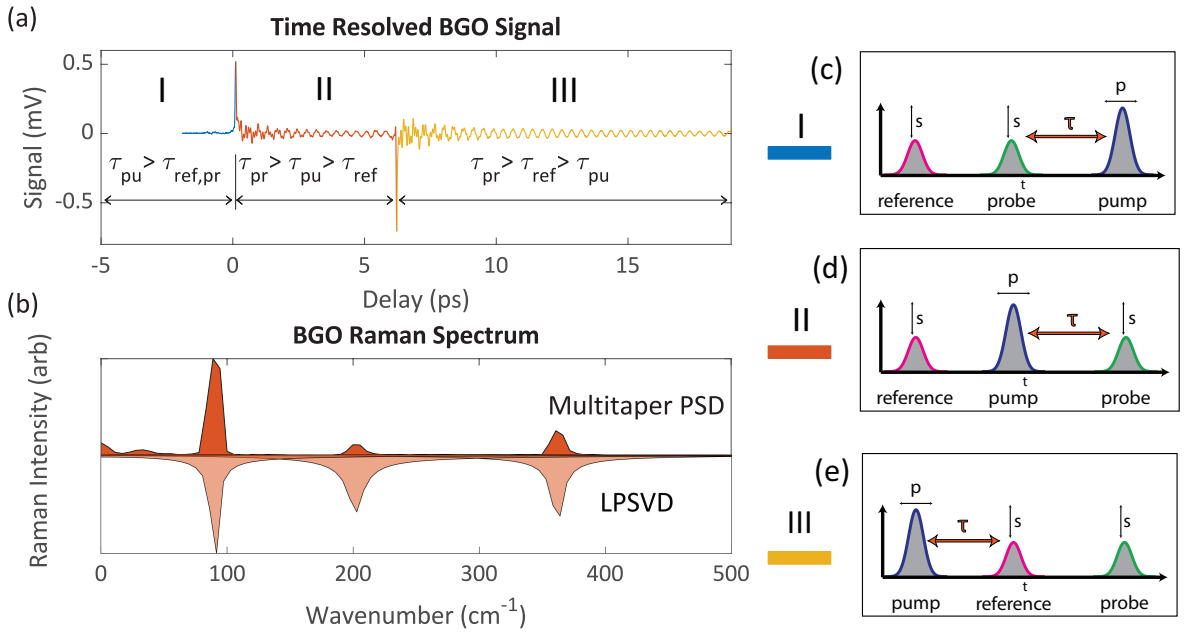

Figure 4.6: a) Three zones of probe-reference pulse delays pump probe interferometry. In zone I, the probe and the reference pulses arrive before the pump pulse. Thus the probe and reference beams experience the same thermal equilibrium phase, so there is zero phase difference between these pulses, and thus no signal. In zone II, the reference pulse arrives before the pump pulse. Next the pump pulse arrives and excites the Raman vibrational coherence that are probed by the probe pulse. Thus, the phase difference that produces the signal is from non-equilibrium phase perturbation induced by the pump pulse. Finally, in zone III, both the reference pulse and the probe pulse arrive after the pump pulse. The phase difference depends on the difference in the non-equilibrium phase probed by reference and probe pulses. b) The power spectrum estimated from Zone II gives the Raman spectrum. The upper power spectrum was determined using a multi-taper spectral decomposition in Matlab while the lower power spectrum was obtained using LPSVD. The probe and reference pulses are linearly polarized along the same direction and perpendicular to the linear pump polarization. c) Illustrates Zone I where both probe and reference pulses arrive before the pump pulse. d) Illustrates Zone II where the pump pulse arrives in-between the probe and reference pulses. e) Illustrates Zone IIII where the probe and references pulses arrive after the pump pulse.

Chapter 5

Radio Frequency Doppler Raman

Optical microscopy is a key tool in many applications, and is particularly valuable in biology where the fate and interaction of specific biomolecules must be tracked to understand processes that control the behavior of cells, tissues, and organisms. Fluorescent microscopic imaging using molecule-specific tags enables an astonishing range of biomedical studies [32]. However, many fluorescent tags are large compared to their target molecules and will modify diffusion properties and binding interactions with other molecules. Fluorescent probes face other issues such as photobleaching and technical difficulties in delivering tags to target molecules. Challenges faced by labeling and fluorescent molecule stability have stimulated intense development of label-free molecular imaging techniques [12] [3].

Other optical interactions have long been pursued for imaging the behavior of biological molecules. Of particular interest is Raman spectroscopy, which distinguishes molecules based on the intramolecular vibrational frequencies in the spectrum of inelastic light scattering from molecules in the specimen. Raman scattering is generally safe for biomedical imaging, as the visible or near infrared light used for measurements is non-ionizing, though low-level multiphoton ionization imposes an upper limit on optical peak intensity [54] and therefore limits sensitivity to low-concentration analytes. Use of visible and NIR light also enables excellent spatial resolution with Raman microscopy due to the short light wavelength and the abundance of high-quality microscope objectives.

Conventional Raman microscopy based on spontaneous Raman scattering has been widely used for cellular, tissue, *in vivo*, and plant imaging [2, 3]. However, spontaneous Raman faces severe limitations. Light interacts weakly with Raman vibrations, which is represented by the small Raman cross section per molecule – on the order of $\sigma_R \approx 10^{-30}\,\mathrm{cm}^2$. This weak cross

[3]This chapter has been adapted from "Phase noise limited frequency shift impulsive raman spectroscopy". APL Photonics, 6(2):026107, 202, with the permission of AIP Publishing.

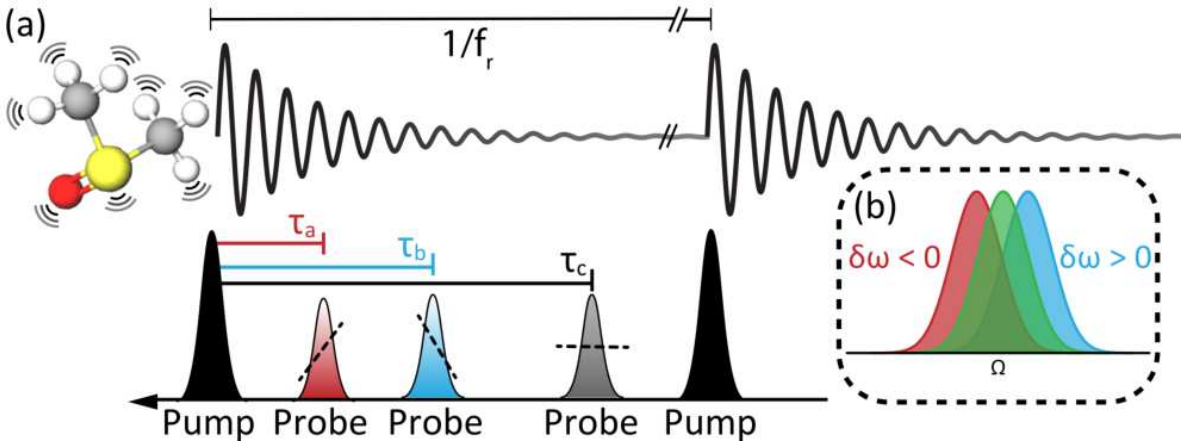

Figure 5.1: (a) A short laser pump pulse excited coherent vibrational motion leading to a time-varying perturbation of the optical susceptibility $\delta\chi^{(1)}(t;\tau) \approx 2n_{\rm pr}\delta n(t;\tau)$, where $n_{\rm pr}$ is the refractive index experienced by the probe pulse at equilibrium. A time-delayed probe pulse arriving at a delay τ after the pump pulse experiences a time-varying linear phase modulation of $\phi_{\rm mod}(t;\tau) \approx k_{\rm pr}\,\delta n(t;\tau)\ell_f$. (b) The centroid of the power spectrum of the probe pulse train is shifted by an amount given by the local slope of the accumulated phase modulation $\delta\omega(\tau) \propto -\partial\phi_{\rm mod}/\partial t$ at the pump-probe pulse delay τ.

section translates into low scattering rates. For example, illumination of a molecule with a 1 Watt light beam focused to a diameter of $150\,\mu$m leads to less than one photon scattered by the spontaneous Raman process every hour. A Raman microscope with a high numerical aperture (NA) objective produces an intense focus that increases the illumination flux in a diffraction-limited focal spot, thereby increasing the rate of Raman scattered photons measured from that volume. Still, since the focused intensity must be kept below the damage threshold, integration times of seconds to minutes are necessary to acquire Raman images. In addition, Raman spectra are usually contaminated by fluorescence emission, which further limits the ability to extract signals above the noise level. Fluorescent background interference is particularly problematic when studying plant-derived specimens [2].These challenges prevent the observation of many molecules with spontaneous Raman techniques.

The limitations of spontaneous Raman scattering motivated the development of other Raman spectroscopy techniques. Resonant Raman scattering can probe Raman spectra of weak and low concentration molecules but employs UV light that can be toxic to cells, and the signal-to-noise ratio (SNR) is still limited by the fluorescent background. Large enhancements from surface en-

hanced Raman scattering (SERS) based on field enhancements near the surface of structured metals enables single molecule detection of Raman scattering [55]. Unfortunately, applications of SERS methods are quite limited because analyte molecules must be less than a wavelength away from the metal surface.

Coherent Raman scattering (CRS) microscopy provides a substantial increase in the rate of the scattering of incident light from the Raman interaction by coherently driving vibrational motion in a stimulated Raman process [56]. By sending in pump and Stokes light fields that are separated by a frequency of a target Raman vibration, the beat frequency of the fields drives strong vibrations in the molecule, producing an amplitude significantly larger than thermally excited vibrations. CRS scattering rates are orders of magnitude higher than spontaneous Raman scattering rates. Efficiently driving CRS processes often requires phase matching, which dissuaded early efforts at CRS microscopy [56]. After the demonstration that phase matching automatically occurs in the focus of a high NA objective [57], CRS microscope technology has flourished [11]. A set of powerful label-free imaging methods with excellent chemical specificity have emerged. Large pump and Stokes field intensities boost the CRS SNR in the recorded image [11]. This SNR enhancement permits low pixel integration times – thereby enabling high-speed dynamic chemical imaging that has opened new applications.

However, the weak intrinsic scattering rate of Raman vibrations still prevents Raman spectroscopy and imaging in low concentration scenarios. While CRS signal strength can be increased with high intensity pump and Stokes fields, damage from the intense lasers prevents further scaling of the intensity [58]. Biological applications of CRS have mostly been limited to lipids, proteins (amide band), and DNA because these are the materials with the highest concentrations in cells. Molecules with low Raman scattering cross sections and concentrations fall below the limit of detection for CRS microscopy and cannot be observed. Many important biologically relevant molecules fall into this category, such as cytochromes, metabolites, and neurotransmitters.

Resonant Raman scattering is able to probe Raman spectra of weak and low concentration molecules, but employs UV light that can be toxic to cells, and the SNR is still limited by the fluo-

rescent background. Large enhancements from surface enhanced Raman scattering (SERS) based on field enhancements near the surface of structured metals enables single molecule detection of Raman scattering [55]. Unfortunately, applications of SERS methods are quite limited because analyte molecules must be in close proximity to the metal surface.

We demonstrate a new technique for measuring stimulated Raman spectroscopy whereby the amplitude of a coherently stimulated Raman signal is increased by an independent optical system. Our approach is based on impulsive stimulated Raman scattering (ISRS), in which a short pump pulse, with a duration $\tau_{\rm pu}$, efficiently excites coherent molecular vibrations in Raman-active modes with vibrational periods, $T_v = 2\pi/\Omega_v$, that are longer than the pulse duration [59]. After the arrival of the pump pulse at $\tau = 0$, the impulsively excited coherent molecular vibrations produce a time-varying perturbation to the effective linear optical susceptibility, $\delta\chi^{(1)}(t;\tau)$. The Raman vibrational coherence can be probed by measuring the transient change in optical susceptibility with a time-delayed probe pulse. Several techniques for measuring the coherent Raman spectrum based on the time-varying perturbation in refractive index (RI) have been established. ISRS spectra have been detected through Kerr lensing [21], diffraction [59], an accumulated phase shift [17–20, 44, 50], or a shift in the center frequency of the probe pulse spectrum [24, 60], i.e., a coherent Raman response-induced Doppler shift of the probe pulse spectrum, as illustrated in Fig. (5.1).

When $\tau_{\rm pr}$ is long compared to the vibrational period, the periodic phase modulation accumulated by the pulse produces equal-amplitude Stokes and anti-Stokes sidebands on the probe pulse spectrum [50, 61]. A number of methods have been adopted to measure the Raman spectrum by recording pump-probe delay traces of the power transmitted through a spectral filter [16, 24, 30, 41, 62] or through subsequent nonlinear signal generation [63, 64]. In particular, the method of recording the Raman spectrum with probe pulse transmission through a spectral filter is routinely used for measuring low-frequency optical phonon vibrational spectra [41]. The phase shifting, frequency shifting, and nonlinear frequency conversion methods are all time-domain Raman techniques, so that the complex Raman spectrum is obtained by Fourier transforming the recorded probe pulse signal. All these previous methods convert the change in RI or the frequency

shift to a change in optical power that is detected to record a Raman spectrum. As a result, all these measurements are limited by noise in light power detection. RFDR spectroscopy allows us to break free of this limitation in detecting Raman vibrational coherence-mediated Doppler shifts, opening the potential for much more sensitive Raman spectroscopy detection.

5.1 Radio frequency Doppler Raman (RFDR) spectroscopy

A quantitative understanding of RFDR spectroscopy requires a model for the excited, time-varying optical susceptibility and subsequent probe pulse interaction. For a single vibrational mode with frequency Ω_v, the time-varying optical susceptibility takes the form [20, 65] $\delta\chi^{(1)}(t;\tau) = \delta\chi_0^{(1)} F_v(t-\tau)$, where $\delta\chi_0^{(1)}$ is the peak change in susceptibility , $F_v(t) = \Theta(t)\exp(-\Gamma_v t)\sin(\Omega_v t + \phi_v)$, Γ_v is the linewidth of the vibrational resonance, ϕ_v is a phase shift imposed by ISRS, and $\Theta(t)$ is the Heaviside step function that enforces causality. The expression for the optical susceptibility perturbation assumes a laser pulse with a peak pump pulse intensity, $I_{0,\mathrm{pu}}$, and a pulse duration, τ_{pu}, shorter than the excited vibrational modes.

Raman spectra are acquired following ISRS by the pump pulse by scanning the arrival time, τ, of a probe pulse. The probe pulse propagating through the Raman-excited medium at a delay time τ accumulates a phase shift given by $\delta\phi(\tau) = \delta\phi_0 F_v(\tau)$, where the peak phase shift, $\delta\phi_0 = k_{\mathrm{pr}}\,\ell_f\,\delta n(0;\tau)$, imparted onto the probe pulse for the Gaussian pump pulse model reads [65]

$$\delta\phi_0 = -\frac{2}{\tilde{\Omega}_v f_R}\,\beta_{\mathrm{ISRE}}\,g\,\mathrm{Im}\{\chi^{(3)}(\Omega_v)\}\,p_{\mathrm{pu}} \tag{5.1}$$

with pump probe beam focusing conditions given by

$$g = \frac{6\pi}{n_{\mathrm{pu}}\,n_{\mathrm{pr}}\,A_f\,c\,\epsilon_0}\left(\frac{\ell_f}{\lambda_{\mathrm{pr}}}\right) \tag{5.2}$$

Here $\tilde{\Omega}_v = \sqrt{\Omega_v^2 - \Gamma_v^2}$ is the reduced vibrational frequency, $\chi^{(3)}(\Omega_v)$ is the third order non-linear susceptibility evaluated at the resonance frequency of the molecular vibration, $\beta_{\mathrm{ISRS}} = \tilde{\Omega}_v\Gamma_v\exp[-(\Omega_v\tau_{\mathrm{pu}}/2)^2]$ is the ISRS parameter, and $f_R = 1/T_R$ is the repetition rate of the pump

and probe pulse trains. We have denoted the pump pulse train average power, interaction length of the focused probe beam, cross sectional focal beam area, and pump pulse refractive index as p_{pu}, ℓ_f, A_f, and n_{pu}, respectively, and n_{pr} and λ_{pr} are the refractive index and the center wavelength of the incident probe pulse. Near the center of the probe pulse at a delay $(t-\tau)$, there is a linear phase ramp that imparts a generalized Doppler frequency shift, moving the centroid of the optical power spectrum by $\delta\omega \approx \delta\omega_0\, G_v(\tau)$. The peak frequency shift is $\delta\omega_0 = \delta\phi_0\, \Omega_v$ and the delay dependence of $G_v(\tau) \approx \exp(-\Gamma_v\tau)\cos(\Omega_v\tau+\phi_v)$ is used to obtain the time-domain Raman spectral signal [1, 25].

To motivate the need for small frequency shift detection, we note that the Doppler frequency shifts due to ISRS increase in direct proportion to the third-order Raman susceptibility, $\delta\omega_0 \propto \mathrm{Im}[\chi^{(3)}(\Omega_v)]$. The third-order optical susceptibility scales with the number density of molecules, N, as $\chi^{(3)}(\Omega_v) = N\,\langle\gamma^{(3)}(\Omega_v)\rangle/\epsilon_0$. Here ϵ_0 is the dielectric permittivity of free vacuum and $\langle\gamma^{(3)}(\Omega_v)\rangle$ is the orientational averaged second hyperpolarizability at the resonant vibrational frequency [17, 66]. The second hyperpolarizability $\gamma^{(3)}(\Delta\Omega) = \gamma^{(3)}_{\mathrm{NR}} + \gamma^{(3)}_{\mathrm{VR}}\, f_v(\Delta\Omega)$ exhibits a non-resonant electronic contribution to the second hyperpolarizability $\gamma^{(3)}_{\mathrm{NR}}$ and a vibrational Raman response with an amplitude $\gamma^{(3)}_{\mathrm{VR}}(\Omega_v) = -(12\,i\,\Gamma_v\,\Omega_v)/(\partial\alpha/\partial Q_v)_0$ at resonant vibrational frequency, Ω_v, and a resonant spectral response of $f_v(\Delta\Omega) = -2\,i\,\Gamma_v\,\Omega_v/(\Omega_v^2 - \Delta\Omega^2 + 2\,i\,\Gamma_v\Delta\Omega)$ [13]. The magnitude of the Raman response is characterized by the derived polarizability, $(\partial\alpha/\partial Q_v)_0$, of a vibrational mode. From the model, it is clear that the frequency shifts $(\delta\omega)$ are linearly proportional to the molecular concentration. To reach improved Raman detection sensitivity, we leverage advances in the measurement of timing jitter from precision optical metrology [67, 68] to detect small ISRS-induced Doppler frequency shifts on the probe spectrum by converting kilohertz optical frequency shifts into nanosecond-scale pulse timing shifts through a dispersive element [69].

To apply precision metrology methods to ISRS detection, we convert the optical Doppler frequency shift imparted to the probe pulse train, $(\delta\omega)$, into a time shift using the technique illustrated in Fig. (5.2). We pass the probe pulse train that has accumulated a frequency shift $(\delta\omega)$ through an optically dispersive system with a group delay τ_g that can be approximated as $\tau_g \approx \tau_{\mathrm{g0}} + \varphi_2\,\delta\omega$,

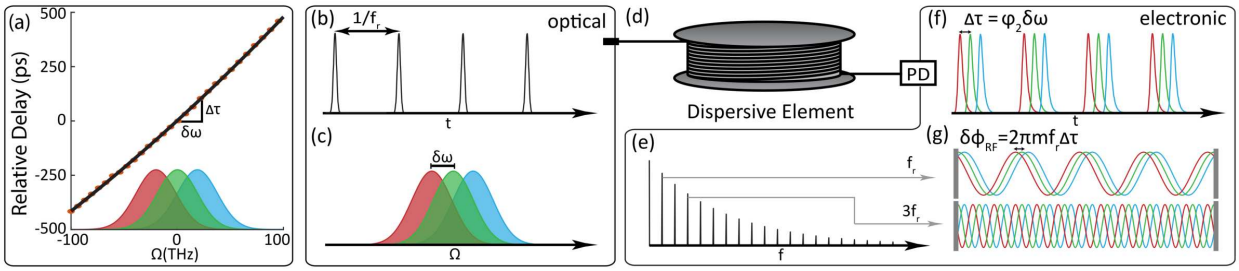

Figure 5.2: (a) A dispersive optical system maps the frequency shift of the probe pulse to a change in transit time through the optical fiber due to group delay dispersion GDD $= \varphi_2$. The probe pulse optical pulse train (b) accumulates a frequency shift (c) due to propagation through the vibrational coherence prepared by the pump pulse. (d) The frequency shift is converted to a change in time of flight through a length of multimode fiber (MMF) whereupon a photodiode (f) converts the optical pulse train to an electronic pulse train. The m^{th} harmonic of the pulse repetition frequency (e) is isolated electronically and a phase detector is used to record the RF phase shift (g), which is the measurement of the Raman excitation.

where φ_2 is the group delay dispersion (GDD) and τ_{g0} is the transit time through the dispersive optical system for probe pulses at the original center frequency ω_0. A change in the center frequency of the probe pulse is thus converted into a change in transit time through the dispersive optical system, $\Delta\tau = \tau_g - \tau_{\mathrm{g0}} = \varphi_2\,\delta\omega$. In RFDR, the energy of the pump pulse is sinusoidally modulated with an acousto-optic modulator (AOM) at a frequency f_{m}, which also modulates the pump-induced Doppler frequency shift. After passing through the dispersive system, the Doppler frequency shift is encoded in the probe pulse train as a sinusoidal timing jitter. The pulse train field is modeled as $\tilde{E}_{\mathrm{pr}}(t) = \sum E_{\mathrm{pr}}(t - j\,T_R - \Delta\tau\,\sin(f_m\,t) + \delta\tau)$. Here T_R is the laser pulse spacing and $\delta\tau$ is a random variable denoting the laser oscillator pulse train timing jitter. The rms timing jitter noise, $\delta\tau_{\mathrm{rms}} = \sqrt{\int_{f_1}^{f_2} S_{\delta\tau}\,(f)\;df}$, depends on the timing jitter power spectral density (PSD), $S_{\delta\tau}$, integrated over the detection bandwidth, $\Delta f = f_2 - f_1$. The timing jitter noise sets the limit on how small of an RFDR-induced timing jitter can be detected, from which we define $\mathrm{SNR} = \Delta\tau/\delta\tau_{\mathrm{rms}}$. By inducing a periodic RFDR-induced timing jitter, the RFDR signal can be detected with high sensitivity using a lock-in amplifier at large offset frequencies that exhibit low noise using a system adapted from methods for precision timing jitter noise characterization [67]. The induced sinusoidal probe pulse timing jitter is detected by an RF phase shift of a harmonic of the pulsed electronic signal that is produced in a photodiode (PD) [70].

Whereas RFDR records Raman spectra through measuring timing jitter, other CRS methods record Raman spectra by detecting a change in optical probe power relative to the average probe pulse power. Both methods are subject to shot noise, but with distinct scaling characteristics. The SNR of CRS, including stimulated Raman scattering (SRS) and RFDR, scales as $\mathrm{SNR} = \rho_j \; g \; p_{pu} \; \mathrm{Im}\left[\chi^{(3)}\right] \sqrt{\Delta t}$. For an equivalent optical experimental setup, differences in detection sensitivity arise from the term ρ_j. The shot noise in SRS and spectral filter detection of ISRS scales as $\rho_{\mathrm{SRS}} \propto \sqrt{p_{pr}}$, whereas shot noise in RFDR scales linearly in power, $\rho_{\mathrm{RFDR}} \propto p_{pr}$ because the relevant shot noise in the RF signal used for timing jitter detection is determined by the RF signal power. Thus, RFDR offers a favorable SNR scaling that outperforms SRS.

SRS is also subject to laser relative intensity noise (RIN), and for a large enough probe pulse average power the SRS noise is proportional to $\rho_{\mathrm{RIN}} \propto \sqrt{2} \; \beta \; 10^{-\frac{\sigma_{\mathrm{RIN}}}{20}}$, however, RIN can be mitigated by balanced detection strategies. RFDR is not susceptible to RIN fluctuations to first order because the Raman spectroscopy information is encoded in the arrival time of pulses in the pulse train, rather than in power fluctuations as with SRS. In this first demonstration of RFDR, the timing jitter is limited by shot noise that appears in the electronic RF phase detection. The sensitivity of RFDR is ultimately limited by the mode-locked oscillator timing jitter noise, which is significantly lower than the timing jitter noise imposed by electronic RF phase detection.

5.2 Methods

The Raman signal is transformed from a generalized Doppler frequency shift of the probe pulse that arises from ISRS-induced time-dependent effective optical susceptibility perturbation. A dispersive element converts this generalized Doppler shift into an ISRS-induced timing jitter on the probe pulse train. The DR timing jitter is extracted using direct electronic detection by comparing the RF probe signal phase to a reference RF signal phase obtained from a reference pulse train [67]. A schematic of the RFDR experimental system is shown in Fig. (5.3). Pulses from a mode-locked Ti:sapphire laser (KM Labs) are sent through an ultrafast pulse shaper to ensure the delivery of transform-limited pulses in the experiment. The pulses exiting the shaper are di-

rected into a polarization-based Mach-Zehnder interferometer with a scanning mirror delay line to produce pump and probe pulses with controllable relative pump-probe delay τ. The intensity of the pump pulse train is modulated with an acousto-optic modulator (AOM, Brimrose) at the modulation frequency f_{m}. The pump and probe pulses are recombined with orthogonal linear polarizations using a polarizing beam splitter (ATF, PBS1005-GVD). The pump-probe pulse pair is focused into a cuvette with an aspheric lens (Newport New Focus. The pump and probe pulses are compressed to the transform limit by optimizing the intensity of two-photon absorption fluorescent emission from a bath of yellow highlighter ink diluted in water and placed in the cuvette. The pulses are recollimated with a matched aspheric lens, then passed through a polarizer to reject the pump pulses. The probe pulse train is coupled into a gradient index MMF (Thorlabs, GIF625) with fiber length L_{fiber} with $\approx 35\%$ coupling efficiency and is detected with a fiber-coupled PD (Thorlabs, DET02AFC) on the distal end of the fiber. The recorded RFDR signal results from detection of modulations to the probe pulse timing delay created by the DR frequency shift-to-timing delay converter (dispersive system). Electronic-based timing jitter measurements work by carefully conditioning two RF signals to implement a RF double balanced mixer as a RF phase detector. A RF double balanced mixer can be operated as a phase detector when two RF signals of the same frequency are injected into the mixer with sufficient RF power to drive the mixer into saturation. RF phase detection is accomplished by measuring the relative RF phase shift between the probe-generated RF signal with Raman vibrational coherence-induced timing jitter and a stable RF reference local oscillator (LO). To create an appropriate RF signal for phase detection, the m^{th} harmonic of the laser oscillator repetition rate (f_R) is isolated by passing the electronic signal generated by the PD through a high-quality RF bandpass filter centered at a frequency $\nu_m = mf_R$. The RF local oscillator (LO) is derived from a small portion of light from the laser that is detected with a matched PD, filtered, amplified (Holzworth, HX2400), and then injected into the LO port of the mixer (Minicircuits, ZX05-1MHW-S+). To ensure the mixer operates as a phase detector, the filtered RF harmonic power is tuned with an adjustable RF attenuator and low phase noise amplifiers.

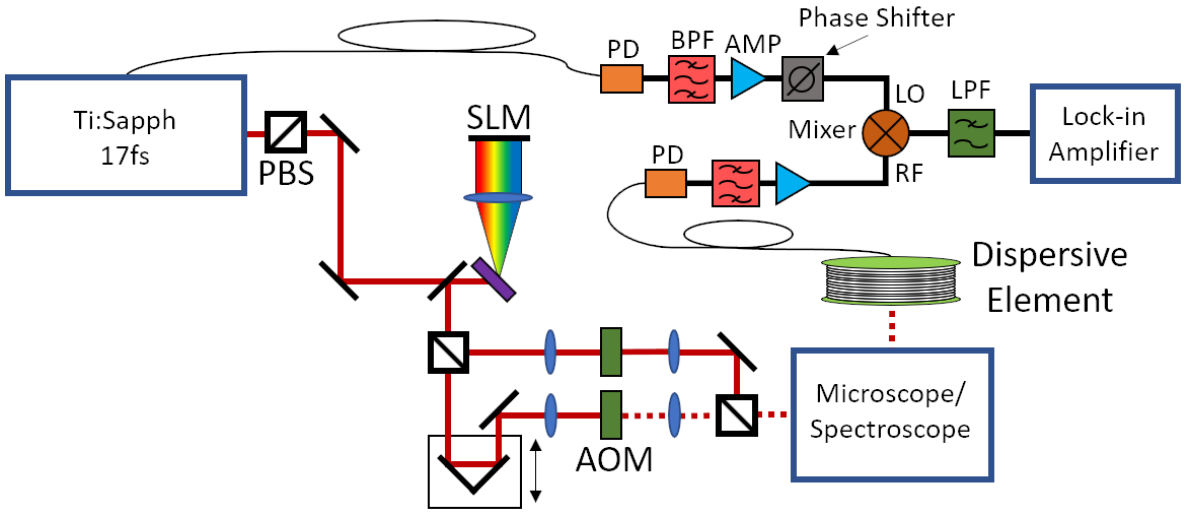

Figure 5.3: Experimental setup for RFDR spectroscopy.

To first order, the saturated RF mixer (phase detector) reduces RF amplitude fluctuations, which rejects RIN. While no RF phase detector is ideal, modern phase detectors perform exceptionally well in this regard, exhibiting very low amplitude-to-phase noise conversion. In addition, the RIN incident on each PD in the RFDR experiment will lead to fluctuations in the photocurrent that are correlated between each detector. Thus, any residual RIN noise will be cancelled in the phase detector. To ensure maximum phase-to-voltage sensitivity, a passive RF phase shifter is used to adjust the input RF and LO signals to be in quadrature. The intermediate frequency (IF) output of the mixer is low-pass filtered, preamplified, and connected to a lock-in amplifier.

To record Raman spectra, data reporting the amplitude of the modulation of the RF phase shift imparted by the modulated pump pulse energy that varied the excitation strength of the vibrational coherence are directly acquired from the lock-in amplifier (Zurich Instruments) as a function of pump-probe delay. At a fixed pump-probe time delay, τ, the time-varying strength of the excited vibrations caused a time-varying center frequency shift, and thus a time-varying change in the transit time of the probe pulse train through the optical fiber, which is finally reflected as a sinusoidal modulation of the RF harmonic phase.

5.3 Results

The electronic RF phase measurement of the DR-induced timing jitter detected at the m^{th} harmonic of the laser repetition rate frequency, f_R, introduces several noise sources that degrade the minimum detectable timing jitter value [70]. Through careful choices of RF electronic components, we operate at the RF phase noise detection limit set by the photodetection process. The lowest measurable timing jitter PSD, $S_{\delta\tau}$, with electronic phase noise detection is set by the shot noise-induced RF phase noise that is determined by the average RF power generated in the PD by the probe pulse. With a given probe pulse-generated RF power, p_{RF}, at the frequency mf_R, the timing jitter PSD is given by $S_{\delta\tau} = h\nu/2\ p_{\mathrm{RF}}\left(\pi m f_R\right)^2$. Here h is Planck's constant and ν is the center optical frequency. As the dispersion (parameterized by φ_2) of the frequency-to-time delay converter is increased to increase the RFDR signal, the increased probe pulse duration produces a nonlinear drop in RF power with increasing harmonic order m. As a result, the shot noise, and commensurately $S_{\delta\tau}$, increases nonlinearly with increasing harmonic order. Thus, even though the RF phase shift ($\delta\phi_{\mathrm{RF}}$) scales linearly with harmonic order m, $\delta\phi_{\mathrm{RF}} = 2\pi f_R m\varphi_2\delta\omega$, there is diminishing returns in terms of SNR when moving to high harmonics because the phase shot noise level rises nonlinearly while the signal is increasing linearly, provided that we operate at the shot noise limit.

The 500 m segment of MMF used for most measurements imparted a GDD of $\varphi_2 = 22.5\ \mathrm{ps}^2$ onto the probe pulses. This value of φ_2 produces a frequency shift to transit delay mapping of $\Delta\tau = 0.14\ \mathrm{fs/MHz}$. The minimum detectable frequency shift, $\delta\nu_{\mathrm{min}}$, and thus the minimum detectable molecular concentration, is computed by setting the SNR to unity, giving $\delta\nu_{\mathrm{min}} = \sqrt{S_{\delta\tau}\left(f_m\right)}/2\varphi_2\sqrt{2\Delta t}$. Here, we assume that the timing jitter noise PSD, $S_{\delta\tau}$, is approximately constant across the detector bandwidth $\Delta f = 1/(2\Delta t)$, which is characterized by the integration time Δt for the offset frequencies centered at the AOM modulation frequency (f_m) imparted onto the pump pulse train. The first and second harmonics performed similarly, and most measurements were recorded at $m = 2$. The minimum detectable frequency shift for our experimental scenario is $\delta\nu_{min} = 1.2\ \mathrm{MHz\ s}^{0.5}/\sqrt{\Delta t}$. In our experiments we find that, averaging over 7 scans, we measure

a minimum frequency shift of $\delta\nu_{min} = 9.08$ MHz compared to the estimated minimum value of 8.54 MHz determined by the shot noise floor – demonstrating operation of RFDR spectroscopy within 6% of the shot noise limit for electronic RF phase noise detection.

Fig. (5.4) shows a typical time-resolved response recorded with RFDR for dimethyl sulfoxide (DMSO). Raman spectra are recovered from the time-resolved Raman response by estimating the signal power spectrum using multitaper PSD estimation or using linear prediction singular value decomposition (LPSVD); the power spectrum is shown in the inset of Fig. (5.4). The exceptional dynamic range of the RFDR system is demonstrated in the system's ability to resolve the large cross phase modulation signal at $\tau = 0$ while the upper inset shows the exponentially decaying Raman response of the sample and the lower inset shows the measured Raman spectrum of dimethyl sulfoxide (DMSO). The cross-phase modulation peak to the system noise floor represents a dynamic range of more than 5 orders of magnitude.

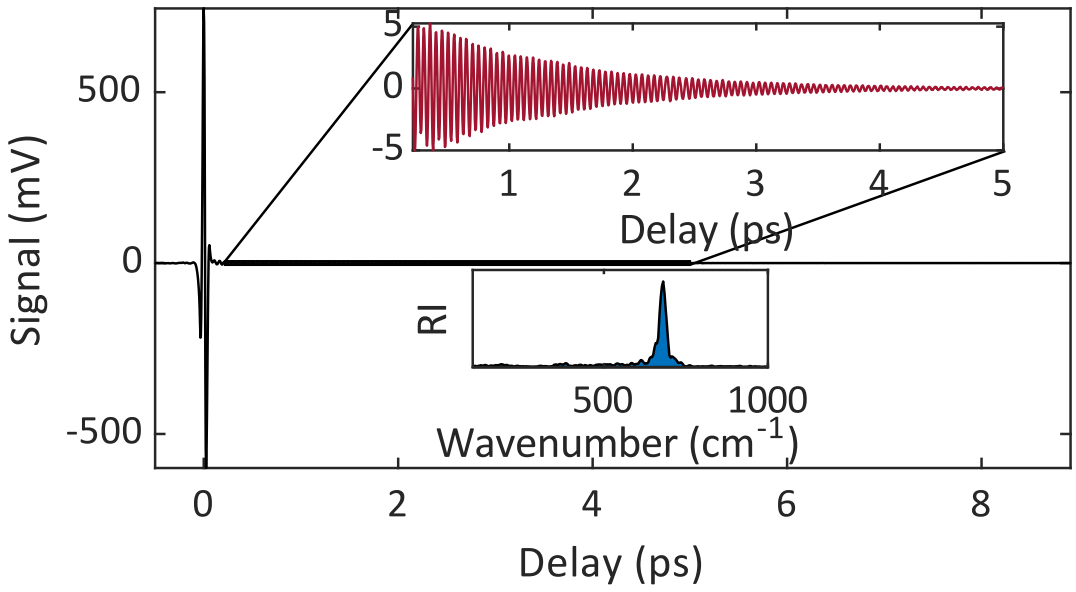

Figure 5.4: Time Resolved signal from 200mM DMSO. The large cross phase modulation peak is visible with the Raman response (upper inset), highlighting the dynamic range of the measurement system. The Raman spectrum recovered using multitaper PSD estimation (time-half bandwidth product, $TW = 2.25$, samples $N = 2114$, and 3.5 Slepian tapers) is shown in the lower inset.

The detected RF phase shift signal in RFDR is given by the simple formula, $\delta\phi_{\mathrm{RF}} = 2\pi f_r m\varphi_2\delta\omega$, that shows the signal is linearly proportional to the detected phase shift with harmonic order m and the GDD (φ_2). We confirmed the linear scaling of with these quantities experimentally. The RF phase measurements also depend on the parameters of the RF mixer used as a phase detector and details of the RF power levels used to saturate the mixers. Linearity of the scaling with harmonic order was verified by operating with a single mixer with carefully adjusted RF power levels to ensure similar mixer saturation conditions across harmonics. Furthermore, the optical Doppler frequency shift, $\delta\omega \propto [C]$, is expected to scale linearly with the molecular concentration, $[C]$. The expected linearity of the scaling of the RFDR spectroscopy signal with concentration is shown in Fig. (5.5 a). To establish the sensitivity limit of the current RFDR spectroscopy system, concentration studies with DMSO were performed. DMSO was selected because it is easily diluted with deionized (DI) water, which lacks a detectable Raman response with RFDR spectroscopy. A series of dilutions were prepared using neat DMSO and DI water to obtain DMSO concentrations from 200 mM to 0.5 mM. A flow-through quartz cuvette was mounted in the specimen plane of the spectroscope. A syringe with 15 mL of DMSO solution was flushed through the flow-through cuvette hosing lines, filling the cuvette with the solution. Data was recorded before repeating the solution flushing three times for each concentration. The syringe volume was sufficient to fully flush the previous solution from the flow-through cuvette before each data run. 15 mL of DI water was plunged through the cuvette between each concentration to prevent contamination from prior solutions. Further, the concentration study started from the lowest concentration (0.5 mM) to further mitigate the potential of contamination from prior solutions. The pump and probe powers for the concentration study were 80 mW and 49 mW respectively. The time-resolved data was processed using LPSVD to recover the peak amplitude for the $667\mathrm{cm}^{-1}$ mode of DMSO. The rms noise floor shown with the dashed line in Fig. (5.5 a) was measured by performing a data run with DI water in a flow-through cuvette, and these values are consistent with independent measurements of the shot noise limited timing jitter noise shown in the Supplemental Information. Fig. (5.5 b) shows LPSVD-derived Raman spectra for a concentration study with the metabolite

flavin adenine dinucleotide (FAD). Raman spectra for several metabolites, which have relatively weak Raman cross sections, are shown in Fig. (5.6) and show excellent agreement with Raman spectral peaks previously reported in the literature [71–77], which are marked with an asterisk.

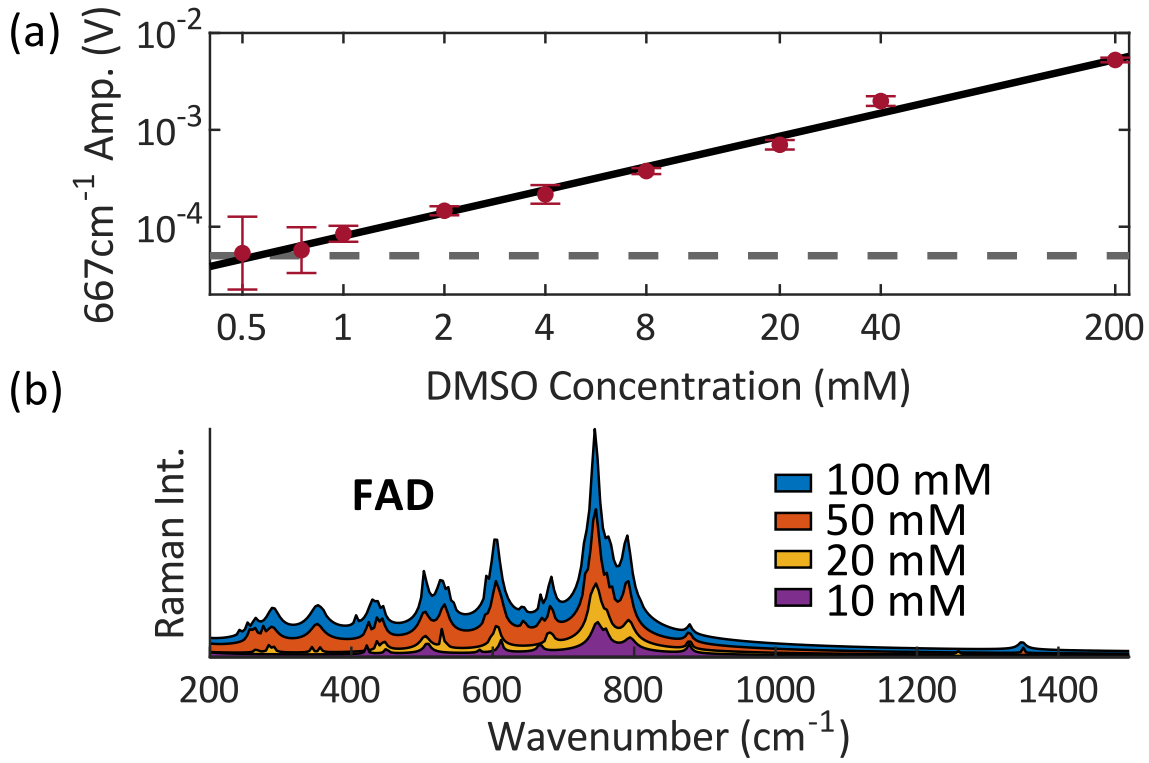

Figure 5.5: (a) Scaling of the RFDR signal strength of the 667 cm^{-1} mode of DMSO with concentration. The dashed line represents the current system noise floor. (b) Flavin adenine dinucleotide (FAD) spectra are shown as a function of concentration.

RFDR spectroscopy was used to observe differences in redox states of the biologically significant molecule nicotinamide adenine dinucleotide (NAD^{+}) prepared in DI water. In Fig. (5.7 a) significant differences in the spectra are seen, particularly the presence of the $1038\mathrm{cm}^{-1}$ mode with (NAD^{+}). This result agrees well with previous studies [74]. Fig. (5.7 b) shows RFDR spectra from 2mM cytochrome *c* in phosphate buffered saline (PBS) where peaks that agree with previous literature have been marked [78]. Fig. (5.7 c) shows the spontaneous Raman spectrum from the same cytochrome *c* sample. The spontaneous Raman spectrum was recorded using a home-built spontaneous Raman microscope with pump wavelength ~~$\lambda_{pump} = 532$ nm~~ $\lambda_{pump} = 785$ nm.

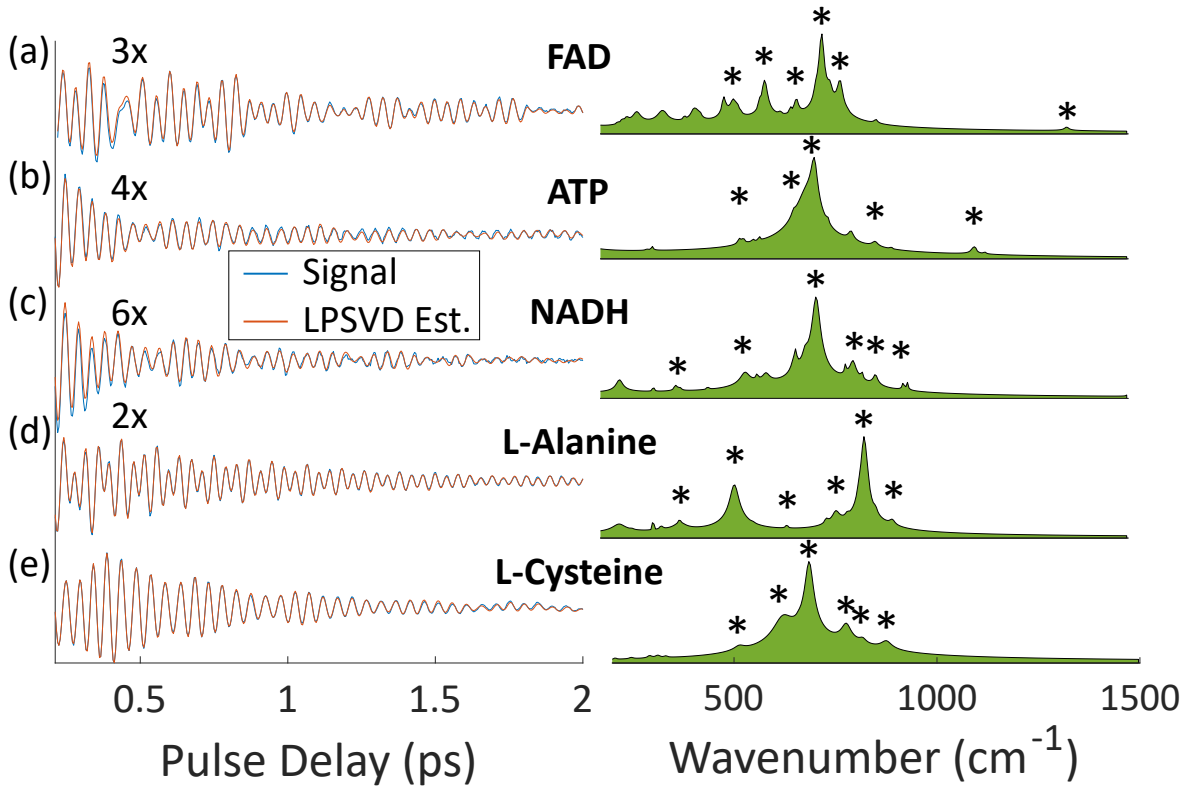

Figure 5.6: Time-resolved Raman spectra of biological molecules measured with RFDR spectroscopy. Signals with linear prediction singular value decomposition (LPSVD) model estimates are shown at left. The scale factors shown indicate by how much the time-resolved signal was scaled for plotting on a consistent axis. Raman spectra reconstructed using LPSVD are shown at right where peaks corresponding to previously reported literature values are marked. (a) 100mM flavin adenine dinucleotide (FAD) in PBS. (b) 100mM adenosine triphosphate in DI water. (c) 100mM nicotinamide adenine dinucleotide (NADH) in PBS. (d) 0.5M L-alanine in PBS. (e) 1M L-cysteine in PBS.

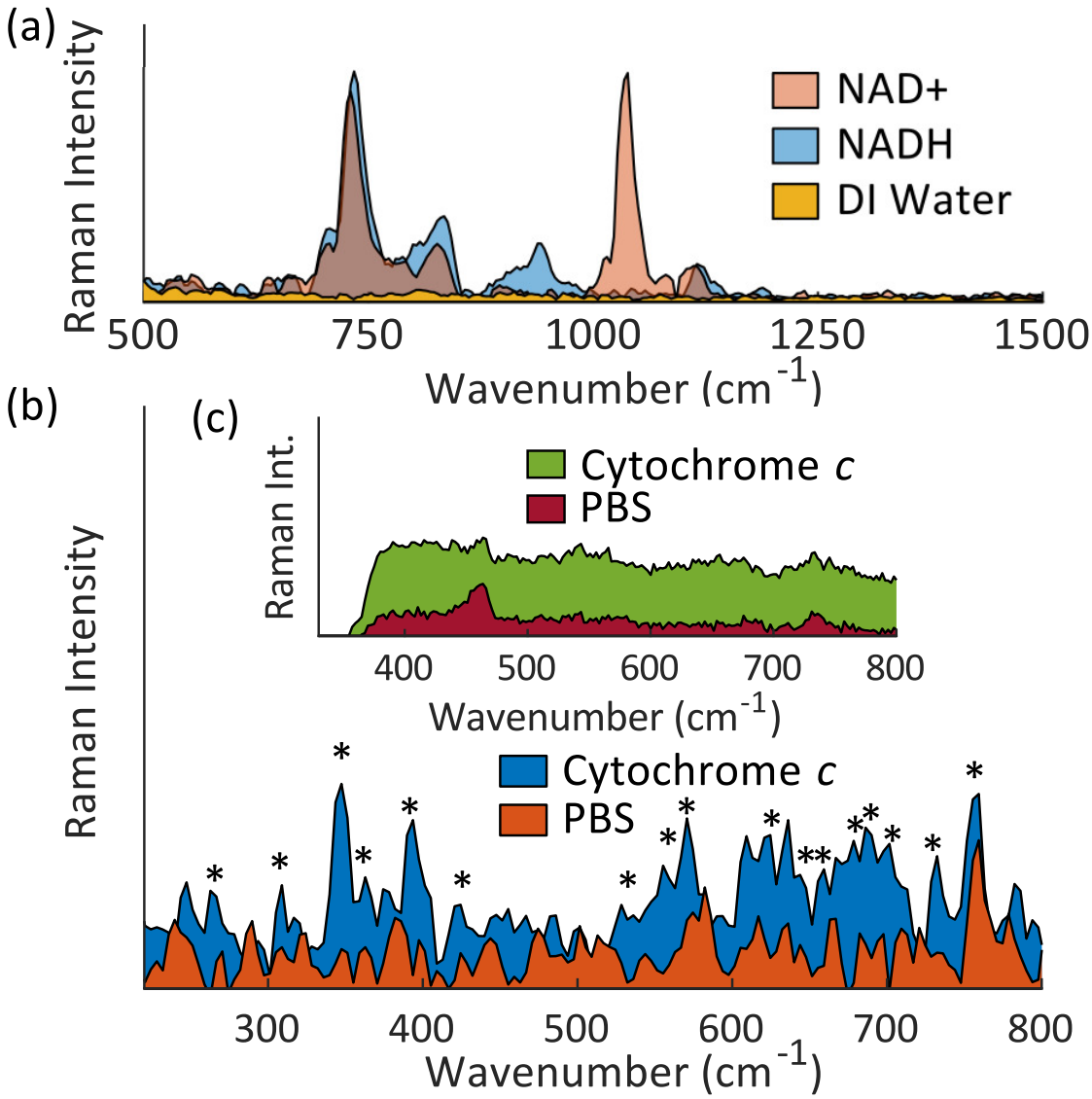

Figure 5.7: (a) DR spectra for NAD+ and its reduced form, NADH, are shown with a DI water background. (b) DR spectra from 2mM cytochrome *c* in phosphate buffered saline (PBS). (c) Spontaneous Raman spectrum of 2mM cytochrome *c* in PBS.

The spontaneous Raman spectrum is dominated by fluorescence background from the fluorescent oxidized form of cytochrome *c*, masking any Raman peaks. RFDR spectroscopy is immune to the fluorescence background that can be prohibitive with spontaneous Raman and similar to other ISRS-based systems, RFDR readily detects low frequency Raman modes that can be difficult to record with spontaneous Raman and other coherent Raman techniques. For this initial experimental implementation, acquisition speed is not representative of the ultimate potential because we are using stepper motors to take a full time-domain pulse delay scan. With the current system, a single 8 ps delay scan with full Raman vibrational information takes ≈ 1.8 s. The data presented in the paper was taken with either 7 ps or 8 ps delay scans, corresponding to spectral resolutions of $4.77\mathrm{cm}^{-1}$ and $4.17\mathrm{cm}^{-1}$, respectively. There are straightforward paths to much faster acquisition times with voice-coil based rapid scan delay lines capable of scanning 20 ps+ at 30 Hz [79].

5.4 Discussion

The motivation of RFDR spectroscopy is to boost the SNR of Raman spectroscopy measurements to push to lower concentration detection limits and to detect molecules with very weak Raman cross sections. RFDR spectroscopic detection offers a unique pathway for ultrasensitive Raman detection because of two primary benefits. Firstly, the Raman signal is amplified in a dispersive medium when the small optical center frequency shift ($\delta\omega$) accumulated by a probe pulse is converted into a timing shift ($\Delta\tau$) by the applied dispersion. By leveraging dispersion, the coherent Raman signal is optically amplified beyond the limits set by damage at the focus, where other coherent Raman techniques are constrained. The second major advantage is more favorable detection SNR compared to conventional methods as the conversion of the optical frequency shift to a timing shift opens a new possibility for very low noise measurements because mode-locked ultrafast oscillators display exceptionally low timing jitter noise. The noise floor (and thus minimum molecular concentration) for RFDR measurements is the mode-locked pulse train timing jitter PSD, rather than the shot noise intensity and RIN that set the noise floor for all other CRS methods, such as SRS [14] and spectral filter detection of ISRS. Extremely low molecular con-

centration detection through RFDR spectroscopy is feasible because mode-locked laser oscillators exhibit extraordinarily low levels of timing jitter, $\delta\tau_{\mathrm{rms}}$ (and thus phase noise at harmonics of the repetition rate of the laser).

To appreciate the advantage of the amplified time delay measurement of RFDR over conventional measurements that detect CRS signals through a change in probe power, we consider noise levels of various experimental systems. At the limiting value of GDD, where the probe pulse temporal duration reaches the pulse train separation f_R^{-1}, then $\varphi_2 = \tau_0/f_R$, and we reach a maximum $\mathrm{SNR} = \delta\omega\tau_0\sqrt{2\Delta t}/f_R\sqrt{S_{\delta\tau}(f_m)}$. Mode-locked oscillator timing jitter PSDs of $S_{\delta\tau} \sim 10^{-b}\ \mathrm{fs}^2/\mathrm{Hz}$ with $b > 10$ have been measured at offset frequencies $> 1\ \mathrm{MHz}$ where the timing jitter PSD can be approximated as constant over the detector integration bandwidth [67,80]. Under typical conditions, the equivalent RIN required, $\sigma\mathrm{RIN} \approx -200\ \mathrm{dBc}$, is orders of magnitude lower than RIN levels of any laser source. Mode-locked lasers with high stability achieve $\sigma\mathrm{RIN} \approx -150\ \mathrm{dBc}$, which for an integration time of $\Delta t = 300\ \mu s$, conventional CRS methods based on probe power pulse changes, such as SRS and spectral filter detection ISRS, are limited to a concentration limit of detection of approximately $[\mathrm{CCl_4}]_{\mathrm{min}} \approx 5\ \mathrm{mM}$. In contrast, RFDR accesses the low timing jitter noise floor, and for the same integration time, concentrations below $\mu\mathrm{M}$ may be accessible.

5.5 Conclusion

We have demonstrated a new concept for coherent Raman spectroscopy that optically amplifies the Raman signal by converting the generalized Doppler Raman (DR) frequency shift into a timing jitter modulation. The transformation of the Raman signal into a timing jitter allows access to lower noise levels than is possible with the conventional optical power perturbation detection techniques for CRS. While the measurements presented in this work are limited by the style of electronic RF phase noise detection, this work demonstrates the potential of RFDR spectroscopy for unprecedented low concentration Raman detection by exploiting the exceptionally low timing jitter of mode-locked ultrafast lasers. Improved RFDR phase detection methods will open the

possibility unprecedented low molecule concentration detection without the need for local field enhancements. Moreover, RFDR spectroscopy, unlike spontaneous Raman, is not strongly impacted by fluorescent emission and is thus useful for label-free spectroscopy in environments with high levels of autofluorescence, such as plants. In this Article, we have shown the ability to record Raman spectra from a range of molecular components, some of which are involved in plant metabolic activity, and also demonstrated the ability to differentiate the redox state of $\mathrm{NADH}/\mathrm{NAD}^+$ with RFDR spectra.

5.6 Supplements

RFDR spectroscopy relies on the generalized Doppler frequency shift that arises from the time-varying refractive index (RI), $n_{\mathrm{mod}}(t)$, that is produced in a Raman-active medium by the vibrational coherence that is prepared by a short pump pulse. The Doppler shift derives from a time-dependent change in optical path length (OPL), $\mathrm{OPL} = n\,\ell$, the product of the RI, n, and the propagation length, ℓ. Due to the time variation in OPL, the optical phase, $\phi(t) = k_0\,\mathrm{OPL}(t)$, accumulated by the propagating light is phase-modulated. Here $k_0 = \omega_0/c$ is the free space wavenumber, ω_0 is the optical frequency, and c is the speed of light. The time-varying phase modulation leads to a change in the wave (here light) frequency, $\delta\omega = -\partial\phi/\partial t - \omega_0 = -k_0\,\partial\mathrm{OPL}(t)/\partial t$. There are two origins of this effect that follow from applying the chain rule to a time-derivative of the time-varying OPL, $\partial\mathrm{OPL}(t)/\partial t$: 1) the conventional Doppler shift arising from the relative motion of a source (either a primary source or scattered light) from $n\,\partial\ell/\partial t$ and 2) the generalized Doppler shift that results from a time-varying change in RI, $\ell\,\partial n/\partial t$. The generalized Doppler shift was first observed and reported in the 1960s following deployment of communications satellites. While the conventional Doppler shift was observed due to the orbital velocity of the satellite, there was a persistent additional, and random, contribution to the Doppler shift that was observed. This “extra” term in the Doppler shift arises from turbulent atmospheric fluctuations that lead to a time-varying accumulated path length for the propagating pulses and is called the "generalized

Doppler shift" [81–88], in this case of microwave radio pulses. Both of these Doppler shift terms originate from a time-varying change in the optical path length.

The generalized Doppler shift that we exploit in this Article occurs due to the rapid change in RI experienced by a probe pulse propagating in a medium at a pump-probe time delay, τ, following the passage of a short pump pulse that has excited coherences of Raman vibrational modes (at delay times shorter than the dephasing time scale). The generalized Doppler frequency shift imparted to the probe pulse in the experiment depends on the arrival time of the probe pulse, τ, and takes the form $\delta\omega(\tau) = -k_{\rm pr}\,\ell\,\partial\,\delta n(t;\tau)/\partial\,t$, where $k_{\rm pr} = 2\,\pi/\lambda_{\rm pr}$ is the wavenumber of the probe pulse, with $\lambda_{\rm pr}$ denoting the wavelength of the probe pulse center frequency. The RI perturbation induced by ISRS takes the form $\delta n(t;\tau) \approx 2\delta\chi(t;\tau)/2$. In the case of RFDR, this generalized Doppler shift is uniform for every pulse in the laser pulse train for equivalent ISRS conditions because the molecular system relaxes back to thermal equilibrium between each pump pulse. The modulation of the pump pulse energy makes the imparted Doppler Raman optical frequency shift vary sinusoidally, permitting lock-in detection.

5.7 The Noise Floor for RFDR Spectroscopy

A comprehensive discussion of noise for RFDR spectroscopy is beyond the scope of this Article. However, we will discuss the primary conclusions that show the superior scaling of RFDR spectroscopy SNR compared to other CRS methods that rely on measuring power fluctuations from scattered optical power or changes in probe power. The two biggest sources of noise in mode-locked ultrafast lasers are intensity fluctuations that vary slowly (compared to the pulse spacing) called relative intensity noise (RIN), and noise in the relative arrival time of the pulses in the pulse train, which is called timing jitter. In addition, all optical measurements are subject to counting statistics, or shot noise. Coherent spectroscopes that detect a signal based on a change in the probe pulse optical power are primarily subject to RIN and shot noise. By contrast RFDR detection is, to first order, immune to RIN, but is limited by laser oscillator timing jitter and shot noise. We consider the impact of these noise sources on CRS measurements. To compare similar coherent

Raman measurements, we consider the SNR between different methods under identical experimental conditions. The limit of detection for measurements occurs when the SNR reaches ~ 1. Noise depends on the detection bandwidth, or is inversely proportional to the integration time of the measurement, Δt and the nonlinear susceptibility, $\chi^{(3)}$, so that we adopt the following notation for the SNR given by

$$\mathrm{SNR} = \kappa \, \mathrm{Im}\{\chi^{(3)}\} \sqrt{\Delta t}. \tag{5.3}$$

Here the parameter κ is determined by the experimental setup, including the particular type of CRS spectroscopy, be it CARS, SRS, or RFDR, for example. We further note that each of these methods depends on the average pump power, p_1 and focusing conditions that are wrapped up in the coefficient h_{CRS}, leading to a coefficient $\rho = \kappa / h_{\mathrm{CRS}} \, p_1$.

For the conventional intensity-based CRS measurements, we consider the two limiting cases where RIN dominates, giving an SNR coefficient of $\rho_{\mathrm{RIN}} = \beta_{\mathrm{RIN}} \, 10^{-\sigma_{\mathrm{RIN}}/20}$, where β is a coefficient that varies for each style of coherent Raman and depends on the coherent excitation process. The SNR coefficient for shot noise is $\rho_{\mathrm{shot}} = \beta_{\mathrm{shot}} \sqrt{p_2}$, where p_2 is the probe pulse average power. The relative contribution of shot noise to the SNR decreases as the average probe power increases, and at high enough power, the RIN dominates the SNR of the measurement. Note, however, that since RIN is correlated in the signal measured by two independent detectors, RIN can be largely suppressed by balanced optical detection [89]. A typical RIN value of $\sigma_{\mathrm{RIN}} = -150$ dBc leads to a value of $\rho_{\mathrm{RIN}} = 1.4 \times 10^{12}$, whereas at an average probe power of 10 mW, the SNR parameter for shot noise is $\rho_{\mathrm{shot}} = 5.6 \times 10^{12}$, and is still the dominant noise process under these conditions.

In the RFDR experiments, the intrinsic rms timing jitter from the laser pulse train near the lock-in amplifier modulation frequency is much lower than the rms timing jitter from the phase noise introduced by shot noise in the optical detector. The shot noise-limited RF phase noise PSD scales with the RF signal power, rather than the the average power of the probe pulse beam. This leads to a SNR coefficient that scales *linearly* with the average probe pulse power, with a expression giving $\rho_{\mathrm{RFDR}} = \beta_{\mathrm{RFDR}} p_2$. This is in stark contrast to the scaling of $\sqrt{p_2}$ for shot noise of measurements

of changes in optical power incident on the photodiode. For our experimental configuration with 10 mW of probe average power, the SNR parameter is $\rho_{\mathrm{RFDR}} = 6.8 \times 10^{13}$, or roughly $10\times$ higher than for SRS. The saturation power of our high-speed photodiodes is 10 mW, whereas by contrast SRS experiments use detectors with saturation powers exceeding 20 mW [89]. Implementation of higher saturation power detectors for RFDR will further improve detection sensitivity by lowering the shot noise-limited phase noise.

We note that many groups have demonstrated shot noise detection with SRS. The shot noise detection for RFDR is not equivalent to what has been performed with SRS. Here, we demonstrate shot noise-limited phase noise detection for RFDR. In fact, we show that RFDR can perform better than SRS at the shot noise limit. The difference between the two arises from the fact that the signals are different in each case, i.e., a change in probe average power is detected in SRS, whereas a change in arrival time (measured as an RF phase) is detected in RFDR. In the case of RFDR, the timing delay (and thus RF phase) can be amplified by a dispersive system, independent of the sample, whereas this is not possible with SRS.

Using the RFDR dispersive system the ISRS-induced optical frequency shift is transformed into a quantity that can be measured with more precision, namely a timing jitter on the probe pulse train. In fact, mode-locked ultrafast lasers can exhibit extremely low timing jitter, well below the level that can routinely be detected with the purely electronic RF phase detection strategy outlined here. The timing jitter PSD in the neighborhood of some offset frequency from the AOM modulation, f_m, can be written in the form $S_{\delta\tau} = 10^{-b}\,\mathrm{fs}^2/\mathrm{Hz}$. Assuming that the timing jitter PSD dominates the noise in the measurement (i.e. surpassing the electronic RF phase limits), the SNR parameter reads $\rho_{\mathrm{lim}} = \sqrt{2}\,\beta_{\mathrm{lim}}\,10^{b/2}\,\mathrm{fs}^{-1}$. In SI units, for the experimental conditions in this Article, we obtain a value of $\rho_{\mathrm{lim}} \approx 8 \times 10^{16}$, or more than three orders of magnitude higher than the shot noise limit for SRS. Thus, the RFDR strategy of converting an optical frequency shift into a timing delay has the potential to scale in sensitivity by several more orders of magnitude.

5.8 Verification of RFDR Shot Noise-Limited Timing Jitter

Figure (5.8) shows timing jitter PSDs of the RFDR system for the first three RF harmonics from offset frequencies, f_{off}, of 500kHz to 10MHz. The dashed lines shown for each of the harmonics represent the shot noise-limited timing jitter PSD expected based on the RF power generated by the PD.

To measure the timing jitter PSD of the RFDR system, first the sample cuvette was removed from the spectroscopic system. The RF signals were carefully conditioned for RF phase detection as discussed in the manuscript. With no Raman-active sample in the spectroscope, the output of the RF frequency mixer/phase detector determines the RFDR experimental system noise floor. To measure the phase noise PSD, the phase detector output is low-pass filtered, preamplified, and then connected to a spectrum analyzer (Signal Hound). The noise PSD measured by the spectrum analyzer can be converted to single sideband phase noise using the conversion factor, K_ϕ, specific to the RF mixer being used. The conversion factor of the mixer/phase detector was measured using the well-known beat-note method.

Once the single sideband phase noise, $S_{\delta\phi}$, has been measured, it is straightforward to convert this to a timing jitter PSD, which are related by $S_{\delta\tau_{\text{rms}}} = (2\pi m f_R)^{-2} S_{\delta\phi}$. As can be seen in Figure (5.8), when the RFDR system is running with the $m = 2$ and $m = 3$ RF harmonics it is close to the calculated shot noise-limited level. The separation between the measured noise floor for $m = 1$ and the shot noise-limited level can most likely be attributed to some amplitude-to-phase noise conversion in the fiber-coupled PDs. Our measurements of the timing jitter PSD at the various RF harmonics confirm that we are running RFDR spectroscopy at the lowest possible timing jitter for electronic phase detection of RF signals synthesized from standard fiber-coupled PDs.

Under conditions of the lowest noise operation, we produced RF powers of 117, 4.17, and 0.50 μW for the $m = 1, 2, 3$ harmonics, respectively, in our system. For these RF powers, the effective timing jitter PSD is $S_{\delta\tau} = 0.020, 0.058, 0.30$ fs^2/Hz, respectively for increasing harmonic order. In the form $S_{\delta\tau} = 10^{-b}$ fs^2/Hz, we find $b = 1.7, 1.2, 0.53$, respectively. The rms timing jitter that

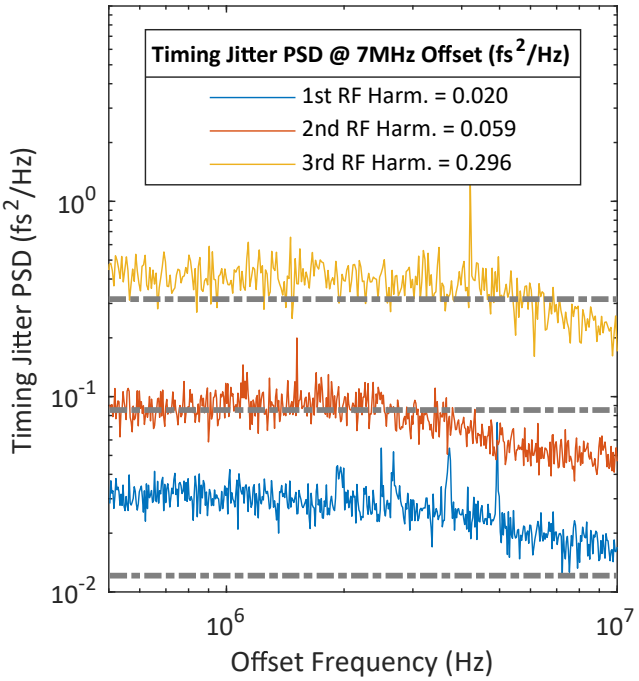

Figure 5.8: Measured timing jitter PSDs. The dashed lines are the shot noise-limited timing jitter levels computed from the measured RF power in each harmonic order using the formula $S_{\delta\phi} = 10\log_{10}\left[h\nu/2\,p_{\mathrm{RF}}(\pi\, m\, f_R)^2\right]$.

sets our detection limit in a Δt integration time is $\delta\tau_{\mathrm{rms}} = \{0.10, 0.17, 0.39\}/\sqrt{\Delta t}$ fs s$^{-1/2}$, for the three ascending harmonics.

The second and third order harmonics both exhibited a noise floor within < 0.5 dB of the calculated shot noise limit, whereas the first order harmonic was 2.2 dB higher than the shot noise limit. Detection with lower harmonic orders produces a higher SNR because the highly chirped pulses lead to a nonlinear reduction in RF power with harmonic order, causing a commensurate nonlinear increase in the phase noise floor. The current experiment is limited in sensitivity by the RF power generated in the probe pulse PD. This RF power can be scaled to produce a lower detection timing jitter PSD as generated in experiments carried out at NIST, where a high power diode detected microwave tones from mode-locked oscillators with a phase noise down to -179 dBc/Hz [90]. Further, alternative methods of phase detection promise to reduce the timing jitter

PSD noise floor by several orders of magnitude, offering a path to improved detection sensitivity using the principles of RFDR spectroscopy.

Chapter 6

Summary and Conclusions

The work in this thesis has successfully pushed forward the practicality and utility of ISRS for microspectroscopy and its applications to complex biological samples. Split spectrum ISRS successfully overcomes many of the limitations of the simple spectral filter detection technique. Rather than the typical experimental setup that relies on orthogonally polarized pump and probe beams and a linear polarizer to reject the pump beam after the sample, split spectrum ISRS leverages the high extinction capabilities of dichroic filtering which remain robust through birefringent and scattering samples. Careful analysis of the split spectrum technique showed that it is a viable method for ISRS and is capable of exciting Raman vibrational modes well into the biomolecular fingerprint region. We find that while the very highest vibrational frequencies are mildly attenuated in the signal and SNR, the vast majority of the low frequency vibrational spectrum can be interrogated with nearly the same fidelity as in a conventional ISRS pump probe scenario. Finally, a stage-scanning hyperspectral image of a complex sample was obtained.

While ISRS can access mid-band Raman frequencies (i.e., the fingerprint region) with careful control over the pulse shape, the unique ability of ISRS to probe low frequency vibrational modes was explored. We have developed a new and versatile method for low-frequency coherent Raman imaging. ϕ-ISRS is a phase sensitive detection scheme for ISRS that more closely resembles the inherent excitation profile of impulsive excitation. By employing a phase-stable probe/reference pair, we were able to significantly increase the robustness of phase sensitive ISRS and demonstrate low-frequency Raman excitation through multiple scattering layers and demonstrated hyperspectral imaging using ϕ-ISRS. These developments open avenues to use low-frequency Raman vibrational spectroscopy in complex systems and samples.

We have also demonstrated a new concept to enhance the sensitivity for coherent Raman spectroscopy that optically amplifies the Raman signal by converting the generalized Doppler Raman (DR) frequency shift into a timing jitter modulation. The transformation of the Raman signal into a

timing jitter allows access to lower noise levels than is possible with the conventional optical power perturbation detection techniques for CRS. We have shown the ability to record Raman spectra from a range of molecular components, some of which are involved in plant metabolic activity, and also demonstrated the ability to differentiate the redox state of $\mathrm{NADH}/\mathrm{NAD}^{+}$ with RFDR spectra. Increasing the sensitivity of coherent Raman to sub-mM concentrations is an important step towards achieving the long term goal of label-free detection of low concentration analytes in cells and tissues.

Challenges remain with the development of ISRS for biomedical applications. Because ISRS is fundamentally a pump/probe technique, acquisition times are limited by how quickly the pump and probe pulses can be scanned in time. Use of a voice-coil based pulse scanner has enabled high-speed pump/probe scanning, the acquisition times for stage-scanning images must be improved for high throughput applications or studying dynamic biological systems. We wish to develop ISRS into a high-speed imaging modality that can be paired with other label-free techniques to provide a more comprehensive study of biology. Split spectrum ISRS and ϕ-ISRS are more experimentally simple than Doppler Raman, but are still challenging due to the difficultly of maintaining short optical pulses after traveling through dispersive materials. Balanced detection could eliminate the need for the acousto-optic modulator for beam intensity modulation, which will drastically reduce the spectral dispersion burden of the system. Such an approach would allow for easier use of high numerical aperture objective lenses that also carry a high dispersion. Future work will explore additional strategies to simplify these ISRS techniques in order to progress from development to a more user-friendly system intended to use low to mid-frequency Raman vibrations as a complement to other modalities when studying dyanmic biological questions such as cell metabolism, protein deformation [6], and virus capsid vibrations, [5].

6.1 Funding

The work in this thesis was gratefully supported in part by the NIH/NIGMS 1R21GM135772 "Off-resonant transient absorption microscopy", the W. M. Keck foundation, DOE Grant Nos. DE-SC0013265 and DE-SC0019545, DE-FOA-0002603.

Bibliography

[1] R. A. Bartels, T. C. Weinacht, N. Wagner, M. Baertschy, Chris H. Greene, M. M. Murnane, and H. C. Kapteyn. Phase modulation of ultrashort light pulses using molecular rotational wave packets. *Physical Review Letters*, 88(1):013903–, 12 2001.

[2] Notburga Gierlinger, Tobias Keplinger, and Michael Harrington. Imaging of plant cell walls by confocal raman microscopy. *Nature Protocols*, 7:1694 EP –, 08 2012.

[3] J. Chan, S. Fore, S. Wachsmann-Hogiu, and T. Huser. Raman spectroscopy and microscopy of individual cells and cellular components. *Laser & Photonics Reviews*, 2(5):325–349, 2008.

[4] Christian W. Freudiger, Wei Min, Brian G. Saar, Sijia Lu, Gary R. Holtom, Chengwei He, Jason C. Tsai, Jing X. Kang, and X. Sunney Xie. Label-free biomedical imaging with high sensitivity by stimulated raman scattering microscopy. *Science*, 322(5909):1857, 12 2008.

[5] Kong-Thon Tsen, Eric C Dykeman, Otto F Sankey, Shaw-Wei D Tsen, Nien-Tsung Lin, and Juliann G Kiang. Probing the low-frequency vibrational modes of viruses with raman scattering—bacteriophage m13 in water. *Journal of biomedical optics*, 12(2):024009, 2007.

[6] Christian Rischel, Diane Spiedel, Justin P. Ridge, Michael R. Jones, Jacques Breton, Jean-Christophe Lambry, Jean-Louis Martin, and Marten H. Vos. Low frequency vibrational modes in proteins: Changes induced by point-mutations in the protein-cofactor matrix of bacterial reaction centers. *Proceedings of the National Academy of Sciences*, 95(21):12306–12311, 1998.

[7] S. Amin, S. Blake, S. M. Kenyon, R. C. Kennel, and E. N. Lewis. A novel combination of dls-optical microrheology and low frequency raman spectroscopy to reveal underlying biopolymer self-assembly and gelation mechanisms. *The Journal of Chemical Physics*, 141(23):234201, 2014.

[8] Tharith Sriv, Kangwon Kim, and Hyeonsik Cheong. Low-frequency raman spectroscopy of few-layer 2h-sns2. *Scientific Reports*, 8(1):10194, 2018.

[9] Alexander A. Puretzky, Liangbo Liang, Xufan Li, Kai Xiao, Kai Wang, Masoud Mahjouri-Samani, Leonardo Basile, Juan Carlos Idrobo, Bobby G. Sumpter, Vincent Meunier, and David B. Geohegan. Low-frequency raman fingerprints of two-dimensional metal dichalcogenide layer stacking configurations. *ACS Nano*, 9(6):6333–6342, 06 2015.

[10] Randy A Bartels, Dan Oron, and Hervé Rigneault. Low frequency coherent raman spectroscopy. *Journal of Physics: Photonics*, 3(4):042004, 2021.

[11] Ji-Xin Cheng and X. Sunney Xie. Vibrational spectroscopic imaging of living systems: An emerging platform for biology and medicine. *Science*, 350(6264), 2015.

[12] Chawin Ounkomol, Sharmishtaa Seshamani, Mary M. Maleckar, Forrest Collman, and Gregory R. Johnson. Label-free prediction of three-dimensional fluorescence images from transmitted-light microscopy. *Nature Methods*, 15(11):917–920, 2018.

[13] Y. R. Shen and N. Bloembergen. Theory of stimulated brillouin and raman scattering. *Physical Review*, 137(6A):A1787–A1805, 03 1965.

[14] Chi Zhang, Delong Zhang, and Ji-Xin Cheng. Coherent raman scattering microscopy in biology and medicine. *Annual Review of Biomedical Engineering*, 17(1):415–445, 2018/08/30 2015.

[15] Hervé Rigneault and Pascal Berto. Tutorial: Coherent raman light matter interaction processes. *APL Photonics*, 3(9):091101, 2018.

[16] Lisa Dhar, John A. Rogers, and Keith A. Nelson. Time-resolved vibrational spectroscopy in the impulsive limit. *Chemical Reviews*, 94(1):157–193, 01 1994.

[17] Klaus Hartinger and Randy A. Bartels. Single-shot measurement of ultrafast time-varying phase modulation induced by femtosecond laser pulses with arbitrary polarization. *Applied Physics Letters*, 92(2):021126, 2018/08/30 2008.

[18] Jesse W. Wilson, Philip Schlup, and Randy Bartels. Phase measurement of coherent raman vibrational spectroscopy with chirped spectral holography. *Optics Letters*, 33(18):2116–2118, 2008.

[19] Jesse W. Wilson, Philip Schlup, and Randy A. Bartels. Synthetic temporal aperture coherent molecular phase spectroscopy. *Chemical Physics Letters*, 463(4):300–304, 2008.

[20] P. Schlup, J. W. Wilson, and R. A. Bartels. Sensitive and selective detection of low-frequency vibrational modes through a phase-shifting fourier transform spectroscopy. *IEEE Journal of Quantum Electronics*, 45(7):777–782, 2009.

[21] Dekel Raanan, Julian Lüttig, Yaron Silberberg, and Dan Oron. Vibrational spectroscopy via stimulated raman induced kerr lensing. *APL Photonics*, 3(9):092501, 2018/08/30 2018.

[22] Dekel Raanan, Xavier Audier, Siddarth Shivkumar, Maor Asher, Matan Menahem, Omer Yaffe, Nicolas Forget, Hervé Rigneault, and Dan Oron. Sub-second hyper-spectral low-frequency vibrational imaging via impulsive raman excitation. *Opt. Lett.*, 44(21):5153–5156, Nov 2019.

[23] David R Smith, Jeffrey J Field, David G Winters, Scott R Domingue, Frauke Rininsland, Daniel J Kane, Jesse W Wilson, and Randy A Bartels. Phase noise limited frequency shift impulsive raman spectroscopy. *APL Photonics*, 6(2):026107, 2021.

[24] S. R. Domingue, D. G. Winters, and R. A. Bartels. Time-resolved coherent raman spectroscopy by high-speed pump-probe delay scanning. *Optics Letters*, 39(14):4124–4127, 2014.

[25] E. Gershgoren, R. A. Bartels, J. T. Fourkas, R. Tobey, M. M. Murnane, and H. C. Kapteyn. Simplified setup for high-resolution spectroscopy that uses ultrashort pulses. *Optics Letters*, 28(5):361–363, 2003.

[26] Hikaru Kuramochi, Satoshi Takeuchi, and Tahei Tahara. Femtosecond time-resolved impulsive stimulated raman spectroscopy using sub-7-fs pulses: Apparatus and applications. *Review of Scientific Instruments*, 87(4):043107, 2016.

[27] Philip Schlup, Jesse Wilson, Klaus Hartinger, and Randy A. Bartels. Dispersion balancing of variable-delay monolithic pulse splitters. *Appl. Opt.*, 46(23):5967–5973, Aug 2007.

[28] Yahel Soffer, Dekel Raanan, and Dan Oron. Low frequency collinear pre-resonant impulsive stimulated raman microspectroscopy. *ACS Photonics*, 7(12):3481–3488, 12 2020.

[29] Liqing Ren, Ilan Hurwitz, Dekel Raanan, Patric Oulevey, Dan Oron, and Yaron Silberberg. Terahertz coherent anti-stokes raman scattering microscopy. *Optica*, 6(1):52–55, Jan 2019.

[30] Dekel Raanan, Liqing Ren, Dan Oron, and Yaron Silberberg. Impulsive raman spectroscopy via precision measurement of frequency shift with low energy excitation. *Optics Letters*, 43(3):470–473, 2018.

[31] JunWoo Kim, Tai Hyun Yoon, and Minhaeng Cho. Interferometric measurement of transient absorption and refraction spectra with dual frequency comb. *The Journal of Physical Chemistry B*, 122(42):9775–9785, 10 2018.

[32] Kurt Thorn and Doug Kellogg. A quick guide to light microscopy in cell biology. *Molecular Biology of the Cell*, 27(2):219–222, 2018/08/30 2016.

[33] Ling Tong and Ji-Xin Cheng. Label-free imaging through nonlinear optical signals. *Materials Today*, 14(6):264–273, 2011.

[34] Richard Kasprowicz, Rakesh Suman, and Peter O'Toole. Characterising live cell behaviour: Traditional label-free and quantitative phase imaging approaches. *The International Journal of Biochemistry & Cell Biology*, 84:89–95, 2017.

[35] Riccardo Cicchi and Francesco Saverio Pavone. Multimodal nonlinear microscopy: A powerful label-free method for supporting standard diagnostics on biological tissues. *Journal of Innovative Optical Health Sciences*, 07(05):1330008, 2014.

[36] Iwan W Schie and Thomas Huser. Label-free analysis of cellular biochemistry by raman spectroscopy and microscopy. *Comprehensive Physiology*, 3(2):941–956, 2013.

[37] Giulia Borile, Deborah Sandrin, Andrea Filippi, Kurt I. Anderson, and Filippo Romanato. Label-free multiphoton microscopy: Much more than fancy images. *International Journal of Molecular Sciences*, 22(5), 2021.

[38] Nirmal Mazumder, Naveen K. Balla, Guan-Yu Zhuo, Yury V. Kistenev, Rajesh Kumar, Fu-Jen Kao, Sophie Brasselet, Viktor V. Nikolaev, and Natalya A. Krivova. Label-free non-linear multimodal optical microscopy—basics, development, and applications. *Frontiers in Physics*, 7, 2019.

[39] Martin Schnell, Shachi Mittal, Kianoush Falahkheirkhah, Anirudh Mittal, Kevin Yeh, Seth Kenkel, Andre Kajdacsy-Balla, P Scott Carney, and Rohit Bhargava. All-digital histopathology by infrared-optical hybrid microscopy. *Proceedings of the National Academy of Sciences*, 117(7):3388–3396, 2020.

[40] Samy Andrea Strola, Jean-Charles Baritaux, Emmanuelle Schultz, Anne Catherine Simon, Cédric Allier, Isabelle Espagnon, Dorothée Jary, and Jean-Marc Dinten. Single bacteria identification by Raman spectroscopy. *Journal of Biomedical Optics*, 19(11):111610, 2014.

[41] R. Merlin. Generating coherent thz phonons with light pulses. *Solid State Communications*, 102(2):207–220, 1997.

[42] Dekel Raanan, Xavier Audier, Siddarth Shivkumar, Maor Asher, Matan Menahem, Omer Yaffe, Nicolas Forget, Hervé Rigneault, and Dan Oron. Sub-second hyper-spectral low-frequency vibrational imaging via impulsive raman excitation. *Optics letters*, 44(21):5153–5156, 2019.

[43] David R Smith, Siddarth Shivkumar, Jeff Field, Jesse W Wilson, Hervé Rigneault, and Randy A Bartels. Nearly degenerate two-color impulsive coherent raman hyperspectral imaging. *Optics Letters*, 47(22):5841–5844, 2022.

[44] Jared K. Wahlstrand, Roberto Merlin, Xiaoqin Li, Steven T. Cundiff, and Oscar E. Martinez. Impulsive stimulated raman scattering: comparison between phase-sensitive and spectrally filtered techniques. *Opt. Lett.*, 30(8):926–928, Apr 2005.

[45] Walker Peterson, Julia Gala De Pablo, Matthew Lindley, Kotaro Hiramatsu, and Keisuke Goda. Ultrafast impulsive raman spectroscopy across the terahertz–fingerprint region. *Advanced Photonics*, 4(1):016003–016003, 2022.

[46] Meindert A van Dijk, Markus Lippitz, and Michel Orrit. Detection of acoustic oscillations of single gold nanospheres by time-resolved interferometry. *Physical review letters*, 95(26):267406, 2005.

[47] Philip Schlup, Jesse Wilson, Klaus Hartinger, and Randy A Bartels. Dispersion balancing of variable-delay monolithic pulse splitters. *Applied optics*, 46(23):5967–5973, 2007.

[48] Soumen Ghosh, Georg Herink, Antonio Perri, Fabrizio Preda, Cristian Manzoni, Dario Polli, and Giulio Cerullo. Broadband optical activity spectroscopy with interferometric fourier-transform balanced detection. *ACS photonics*, 8(8):2234–2242, 2021.

[49] Jesse W Wilson and Randy A Bartels. Rapid birefringent delay scanning for coherent multiphoton impulsive raman pump–probe spectroscopy. *IEEE Journal of Selected Topics in Quantum Electronics*, 18(1):130–139, 2011.

[50] R. A. Bartels, T. C. Weinacht, S. R. Leone, H. C. Kapteyn, and M. M. Murnane. Nonresonant control of multimode molecular wave packets at room temperature. *Physical Review Letters*, 88(3):033001–, 01 2002.

[51] SR Domingue and RA Bartels. Nearly transform-limited sub-20-fs pulses at 1065 nm and> 10 nj enabled by a flat field ultrafast pulse shaper. *Optics Letters*, 40(2):253–256, 2015.

[52] Jesse W. Wilson, Philip Schlup, Monte Lunacek, Darrell Whitley, and Randy A. Bartels. Calibration of liquid crystal ultrafast pulse shaper with common-path spectral interferometry and application to coherent control with a covariance matrix adaptation evolutionary strategy. *Review of Scientific Instruments*, 79(3):033103, 2022/09/07 2008.

[53] Faris Sinjab, Kazuki Hashimoto, Xuanqiang Zhao, Yu Nagashima, and Takuro Ideguchi. Enhanced spectral resolution for broadband coherent anti-stokes raman spectroscopy. *Opt. Lett.*, 45(6):1515–1518, Mar 2020.

[54] Judith Baumgart, Kai Kuetemeyer, Willem Bintig, Anaclet Ngezahayo, Wolfgang A. Ertmer, Holger Lubatschowski, and Alexander Heisterkamp. Repetition rate dependency of reactive oxygen species formation during femtosecond laser-based cell surgery. *Journal of Biomedical Optics*, 14(5):1 – 9, 2009.

[55] Paul L. Stiles, Jon A. Dieringer, Nilam C. Shah, and Richard P. Van Duyne. Surface-enhanced raman spectroscopy. *Annual Review of Analytical Chemistry*, 1(1):601–626, 2018/08/30 2008.

[56] M. D. Duncan, J. Reintjes, and T. J. Manuccia. Scanning coherent anti-stokes raman microscope. *Optics Letters*, 7(8):350–352, 1982.

[57] Andreas Zumbusch, Gary R. Holtom, and X. Sunney Xie. Three-dimensional vibrational imaging by coherent anti-stokes raman scattering. *Phys. Rev. Lett.*, 82:4142–4145, May 1999.

[58] Yan Fu, Haifeng Wang, Riyi Shi, and Ji-Xin Cheng. Characterization of photodamage in coherent anti-stokes raman scattering microscopy. *Optics Express*, 14(9):3942–3951, 2006.

[59] Yong-Xin Yan, Edward B. Gamble, and Keith A. Nelson. Impulsive stimulated scattering: General importance in femtosecond laser pulse interactions with matter, and spectroscopic applications. *The Journal of Chemical Physics*, 83(11):5391–5399, 2018/08/30 1985.

[60] J. Chesnoy and A. Mokhtari. Resonant impulsive-stimulated raman scattering on malachite green. *Phys. Rev. A*, 38:3566–3576, Oct 1988.

[61] T. C. Weinacht, R. Bartels, S. Backus, P. H. Bucksbaum, B. Pearson, J. M. Geremia, H. Rabitz, H. C. Kapteyn, and M. M. Murnane. Coherent learning control of vibrational motion in room temperature molecular gases. *Chemical Physics Letters*, 344(3):333–338, 2001.

[62] Nirit Dudovich, Dan Oron, and Yaron Silberberg. Single-pulse coherently controlled nonlinear raman spectroscopy and microscopy. *Nature*, 418:512 EP –, 08 2002.

[63] Klaus Hartinger and Randy A. Bartels. Modulation of third-harmonic generation conversion in the presence of a rotational wave packet. *Optics Letters*, 33(11):1162–1164, 2008.

[64] David Kupka, Jesse W. Wilson, Omid Masihzadeh, and Randy A. Bartels. Distinguishing bulk and interface modulation of optical third harmonic generation due to coherent optical phonon excitation. *Chemical Physics Letters*, 490(1):97–101, 2010.

[65] Jesse W. Wilson and Randy A. Bartels. Coherence-modulated third harmonic generation for vibrational spectroscopy: a theoretical treatment. *Journal of the Optical Society of America B*, 29(8):1875–1883, 2012.

[66] Carsten Cleff, Alicja Gasecka, Patrick Ferrand, Hervé Rigneault, Sophie Brasselet, and Julien Duboisset. Direct imaging of molecular symmetry by coherent anti-stokes raman scattering. *Nature Communications*, 7:11562 EP –, 05 2016.

[67] R. P. Scott, C. Langrock, and B. H. Kolner. High-dynamic-range laser amplitude and phase noise measurement techniques. *IEEE Journal of Selected Topics in Quantum Electronics*, 7(4):641–655, 2001.

[68] J. Kim and F. X. Kärtner. Attosecond-precision ultrafast photonics. *Laser & Photonics Reviews*, 4(3):432–456, 2018/08/30 2010.

[69] Randy A. Bartels and David G. Winters. Apparatus and method for measurement of optical frequency shifts. US Patent App. 15/317,963, July 2018.

[70] J. J. McFerran, E. N. Ivanov, A. Bartels, G. Wilpers, C. W. Oates, S. A. Diddams, and L. Hollberg. Low-noise synthesis of microwave signals from an optical source. *Electronics Letters*, 41(11):650–651, May 2005.

[71] Yoshifumi Nishimura and Masamichi Tsuboi. Raman spectra of flavins: avoidance of interference from fluorescence. *Chemical Physics Letters*, 59(2):210 – 213, 1978.

[72] L. Rimai, T. Cole, J. L. Parsons, Jr. Hickmott, J. T., and E. B. Carew. Studies of raman spectra of water solutions of adenosine tri-, di-, and monophosphate and some related compounds. *Biophys J*, 9(3):320–9, 1969.

[73] T. T. Chen, C. S. Kuo, Y. C. Chou, and N. T. Liang. Surface-enhanced raman scattering of adenosine triphosphate molecules. *Langmuir*, 5(4):887–891, 1989.

[74] Kwok To Yue, Charlotte L. Martin, Dehuai Chen, Paula Nelson, Donald L. Sloan, and Robert Callender. Raman spectroscopy of oxidized and reduced nicotinamide adenine dinucleotides. *Biochemistry*, 25(17):4941–4947, 1986. PMID: 3768324.

[75] Joke De Gelder, Kris De Gussem, Peter Vandenabeele, and Luc Moens. Reference database of raman spectra of biological molecules. *Journal of Raman Spectroscopy*, 38(9):1133–1147, 2007.

[76] Guillermo Diaz Fleming, Justin J. Finnerty, Marcelo Campos-Vallette, Freddy Célis, Alvaro E. Aliaga, Carlos Fredes, and Rainer Koch. Experimental and theoretical raman and surface-enhanced raman scattering study of cysteine. *Journal of Raman Spectroscopy*, 40(6):632–638, 2009.

[77] A. Pawlukojc, J. Leciejewicz, A. J. Ramirez-Cuesta, and J. Nowicka-Scheibe. l-cysteine: Neutron spectroscopy, raman, ir and ab initio study. *Spectrochim Acta A Mol Biomol Spectrosc*, 61(11-12):2474–81, 2005.

[78] Songzhou Hu, Ian K. Morris, Jai P. Singh, Kevin M. Smith, and Thomas G. Spiro. Complete assignment of cytochrome c resonance raman spectra via enzymic reconstitution with isotopically labeled hemes. *Journal of the American Chemical Society*, 115(26):12446–12458, 1993.

[79] Chien-Sheng Liao, Kai-Chih Huang, Weili Hong, Andy J Chen, Caroline Karanja, Pu Wang, Gregory Eakins, and Ji-Xin Cheng. Stimulated Raman spectroscopic imaging by microsecond delay-line tuning. *Optica*, 3(12):1377–1380, dec 2016.

[80] Kwangyun Jung and Jungwon Kim. Characterization of timing jitter spectra in free-running mode-locked lasers with 340 dB dynamic range over 10 decades of Fourier frequency. *Opt. Lett.*, 40(3):316–319, feb 2015.

[81] William H. Guier and George C. Weiffenbach. Theoretical analysis of doppler radio signals from earth satellites. *Nature*, 181(4622):1525–1526, 1958.

[82] J.A. Bennett. The calculation of doppler shifts due to a changing ionosphere. *Journal of Atmospheric and Terrestrial Physics*, 29(7):887 – 891, 1967.

[83] JA Bennett. The ray theory of doppler frequency shifts. *Australian Journal of Physics*, 21(3):259–272, 1968.

[84] J. A. Bennett. On the application of variation techniques to the ray theory of radio propagation. *Radio Science*, 4(8):667–678, 1969.

[85] R. L. Fante. Propagation of electromagnetic waves in media which vary slowly with position and time. *Radio Science*, 7(12):1153–1162, 1972.

[86] D. Censor and J.J. Brandstatter. Generalized doppler effect in time-varying media. *Journal of the Franklin Institute*, 297(6):485 – 490, 1974.

[87] P.L Dyson. Relationships between the rate of change of phase path (doppler shift) and angle of arrival. *Journal of Atmospheric and Terrestrial Physics*, 37(8):1151 – 1154, 1975.

[88] H. S. Hopfield. The effect of tropospheric refraction on the doppler shift of a satellite signal. *Journal of Geophysical Research*, 68(18):5157–5168, 2018/08/30 15 September 1963.

[89] Christian W. Freudiger, Wenlong Yang, Gary R. Holtom, Nasser Peyghambarian, X. Sunney Xie, and Khanh Q. Kieu. Stimulated raman scattering microscopy with a robust fibre laser source. *Nature Photonics*, 8(2):153–159, 2014.

[90] F. Quinlan, T. M. Fortier, H. Jiang, A. Hati, C. Nelson, Y. Fu, J. C. Campbell, and S. A. Diddams. Exploiting shot noise correlations in the photodetection of ultrashort optical pulse trains. *Nature Photonics*, 7:290 EP –, 03 2013.